How to see the forest for the trees:

Constraining the large-scale cosmic microwave background in the presence of polarized Galactic foregrounds

by

Duncan Joseph Watts

A dissertation submitted to The Johns Hopkins University

in conformity with the requirements for the degree of

Doctor of Philosophy

Baltimore, Maryland

July, 2018

Abstract

The Cosmology Large Angular Scale Surveyor (CLASS) is an experiment designed to constrain the amplitude of primordial gravitational waves generated during inflation. CLASS will do this by measuring the largest angular scales of the sky at 40, 90, 150, and 220 GHz across 70% of the sky to characterize all known sources of polarized microwave emission at these frequencies, the Galactic synchrotron and thermal dust emission, and the cosmic microwave background (CMB). This thesis begins by describing the CMB and how it is generated, as well as enumerating the Galactic foregrounds that must be removed in order to accurately characterize the CMB. I then describe in detail an optimal method for removing foregrounds while constraining the primordial gravitational waves' amplitude. I then use a power spectrum method to show that CLASS will be able to use its large angular scale data to constrain the reionization optical depth to near its cosmic variance limit, and describe how this will enable a measurement of the effects of massive neutrinos on galaxy clustering.

Primary Reader: Tobias A. Marriage

Secondary Reader: Charles L. Bennett

Acknowledgments

No man is an island, entire of itself; every man is a piece of the continent, a part of the main. If a clod be washed away by the sea, Europe is the less, as well as if a promontory were, as well as if a manor of thy friend's or of thine own were: any man's death diminishes me, because I am involved in mankind, and therefore never send to know for whom the bells tolls; it tolls for thee.

-John Donne, Devotions Upon Emergent Occasions (1624)

I would like to first thank Professor Tobias Marriage for his role in guiding me through my doctoral work. His boundless curiosity, his careful attention to detail, his dedication to his craft, and his good nature all inspire me to be a better person every day. I would also like to thank Professor Charles Bennett. His firm, direct, and kind guidance along with his phenomenal gift for clear and complete communication all provide standards for the scientist I strive to be. I have also benefited immensely from the guidance of David Larson, Janet Weiland, and Graeme Addison. Thank you to all of you for your guidance, your patience, and your good nature.

Thank you as well to the CLASS group as a whole. Not only did your labor give me a reason for my work, but the collegial atmosphere cultivated by all of you made my time here enjoyable and productive. Doing my PhD work with any other group

of people would have been a mistake.

Thanks especially to my friends, listed roughly the order in which I met them; Michael Calderone, Caitlin O'Neill, Michael Fountaine, William Ramsey, Andrew Brownjohn, Zhilei Xu, Rachael Alexandroff, Kathleen Harrington, Devin Crichton, Raymond Simons, Kirill Tchernyshyov, Wesley Fuhrman, Alena Fuhrman, Michael Peth, Michael Valentine, David Jones, Schuyler Wolff, Alexandra Greenbaum, Kirsten Hall, Sumit Dahal, Erini Lambrides, Jessica Berman, Carolina Núñez, and Jacob Hamer. I couldn't have made it without you.

Finally, thank you to my family.

Table of Contents

List of Tables

List of Figures

Chapter 1

Introduction

Since the discovery of general relativity, cosmologists' understanding of the universe has gone through several paradigm shifts, from lacking evidence against a static, infinite-aged universe to constraining its dynamics within fractions of a second of the Big Bang. I will briefly discuss the observational foundations of cosmology, before describing our theoretical understanding of the cosmic microwave background and astronomical impediments to its observation and characterization.

1.1 The Universe on the Whole

The modern cosmological revolution began with two fundamental, unexpected observations. The first was the expansion of the universe, as observed by Vesto Slipher and Edwin Hubble (Slipher, 1917; Hubble, 1926; Hubble, 1929), and the second was the discovery of the cosmic microwave background by Penzias and Wilson (Penzias and Wilson, 1965; Dicke et al., 1965). Both of these observations marked the first time that there was observational evidence that the universe was not infinite in age.

Hubble's law is the observational fact that there is a linear relation between the

distance between us and other galaxies and the velocity with which it is receding,

$$v = H_0 d. \tag{1.1}$$

The proportionality constant, H_0, is the current expansion rate of the universe and is consistent with the uniform expansion of space. Slipher's determination of the Doppler redshift $z = \sqrt{\frac{c+v}{c-v}} - 1 \approx v/c$, and Hubble's subsequent determination of these galaxies' immense distance from us, i.e. outside of the Milky Way, confirmed that all galaxies outside of the Local Group are in fact receding, and implied that the Universe was once much denser and hotter than it is today.

Cosmologists work in comoving coordinates that essentially cancel out the known recession velocity. The distance d between two galaxies, as measured at a single instant in time by a physical yardstick, can be rewritten as $d = a(t)r$, where r, the comoving separation, is fixed in time. Assuming there is no motion beyond the simple expansion of the universe, the relative velocity between the two galaxies is given by

$$v \equiv \frac{\mathrm{d}d}{\mathrm{d}t} = \frac{\mathrm{d}a}{\mathrm{d}t} r = \frac{\mathrm{d}\ln a}{\mathrm{d}t} d = Hd$$

where $H(t) \equiv \frac{\mathrm{d}\ln a}{\mathrm{d}t}$ is the time-dependent Hubble parameter, and where H_0 is this quantity evaluated today, a time t_0 after the Big Bang. The measurement of this expansion confirmed that the Universe was expanding, but was still consistent with the Universe having infinite age, constantly generating new particles to maintain a steady expanding state.

The discovery of a 3.5 ± 1.0 K blackbody at 4080 MHz was the event that cemented the astronomical community's belief in a Hot Big Bang model of the universe (Penzias and Wilson, 1965; Dicke et al., 1965). This signal was observed in all directions,

and could not be explained by any known terrestrial or astronomical source. The cleanest explanation has, and remains to be, that this is in fact thermal radiation from the beginning of the universe that permeates all of space, and was generated when the universe was once hotter and much denser. The *COBE*/FIRAS measurement of the spectral dependence of this Cosmic Microwave Background (CMB) radiation confirmed that this was a true blackbody radiation with temperature $T = 2.726 \pm 0.001$ K (Mather et al., 1994).

1.2 The FLRW Metric and the Homogeneous Universe

In order to accurately describe the dynamics of the universe, it is necessary to develop a mathematical formalism to make sense of concepts such as distance and time. This section uses the framework of general relativity in the form of Einstein's field equations to describe the universe's expansion history in terms of the density of its various components.

A four-dimensional spacetime has an invariant interval $ds^2 = g_{\mu\nu}\,\mathrm{d}x^\mu\,\mathrm{d}x^\nu$, where the geometry is encoded in the metric $g_{\mu\nu}(t, \boldsymbol{x})$. Note that here and throughout we use Einstein summation notation, such that repeated indices are implicitly summed over. The only possible three-dimensional spacetimes that are rotationally and translationally invariant are Euclidean space, three-dimensional space embedded into a 4-dimensional sphere, and three-dimensional space embedded into a 4-dimensional hyperbola. These three cases can be parametrized by the curvature constant $K = \{+1, -1, 0\}$ for spherical, hyperbolic, and Euclidean coordinates,

respectively, with the invariant interval given by

$$ds^2 = g_{\mu\nu}\,\mathrm{d}x^\mu\,\mathrm{d}x^\nu = -c^2\,\mathrm{d}t^2 + \mathrm{d}\boldsymbol{x}^2 + K\frac{(\boldsymbol{x}\cdot\mathrm{d}\boldsymbol{x})^2}{1-K\boldsymbol{x}^2}. \tag{1.2}$$

Because the curvature is approximately zero ($\Omega_K = 0.000 \pm 0.005$, Planck Collaboration, 2015b), we will set $K = 0$ throughout for brevity. Typically this is written with the expansion factored out of the proper coordinates $\boldsymbol{x}$,

$$ds^2 = g_{\mu\nu}\,\mathrm{d}x^\mu\,\mathrm{d}x^\nu = -c^2\,\mathrm{d}t^2 + a(t)^2\,\mathrm{d}\boldsymbol{x}^2,$$

where $\boldsymbol{x}$ are now comoving coordinates. This particular solution to Einstein's field equations is known as the Friedmann-Lemaître-Robertson-Walker (FLRW) metric. Note that the conformal time η is often used, defined such that $\mathrm{d}t = a(t)\,\mathrm{d}\eta$.

The functional form of the metric is incredibly important, and depends on the energy content of the universe. Using Einstein's field equations, it is possible to solve for the metric,

$$G_{\mu\nu} = 8\pi G T_{\mu\nu}, \tag{1.3}$$

where $T_{\mu\nu}$ is the stress-energy tensor, and $G_{\mu\nu}$ is the only covariant second derivative of the metric. This is the relativistic upgrade of Poisson's equation for gravity $\nabla^2\phi = 4\pi G\rho$, and in fact the 00 element of this equation does reduce to this in the weak-field limit.

The Einstein tensor is defined as $G_{\mu\nu} \equiv R_{\mu\nu} - \frac{1}{2}g_{\mu\nu}g^{\alpha\beta}R_{\alpha\beta}$, where the Ricci tensor is given by $R_{\mu\nu} = \partial_\alpha\Gamma^\alpha_{\mu\nu} - \partial_\nu\Gamma^\alpha_{\mu\alpha} + \Gamma^\alpha_{\beta\alpha}\Gamma^\beta_{\mu\nu} - \Gamma^\alpha_{\beta\nu}\Gamma^\beta_{\mu\alpha}$, and the Christoffel symbols are $\Gamma^\mu_{\alpha\beta} = \frac{1}{2}g^{\mu\nu}(\partial_\beta g_{\alpha\nu} + \partial_\alpha g_{\beta\nu} - \partial_\nu g_{\alpha\beta})$. The Christoffel symbols can be computed for the FLRW metric, giving $R_{00} = -3\frac{\ddot{a}}{a}$, $R_{ij} = \delta_{ij}[2\dot{a}^2 + a\ddot{a}]$, and $g^{\mu\nu}R_{\mu\nu} = 6\left[\frac{\ddot{a}}{a} + \left(\frac{\dot{a}}{a}\right)^2\right]$

so that the time-time component of the Einstein equations becomes

$$H^2 = \frac{8\pi G}{3}\rho. \tag{1.4}$$

Assuming the universe is described by a perfect fluid, the stress energy tensor is given by $T_{\mu\nu} = pg_{\mu\nu} + (p + \rho)u_\mu u_\nu$, where u_μ is the velocity 4-vector that satisfies $g^{\mu\nu}u_\mu u_\nu = -1$ and is $u_i = 0$ and $u_0 = -1$ in the rest frame. The stress energy tensor is covariantly conserved, implying that $\nabla_\mu T^\mu_\nu = 0$. The $\nu = 0$ component reduces to

$$\frac{\mathrm{d}\rho}{\mathrm{d}t} + 3H[\rho + p] = 0. \tag{1.5}$$

We can parametrize the components of the universe by their equations of state relating pressure to density $p = w\rho$, where the equation of state parameter $w \in \{0, \frac{1}{3}, -1\}$ for matter, radiation, and dark energy respectively. With this parametrization, Equation 1.5 has the solution $\rho_w(a) \propto a^{-3(1+w)}$. Defining $\Omega_{w,0} = \rho_{w,0}/\rho_\mathrm{c}$ where the critical density of the universe is given by $\rho_\mathrm{c} \equiv \frac{3H_0^2}{8\pi G}$, allows us to write the expansion history of the universe (Equation 1.4), hence implicitly the scale factor $a(t)$, as

$$H^2 = H_0^2 \sum_w \Omega_{w,0} a^{-3(1+w)}. \tag{1.6}$$

This equation gives the mean expansion history of the universe, and at the low redshifts probed by Type Ia Supernovae, it provides a direct constraint on H_0, $\Omega_{\mathrm{m},0}$, and $\Omega_{\Lambda,0}$. Note that deviations from flatness are defined as though there were an additional component $\Omega_{K,0} \equiv 1 - \Omega_{\mathrm{m},0} - \Omega_{\Lambda,0} - \Omega_{\mathrm{r},0}$ with $w = -\frac{1}{3}$.

1.3 The Cosmic Microwave Background

With the tools of general relativity and an understanding of how photons interact with fluids of various forms (baryonic matter, dark matter, and dark energy), it is possible to take the conceptually simple idea of sound waves in an expanding universe and predict the distribution of matter after a certain amount of time has elapsed. To understand our observations of the universe, we must develop a framework that can be used to characterize the photons we can see, as well as a framework that can explain how these data are related to the underlying distribution of energy in the observable universe.

Our observations are a single realization of a random process, so to make sense of the maps we must analyze them statistically, using power spectra. The brightness of the CMB can be described by maps of the intensity, linear polarization, and circular polarization, parametrized by the Stokes parameter vector $\boldsymbol{m}(\hat{\boldsymbol{n}}) = (I, Q, U, V)$. The maps can be described by spherical harmonics $\mathbf{a}_{\ell m} = (a^T_{\ell m}, a^E_{\ell m}, a^B_{\ell m}, a^V_{\ell m})$ and have an azimuthal average

$$\hat{\boldsymbol{C}}_\ell = \frac{1}{2\ell + 1} \sum_m \mathbf{a}^\dagger_{\ell m} \mathbf{a}_{\ell m}. \tag{1.7}$$

Standard cosmological models assume that the $\mathbf{a}_{\ell m}$ are Gaussian distributed, so the variables $(2\ell + 1)\hat{\boldsymbol{C}}_\ell$ are draws from a Wishart distribution with scale matrix $\boldsymbol{C}_\ell$ and $2\ell + 1$ degrees of freedom.[1] In the temperature-only case $\hat{C}_\ell / C_\ell$ is distributed as the more familiar χ^2 distribution with $2\ell + 1$ degrees of freedom.

The source of these brightness fluctuations are variations in density in the early

[1] Given n draws from a p-dimensional Gaussian distribution $\boldsymbol{x}_i \sim \mathcal{N}(\mathbf{0}, \boldsymbol{V})$, the $p \times p$ matrix $\boldsymbol{S} = \sum_{i=1}^n \boldsymbol{x}_i^T \boldsymbol{x}_i$ is a draw from a Wishart distribution with n degrees of freedom and $p \times p$ scale matrix $\boldsymbol{V}$, denoted $\boldsymbol{S} \sim \mathcal{W}_p(n, \boldsymbol{V})$. Therefore, $(2\ell + 1)\hat{\boldsymbol{C}}_\ell \sim \mathcal{W}_{2\ell+1}(4, \boldsymbol{C}_\ell)$.

universe, described in Fourier space with scalar power spectrum $\Delta^{(S)}(k) \propto A_s k^{n_s - 1}$, and potentially gravitational wave fluctuations with their tensor power spectrum $\Delta^{(T)}(k) \propto A_t k^{n_t}$.

Using the Boltzmann equation for the time evolution of a particle's distribution function in phase space, it is possible to evolve an initial set of perturbations from the radiation-dominated epoch of the universe to today. A set of fluctuations in Fourier space $\Delta_X(k, t)$ can be related to the on-sky power spectrum

$$C_\ell^{XY} = \pi^2 T_0^2 \int k^2 \, \mathrm{d}k \, \Delta_{X,\ell}(k, t_0) \Delta_{Y,\ell}(k, t_0)$$

where $X \in \{T, E, B\}$. There are no predictions for circular polarization V in standard cosmological models, so we will not focus on it in this introduction, although it is addressed in more detail in King and Lubin (2016), Montero-Camacho and Hirata (2018), and others. The evolution of Δ depends on factors like the amplitude and shape of the fluctuations that set the initial conditions (A_s, A_t, n_s, n_t), the content of the universe (Ω_b, Ω_c, Ω_Λ), and the optical depth as a function of time, $\tau(t) = \int_t^{t_0} n_\mathrm{e}(t') \sigma_\mathrm{T} c \, \mathrm{d}t'$, typically reported evaluated at the last scattering surface shortly after recombination, $\tau(t_\mathrm{lss})$.

1.4 The Characterization of Photons

The measured intensity at a position in the universe $\boldsymbol{x}$, looking at a direction $\hat{\boldsymbol{n}}$, at a time t, with a frequency ν, and detector orientation γ, is denoted $\mathcal{I}(\boldsymbol{x}, \hat{\boldsymbol{n}}, t, \nu, \gamma)$, where the quantity measured is fundamentally the measured power per unit frequency per solid angle. In this framework, the discovery of the Cosmic Microwave Background by Penzias and Wilson (1965) amounted to measuring $\iint \mathrm{d}\gamma \, \mathrm{d}\hat{\boldsymbol{n}} \, \mathcal{I}(0, \hat{\boldsymbol{n}}, t_0, 4.08\,\mathrm{MHz}, \gamma)$

and attributing the measured intensity to a blackbody with temperature 3.5 K. The *COBE*/FIRAS experiment sampled this function from frequencies $\nu = 30\,\mathrm{GHz}$ to 2190 GHz, detecting no deviations from a pure blackbody radiation with $T = 2.72548 \pm 0.00057$ K (Mather et al., 1994; Fixsen, 2009).

1.4.1 Observables

An electromagnetic wave that propagates in the z direction is described by the electric field vector, which is the real part of

$$E_x(t) = a_x(t)e^{i[\omega t - \theta_x(t)]}, \qquad E_y(t) = a_y(t)e^{i[\omega t - \theta_y(t)]} \tag{1.8}$$

where ω is the frequency of the wave, a_x are the real amplitudes, and $\theta_{x,y}$ are the phase differences. Correlation between these components implies a level of polarization that comes from a coherent phase difference between the x and y components. The Stokes parameters are given by the time averages

$$I \propto \langle E_x E_x^* \rangle + \langle E_y E_y^* \rangle \qquad = \langle a_x^2 \rangle + \langle a_y^2 \rangle \tag{1.9}$$

$$Q \propto \langle E_x E_x^* \rangle - \langle E_y E_y^* \rangle \qquad = \langle a_x^2 \rangle - \langle a_y^2 \rangle \tag{1.10}$$

$$U \propto \langle E_x E_y^* \rangle + \langle E_y E_x^* \rangle \qquad = \langle 2a_x a_y \cos(\theta_x - \theta_y) \rangle \tag{1.11}$$

$$V \propto \frac{1}{i}(\langle E_x E_y^* \rangle - \langle E_y E_x^* \rangle) \qquad = \langle 2a_x a_y \sin(\theta_x - \theta_y) \rangle \tag{1.12}$$

where the proportionality constant is given by $c^2\epsilon_0$, where ϵ_0 is the permittivity of free space. Q and U describe the linear polarization, and are coordinate-dependent spin-2 quantities. The total intensity is given by I, proportional to the total energy flux of an electromagnetic wave. The circular polarization V corresponds to the degree to

which there is a coherent phase difference between the E_x and E_y components of the electric field vector.

Both I and V are coordinate-independent and spin-0. We can see this by rotating to a new observer coordinate frame rotated by an angle α such that $E'_x = E_x \cos\alpha + E_y \sin\alpha$ and $E'_y = E_y \cos\alpha - E_x \sin\alpha$, giving transformed quantities

$$I' = I \tag{1.13}$$

$$Q' = Q\cos 2\alpha + U \sin 2\alpha \tag{1.14}$$

$$U' = U\cos 2\alpha - Q \sin 2\alpha \tag{1.15}$$

$$V' = V. \tag{1.16}$$

Now that we have our definitions of Q and U, and know that they are coordinate-dependent, we introduce the scalar counterparts, the E- and B-modes. The combinations $Q \pm iU$ are spin-2 quantities, i.e. under a rotation α about the z-axis, the linear polarization transforms as

$$(Q \pm iU)' = e^{\mp 2i\alpha}(Q \pm iU). \tag{1.17}$$

Therefore, a full-sky map of the Stokes parameters I, Q, U, V can be decomposed as

$$T(\hat{\boldsymbol{n}}) = \sum_{\ell,m} a_{T,\ell m} Y_{\ell m}(\hat{\boldsymbol{n}}) \tag{1.18}$$

$$(Q \pm iU)(\hat{\boldsymbol{n}}) = \sum_{\ell m} a_{\pm 2,\ell m\ \pm 2} Y_{\ell m}(\hat{\boldsymbol{n}}) \tag{1.19}$$

$$V(\hat{\boldsymbol{n}}) = \sum_{\ell,m} a_{V,\ell m} Y_{\ell m}(\hat{\boldsymbol{n}}). \tag{1.20}$$

The $Y_{\ell m}$ are the usual spherical harmonics, and ${}_{\pm 2}Y_{\ell m}$ are the spin-2 weighted spherical harmonics, both of which are orthonormal functions that are a complete basis on the surface of a sphere. The $a_{\pm 2,\ell m}$ can be combined to create a spin-0 combination,

$$a_{E,\ell m} = -\frac{1}{2}(a_{2,\ell m} + a_{-2,\ell m}), \qquad a_{B,\ell m} = \frac{i}{2}(a_{2,\ell m} - a_{-2,\ell m})$$

so that we can make maps of so-called E-modes and B-modes,

$$E(\hat{\boldsymbol{n}}) = \sum_{\ell m} a_{E,\ell m} Y_{\ell m}(\hat{\boldsymbol{n}}), \qquad B(\hat{\boldsymbol{n}}) = \sum_{\ell m} a_{B,\ell m} Y_{\ell m}(\hat{\boldsymbol{n}}).$$

The names "E-modes" and "B-modes" are given because the linear polarization vector in a pure E-mode is locally radially symmetric and is curl-free like a static electric field, while in a pure B-mode the polarization vector field is gradient free, like a static magnetic field.

The intensity and polarization maps are realizations of a Gaussian random field, so it makes sense to take a power spectrum so that we can compare with theoretical predictions. Given a full-sky measurement, one may construct vectors $\mathbf{a}_{\ell m} = (a_{T,\ell m}, a_{E,\ell m}, a_{B,\ell m}, a_{V,\ell m})$ and take the azimuthal average of their outer product;

$$\hat{\boldsymbol{C}}_\ell = \frac{1}{2\ell+1}\sum_m \mathbf{a}^\dagger_{\ell m}\mathbf{a}_{\ell m} = \begin{pmatrix} \hat{C}_\ell^{\mathrm{TT}} & \hat{C}_\ell^{\mathrm{TE}} & \hat{C}_\ell^{\mathrm{TB}} & \hat{C}_\ell^{\mathrm{TV}} \\ & \hat{C}_\ell^{\mathrm{EE}} & \hat{C}_\ell^{\mathrm{EB}} & \hat{C}_\ell^{\mathrm{EV}} \\ & & \hat{C}_\ell^{\mathrm{BB}} & \hat{C}_\ell^{\mathrm{BV}} \\ & & & \hat{C}_\ell^{\mathrm{VV}} \end{pmatrix}. \tag{1.21}$$

Standard cosmological models treat the individual $\mathbf{a}_{\ell m}$ as Gaussian random variables, uncorrelated between different ℓ and m. Each $\hat{C}_\ell^{\mathrm{XY}}$ has mean C_ℓ^{XY} and variance $\frac{1}{2\ell+1}[(C_\ell^{\mathrm{XY}})^2 + C_\ell^{\mathrm{XX}}C_\ell^{\mathrm{YY}}]$, and the matrix $\hat{\boldsymbol{C}}_\ell$ on the whole is described by the inverse-Wishart distribution.

In order to construct a useful framework to account for polarization, it is helpful to

decompose the intensity into the form $\mathcal{I}(\hat{\boldsymbol{n}}, \gamma) = e_j^* \mathcal{I}_{ij} e_i$ where $\mathcal{I}_{ij}$ is the intensity matrix and $\boldsymbol{e}(\gamma)$ are the polarization vectors that characterize the detector's polarization orientation. The dimensionless intensity matrix J_{ij} is given by

$$a^4(t)\bar{\rho}_\gamma(t) J_{ij}(\boldsymbol{x}, -\hat{\boldsymbol{n}}, t) \equiv \mathcal{I}_{ij}(\boldsymbol{x}, \hat{\boldsymbol{n}}, t) - \bar{\mathcal{I}}_{ij}(t). \tag{1.22}$$

For a photon moving in the $\hat{p} = -\hat{\boldsymbol{z}}$ direction, J_{ij} can be written in the form

$$J_{ij}(0, -\hat{\boldsymbol{z}}, t_0) = \frac{2}{T_0} \begin{pmatrix} \Delta T(\hat{\boldsymbol{z}}) + Q(\hat{\boldsymbol{z}}) & U(\hat{\boldsymbol{z}}) - iV(\hat{\boldsymbol{z}}) & 0 \\ U(\hat{\boldsymbol{z}}) + iV(\hat{\boldsymbol{z}}) & \Delta T(\hat{\boldsymbol{z}}) - Q(\hat{\boldsymbol{z}}) & 0 \\ 0 & 0 & 0 \end{pmatrix}.$$

In general, the Stokes parameters are related to the intensity matrix

$$\Delta T(\hat{\boldsymbol{n}}) = \frac{T_0}{4} J_{ii}(0, -\hat{\boldsymbol{n}}, t_0) \tag{1.23}$$

$$Q(\hat{\boldsymbol{n}}) \pm iU(\hat{\boldsymbol{n}}) = \frac{T_0}{2} e_{\pm i}(\hat{\boldsymbol{n}}) e_{\pm j}(\hat{\boldsymbol{n}}) J_{ij}(0, -\hat{\boldsymbol{n}}, t_0) \tag{1.24}$$

$$V(\hat{\boldsymbol{n}}) = \frac{T_0}{4} e_{-i}(\hat{\boldsymbol{n}}) e_{+j}(\hat{\boldsymbol{n}}) \big(J_{ij}(0, -\hat{\boldsymbol{n}}, t_0) - J_{ji}(0, -\hat{\boldsymbol{n}}, t_0) \big) \tag{1.25}$$

where the basis vector for polarization are given by

$$\boldsymbol{e}_\pm(\hat{\boldsymbol{n}}) = \frac{1}{\sqrt{2}} (\hat{\boldsymbol{\theta}} \pm i\hat{\boldsymbol{\phi}}) \tag{1.26}$$

which can be verified straightforwardly by comparing to the $\hat{\boldsymbol{z}}$ case.

A polarization-sensitive detector will detect polarization projected in the direction $\boldsymbol{e}(\gamma) = \hat{\boldsymbol{x}} \cos\gamma + \hat{\boldsymbol{y}} \sin\gamma$. The intensity we observe in the direction $\hat{\boldsymbol{z}}$ can be obtained using the differential fluctuations $\mathcal{I}(0, \hat{\boldsymbol{z}}, \gamma) - \bar{\mathcal{I}}$. The total detector power is given by

$$d \propto \frac{T_0}{2} e_i J_{ij} e_j = \Delta T + Q \cos 2\gamma + U \sin 2\gamma.$$

In general, a single detector is sensitive to only linear polarization states. The CLASS experiment is sensitive to circular polarization by transforming local V into local Q/U using its Variable-delay Polarization Modulator (VPM, Krejny et al., 2006; Chuss et al., 2012). The total power deposited on the detector is maximized when $\gamma = \frac{1}{2}\arctan\frac{U}{Q}$, which we refer to as polarization angle.

1.4.2 Perturbation Theory in General Relativity

The discussion in section 1.2 solved Einstein's equation $G_{\mu\nu} = 8\pi G T_{\mu\nu}$ assuming the universe is perfectly homogeneous in space as it evolved in time. Here we relax this assumption and consider first-order perturbations, corresponding to the more complicated equation

$$\delta G_{\mu\nu} = 8\pi G\, \delta T_{\mu\nu}. \tag{1.27}$$

Following the full details of this derivation will only distract from the main purpose of this introduction, so what follows will mostly be an outline of essential results interconnected by physical arguments. Much of this section is an abridged version of §2 of Flauger (2009), which goes over much of this in more detail and with more thorough background.

In Cartesian coordinates, the metric is given by

$$g_{\mu\nu}(t, \boldsymbol{x}) = \bar{g}_{\mu\nu}(t) + \delta g_{\mu\nu}(t, \boldsymbol{x}).$$

For a flat universe,

$$\bar{g}_{00} = -c^2, \qquad \bar{g}_{0i} = \bar{g}_{i0} = 0, \qquad \bar{g}_{ij} = \delta_{ij} a(t)^2.$$

The metric fluctuations can be parametrized as

$$\delta g_{00} = -E$$

$$\delta g_{0i} = a[\partial_i F + G_i]$$

$$\delta g_{ij} = a^2[A\delta_{ij} + \partial_i\partial_j B + \partial_i C_j + \partial_j C_i + D_{ij}]. \tag{1.28}$$

The stress energy tensor for a fluid is given by $T_{\mu\nu} = pg_{\mu\nu} + (p+\rho)u_\mu u_\nu + \pi_{\mu\nu}$, where u_μ is the velocity 4-vector, p pressure, ρ energy density, and $\pi_{\mu\nu}$ the anisotropic inertia that represents deviations from a perfect fluid. The first-order perturbation to the stress energy tensor is given by

$$\delta T_{00} = -\bar{\rho}\,\delta g_{00} + \delta\rho$$

$$\delta T_{0i} = \bar{p}\,\delta g_{0i} - (\bar{\rho} + \bar{p})\,\delta u_i$$

$$\delta T_{ij} = \bar{p}\,\delta g_{ij} + a^2\delta_{ij}(\delta p + \pi_{ij}). \tag{1.29}$$

It is occasionally convenient to decompose these quantities into trace ("scalar"), divergenceless ("vector") and traceless ("tensor") components, i.e. $\delta u_i = \partial_i \delta u^S + \delta u_i^V$ and $\pi_{ij} = \partial_i\partial_j\pi^S + \partial_i\pi_j^V + \partial_j\pi_i^V + \pi_{ij}^T$, and whose tensor and vector components satisfy

$$\partial_i\pi_i^V = \partial_i\delta u_i^V = 0, \qquad \partial_i\pi_{ij}^T = \pi_{ii}^T = 0, \tag{1.30}$$

respectively, where S, V, and T label "scalar","vector", and "tensor", respectively. Here all quantities follow the usual rules for covariant tensors under a coordinate

transformation $x^\mu \to x'^\mu$,

$$\pi'^V_\rho(x') = \pi_\mu(x)^V \frac{\partial x^\mu}{\partial x'^\rho}, \qquad \pi'^T_{\rho\sigma}(x') = \pi^T_{\mu\nu}(x)\frac{\partial x^\mu}{\partial x'^\rho}\frac{\partial x^\nu}{\partial x'^\sigma}. \tag{1.31}$$

With these definitions in hand, the dynamics of the universe's perturbations can be computed by calculating the Christoffel symbols, Ricci tensor, and Riemann curvature. The results of this are as follows;

$$-\frac{\nabla^2}{a^2}A + 3H\dot{A} + H\nabla^2\dot{B} = 8\pi G\,\delta\rho \tag{1.32}$$

$$\dot{A} = 8\pi G(\bar{\rho} + \bar{p})\,\delta u \tag{1.33}$$

$$\frac{1}{2}\frac{\nabla^2}{a^2}A - \ddot{A} - 3H\dot{A} - \frac{1}{2}\nabla^2\ddot{B} - \frac{3}{2}H\nabla^2\dot{B} = 8\pi G\,\delta p \tag{1.34}$$

$$-A + a^2\ddot{B} + 3a\dot{a}\dot{B} = 16\pi G a^2\,\pi^S \tag{1.35}$$

$$\nabla^2\dot{C}_i = -16\pi G(\bar{\rho} + \bar{p})\,\delta u^V_i \tag{1.36}$$

$$\ddot{C}_i + 3H\dot{C}_i = 16\pi G\pi^V_i \tag{1.37}$$

$$\ddot{D}_{ij} + 3H\dot{D}_{ij} - \frac{\nabla^2}{a^2}D_{ij} = 16\pi G\pi^T_{ij}. \tag{1.38}$$

The analogous equations for the smooth universe are all zero, except for Equation 1.32 and Equation 1.34, which correspond to the Friedmann equations $H^2 = \frac{8\pi G}{3}\rho$ and $\frac{\ddot{a}}{a} + \frac{4\pi G}{3}(\rho + 3p) = 0$. Equation 1.32 through Equation 1.35 are the standard equations used to compute the evolution of scalar perturbations through cosmic time, and are used to predict the standard power spectra. Equation 1.38 encodes the evolution of tensor fluctuations in the metric. We write these equations using the synchronous gauge, for which $\delta g_{00} = \delta g_{0i} = 0$, i.e. $E = F = 0$. This is in contrast with the

Newtonian gauge, with $E = 2\Phi$ and $A = -2\Psi$, where $\Phi(\boldsymbol{x}, t) \simeq -\Psi(\boldsymbol{x}, t)$ is the Newtonian gravitational potential. The synchronous gauge is more computationally tractable and is used in the common numerical codes (`CAMB`, Lewis, Challinor, and Lasenby 2000, `CLASS`, Blas, Lesgourgues, and Tram 2011), so we use it here for comparison with these works.

Perturbations to the covariant conservation of the stress-energy tensor $\nabla_\mu T^\mu_\nu = 0$ gives two equations for the scalar modes, energy conservation, the $\nu = 0$ component

$$\dot{\delta\rho} + 3H(\delta\rho + \delta p) + \frac{\nabla^2}{a^2}[(\bar{\rho} + \bar{p})\delta u + a\dot{a}\pi^S] + \frac{1}{2}(\bar{\rho} + \bar{p})(3\dot{A} + \nabla^2\dot{B}) = 0 \tag{1.39}$$

and momentum conservation, where the spatial component of $\nabla_\mu T^\mu_\nu = 0$ can be split into scalar modes

$$\dot{\delta p} + \nabla^2\pi^S + \frac{1}{a^3}\frac{\partial}{\partial t}[a^3(\bar{\rho} + \bar{p})\delta u] = 0, \tag{1.40}$$

and vector modes

$$\nabla^2\pi^V_i + \frac{1}{a^3}\frac{\partial}{\partial t}[a^3(\bar{\rho} + \bar{p})\delta u^V_i] = 0. \tag{1.41}$$

Equation 1.37 and Equation 1.41 demonstrate that vector modes decay rapidly in time if there is no anisotropic stress, and vector modes only come into play if they are continuously generated, which is not a feature of standard cosmological models. The only analogous nonzero component in the homogeneous universe is $\dot{\rho} + 3H(\rho + p) = 0$.

Denoting all scalar quantities $X(t, \boldsymbol{x}) \in \{\delta\rho(t, \boldsymbol{x}), \delta p(t, \boldsymbol{x}), \ldots\}$, we can write their general solution as a sum of Fourier modes

$$X(t, \boldsymbol{x}) = \int \mathrm{d}^3k\, \alpha(\boldsymbol{k}) X_k(t) e^{i\boldsymbol{k}\cdot\boldsymbol{x}} \tag{1.42}$$

where the $\alpha(\boldsymbol{k})$ are random parameters corresponding to the universe's initial conditions, and satisfy $\langle\alpha(\boldsymbol{k})^*\alpha(\boldsymbol{k}')\rangle = \delta(\boldsymbol{k} - \boldsymbol{k}')$, by construction.

The solution to the tensorial perturbations to the metric, $D_{ij}(t, \boldsymbol{x})$, can be written in terms of the Fourier decomposition

$$D_{ij}(t, \boldsymbol{x}) = \sum_{N,\lambda} \int \mathrm{d}^3k \, \beta_N(\boldsymbol{k}, \lambda) e_{ij}(\hat{\boldsymbol{k}}, \lambda) \, \mathcal{D}_{Nk}(t) e^{i\boldsymbol{k}\cdot\boldsymbol{x}}. \tag{1.43}$$

There are only two independent modes, labeled N, and two gravitational wave helicities, $\lambda = \pm 2$. The modes $\beta_N(\boldsymbol{k}, \pm 2)$ are normalized such that

$$\langle \beta_N(\boldsymbol{k}, \lambda) \beta^*_{N'}(\boldsymbol{k}', \lambda') \rangle = \delta_{NN'} \delta_{\lambda\lambda'} \delta^3(\boldsymbol{k} - \boldsymbol{k}') \tag{1.44}$$

and the polarization tensor $e_{ij}(\hat{\boldsymbol{q}}, \pm 2)$, is such that if $\hat{\boldsymbol{k}} = \hat{\boldsymbol{z}}$

$$e_{11}(\hat{\boldsymbol{z}}, \pm 2) = -e_{22}(\hat{\boldsymbol{z}}, \pm 2) = \frac{1}{\sqrt{2}}, \qquad e_{12}(\hat{\boldsymbol{z}}, \pm 2) = e_{21}(\hat{\boldsymbol{z}}, \pm 2) = \pm \frac{i}{\sqrt{2}}.$$

If we decompose π^T_{ij} analogously, the tensor mode equation becomes

$$\ddot{\mathcal{D}}_{Nk} + 3\frac{\dot{a}}{a}\dot{\mathcal{D}}_{Nk} + \frac{k^2}{a^2}\mathcal{D}_{Nk} = 16\pi G \pi^T_{Nk}. \tag{1.45}$$

At large scales and in the case of no anisotropic inertia, this equation has two solutions, $\mathcal{D}^0_k$ constant and $\mathcal{D}^1_k \propto \int \mathrm{d}t \, a(t)^{-3}$. This second solution is negligible, so we write the solution to the tensor perturbations as

$$D_{ij}(t, \boldsymbol{x}) = \sum_{\lambda} \int \mathrm{d}^3k \, \beta(\boldsymbol{k}, \lambda) e_{ij}(\hat{\boldsymbol{k}}, \lambda) \mathcal{D}^0_k(t) e^{i\boldsymbol{k}\cdot\boldsymbol{x}}. \tag{1.46}$$

1.4.3 Scalar and Tensor Power Spectra

In this section, we will discuss the solution to the first-order perturbations of the collisional Boltzmann equation,

$$\frac{\mathrm{d}n^{ij}}{\mathrm{d}t} = C[n^{ij}]. \tag{1.47}$$

The derivation of these results is extensive and is deferred to section B.3. This section goes over the evolution of the phase space density for photons with ellipticity vectors in the i and j directions, n^{ij}, which is related to the dimensionless intensity matrix by

$$a^2 \bar{\rho}_\gamma J_{ij}(\boldsymbol{x}, \hat{\boldsymbol{p}}, t) = a^2 \int p \ \mathrm{d}^3\boldsymbol{p} \ \delta n^{ij}(\boldsymbol{x}, \boldsymbol{p}, t). \tag{1.48}$$

Note that throughout this section, we define $\tau(t) = \int_t^{t_0} n_e(t')\sigma_\mathrm{T} \, \mathrm{d}t' = \int \omega_c \, \mathrm{d}t'$ so that $\dot{\tau} = -n_e(t)\sigma_\mathrm{T}$ as opposed to the standard notation for reionization optical depth, $\tau = \tau(t_\mathrm{lss})$.

Scalar modes

We may decompose the intensity matrix into an unpolarized and a polarized component labeled $\Delta_T^{(S)}$ and $\Delta_P^{(S)}$ such that

$$J_{ij} = \alpha(\boldsymbol{k}) \left\{ \frac{1}{2} \left(\Delta_T^{(S)} - \Delta_P^{(S)} \right) (\delta_{ij} - \hat{p}_i \hat{p}_j) + \Delta_P^{(S)} \left[\frac{(\hat{k}_i - (\hat{k} \cdot \hat{p})\hat{p}_i)(\hat{k}_j - (\hat{k} \cdot \hat{p})\hat{p}_j)}{1 - (\hat{p} \cdot \hat{k})^2} \right] \right\}. \tag{1.49}$$

When this decomposition is used in the Boltzmann equation, we obtain these coupled differential equations for the scalar fluctuations

$$\dot{\Delta}_T^{(S)} + i \frac{k\mu}{a} \Delta_T^{(S)} = \dot{\tau} \left[\Delta_T^{(S)} - \frac{3}{4}(1 - \mu^2)\Pi - 3\Phi - \frac{4ik\mu}{a} \delta u_{Bk} \right] - 2\dot{A}_k + 2k^2\mu^2 \dot{B}_k \tag{1.50}$$

$$\dot{\Delta}_P^{(S)} + i \frac{k\mu}{a} \Delta_P^{(S)} = \dot{\tau} \left[\Delta_P^{(S)} - \frac{3}{4}(1 - \mu^2)\Pi \right] \tag{1.51}$$

where the directional dependence is encoded in the term $\mu = \hat{\boldsymbol{k}} \cdot \hat{\boldsymbol{p}}$. We have slipped in definitions of source functions such that

$$\int \frac{\mathrm{d}^2\hat{\boldsymbol{p}}}{4\pi} J_{ij}(\boldsymbol{k}, \hat{\boldsymbol{p}}, t) = \alpha(\boldsymbol{k}) \left[\delta_{ij}\Phi + \frac{1}{2} \hat{k}_i \hat{k}_j \Pi \right]$$

which can be written in terms of the Legendre coefficients

$$\Phi = \frac{1}{6}\left[2\Delta^{(S)}_{T,0} - \Delta^{(S)}_{T,2} - \Delta^{(S)}_{P,0} - \Delta^{(S)}_{P,2}\right] \tag{1.52}$$

$$\Pi = \Delta^{(S)}_{P,0} + \Delta^{(S)}_{T,2} + \Delta^{(S)}_{P,2} \tag{1.53}$$

where the Legendre decomposition is in general

$$f(k,\mu) = \sum_{\ell=0}^{\infty}(-i)^{\ell}(2\ell+1)P_{\ell}(\mu)f_{\ell}(k). \tag{1.54}$$

The solution of these differential equations is outside of the scope of this work, but there are a few notable features that can be pulled out. First, the equations are of an oscillatory form, with a friction term corresponding to the expansion of the universe. The forcing term is proportional to the changing optical depth $\dot{\tau} = -n_e(t)\sigma_{\mathrm{T}}$, and is hence dependent on the free electron density over cosmic time. This essentially creates a new source term during the epoch of reionization, and boosts the polarization signal at small k Fourier modes, hence low multipole values ℓ. This is known as the reionization peak, and is an important target for CMB polarization experiments. The initial conditions of the fluctuations come in when considering the temperature's monopole and quadrupole terms $\Delta^{(S)}_{T,0}$ and $\Delta^{(S)}_{T,2}$, which at early times dominate over the rest of the Legendre coefficients. The initial amplitude of these fluctuations is proportional to the quantity A_s in standard ΛCDM cosmology.

Tensor modes

The intensity matrix is decomposed as

$$J_{ij} = \frac{1}{2}(\delta_{ij}-\hat{p}_i\hat{p}_j)\hat{p}_k\hat{p}_l e_{kl}\left(\Delta^{(T)}_T + \Delta^{(T)}_P\right) + \left(e_{ij} - \hat{p}_i\hat{p}_k e_{kj} - \hat{p}_j\hat{p}_k e_{ik} + \hat{p}_i\hat{p}_j\hat{p}_k\hat{p}_l e_{kl}\right)\Delta^{(T)}_P \tag{1.55}$$

With this in hand, we can write down the coupled Boltzmann equations for temperature and polarization fluctuations due to tensor modes,

$$\dot{\Delta}_T^{(T)} + i\frac{k\mu}{a}\Delta_T^{(T)} = \dot{\tau}[\Delta_T^{(T)} - \Psi] - 2\dot{\mathcal{D}}_k \tag{1.56}$$

$$\dot{\Delta}_P^{(T)} + i\frac{k\mu}{a}\Delta_P^{(T)} = \dot{\tau}[\Delta_P^{(T)} + \Psi]. \tag{1.57}$$

Here the source function we have slipped in is defined by

$$\int \frac{\mathrm{d}^2\hat{\boldsymbol{p}}}{4\pi} J_{ij}(\boldsymbol{k}, \hat{\boldsymbol{p}}, t, \lambda) = -\frac{2}{3} e_{ij}\Psi$$

which in a Legendre decomposition is given by

$$\Psi = \frac{1}{10}\Delta_{T,0}^{(T)} + \frac{1}{7}\Delta_{T,2}^{(T)} + \frac{3}{70}\Delta_{T,4}^{(T)} - \frac{3}{5}\Delta_{P,0}^{(T)} + \frac{6}{7}\Delta_{P,2}^{(T)} - \frac{3}{70}\Delta_{P,4}^{(T)}. \tag{1.58}$$

This is qualitatively very similar to, and in fact simpler than, the equations for scalar fluctuations. From the perturbed Einstein field equation Equation 1.45, we know that the gravitational wave signal $\mathcal{D}_k$ is roughly constant, and its initial condition is usually given as proportional to A_t.

An often-used parameterization of ΛCDM fits for an amplitude of curvature fluctuations $\mathcal{R}_k^0$ at a pivot scale k_*,

$$\Delta_{\mathcal{R}}^2(k) = 4\pi|\mathcal{R}_k^0|^2 k^3 = A_s \left(\frac{k}{k_*}\right)^{n_s - 1}. \tag{1.59}$$

For tensor modes, we can approximate the tensor fluctuations by the dominant constant solution. We parametrize the shape of the tensor power law spectrum as

$$\Delta_{\mathcal{D}}^2(k) = 16\pi|\mathcal{D}_k^0|^2 k^3 = A_t \left(\frac{k}{k_*}\right)^{n_t}.$$

The relative amplitude of tensor fluctuations is parametrized by the tensor-to-scalar ratio r,

$$r(k) \equiv \frac{\Delta^2_{\mathcal{D}}(k)}{\Delta^2_{\mathcal{R}}(k)} \simeq \frac{A_t}{A_s}.$$

The tensor-to-scalar ratio is roughly scale-independent, and is usually set to the pivot scale $k_* = 0.05\,\mathrm{Mpc}^{-1}$, as we do throughout this work.

We can compute the multipole coefficients $C_\ell^{XY} \equiv \langle a_{X,\ell m} a^*_{Y,\ell m} \rangle$ using the dimensionless intensity matrix, so that

$$a_{T,\ell m} = \frac{T_0}{4} \int \mathrm{d}^2\hat{\boldsymbol{n}}\, Y^*_{\ell m}(\hat{\boldsymbol{n}}) J_{ii}(0, -\hat{\boldsymbol{n}}, t_0) \tag{1.60}$$

$$a_{\pm 2,\ell m} = \frac{T_0}{2} \int \mathrm{d}^2\hat{\boldsymbol{n}}\, {}_{\pm 2}Y^*_{\ell m}(\hat{\boldsymbol{n}}) e_{\pm,i}(\hat{\boldsymbol{n}}) e_{\pm,j}(\hat{\boldsymbol{n}}) J_{ij}(0, -\hat{\boldsymbol{n}}, t_0). \tag{1.61}$$

We first focus on the scalar modes, then the tensor modes. The dimensionless intensity matrix for scalar fluctuations is

$$J_{ij}(\boldsymbol{k}, \hat{p}, t) = \alpha(\boldsymbol{k}) \left\{ \frac{1}{2}(\Delta^{(S)}_T - \Delta^{(S)}_P)(\delta_{ij} - \hat{p}_i \hat{p}_j) + \Delta^{(S)}_P \left[\frac{(\hat{k}_i - (\hat{k}\cdot\hat{p})\hat{p}_i)(\hat{k}_j - (\hat{k}\cdot\hat{p})\hat{p}_j)}{1 - (\hat{p}\cdot\hat{k})^2} \right] \right\}$$

where the arguments of each Δ are $(k, \hat{k}\cdot\hat{p}, t)$. The trace of this function is $J_{ii}(\boldsymbol{k}, \hat{\boldsymbol{p}}, t) = \alpha(\boldsymbol{k})\Delta^{(S)}_T$, by construction. The polarization components, $e_{\pm,i} e_{\pm,j} J_{ij}$, can be simplified to the quantity

$$e_{\pm i} e_{\pm j} J_{ij} = \alpha(\boldsymbol{k}) \frac{(\boldsymbol{e}_\pm \cdot \hat{\boldsymbol{k}})^2}{1 - (\hat{\boldsymbol{p}}\cdot\hat{\boldsymbol{k}})^2}.$$

These expressions allow us to write down the expressions for the spherical harmonic transforms given the Fourier components $\Delta^{(S)}$;

$$a^{(S)}_{T,\ell m} = \frac{T_0}{4}\int \mathrm{d}^3\boldsymbol{k}\;\alpha(\boldsymbol{k})\int \mathrm{d}^2\hat{\boldsymbol{n}}\;Y^*_{\ell m}\Delta^{(S)}_T(k,-\hat{\boldsymbol{k}}\cdot\hat{\boldsymbol{n}},t_0) \tag{1.62}$$

$$a^{(S)}_{\pm2,\ell m} = \frac{T_0}{2}\int \mathrm{d}^3\boldsymbol{k}\;\alpha(\boldsymbol{k})\int \mathrm{d}^2\hat{\boldsymbol{n}}\;{}_{\pm2}Y^*_{\ell m}\frac{(\boldsymbol{e}_\pm\cdot\hat{k})^2}{1-(\hat{\boldsymbol{k}}\cdot\hat{\boldsymbol{n}})^2}\Delta^{(S)}_P(k,-\hat{\boldsymbol{k}}\cdot\hat{\boldsymbol{n}},t_0). \tag{1.63}$$

It is possible to obtain analytical expressions for the coefficients,

$$a^{(S)}_{T,\ell m} = \pi T_0 i^\ell\int \mathrm{d}^3\boldsymbol{k}\;\alpha(\boldsymbol{k})Y^*_{\ell m}(\hat{\boldsymbol{k}})\Delta^{(S)}_{T,\ell}(k,t_0) \tag{1.64}$$

$$a^{(S)}_{\pm2,\ell m} = -\pi T_0 i^\ell\int \mathrm{d}^3\boldsymbol{k}\;\alpha(\boldsymbol{k})Y^*_{\ell m}(\hat{\boldsymbol{k}})\Delta^{(S)}_{E,\ell}(k,t_0) \tag{1.65}$$

where we wrote the solutions in terms of the transfer functions,

$$\Delta^{(S)}_{T,\ell}(k) = -\int^{t_0}\mathrm{d}t\dot{\tau}e^{-\tau}\left\{\left[3\Phi-2a\frac{\mathrm{d}}{\mathrm{d}t}(a\dot{B}_k)+\frac{3}{4}\Pi\right]j_\ell(kr)-4k\left[\delta u_k/a+a\dot{B}_k/2\right]j'_\ell(kr)+\frac{3}{4}\Pi j''_\ell(kr)\right\}$$
$$-\int^{t_0}\mathrm{d}te^{-\tau}\frac{\mathrm{d}}{\mathrm{d}t}\left[2A_k+2a\frac{\mathrm{d}}{\mathrm{d}t}(a\dot{B}_k)\right]j_\ell(kr) \tag{1.66}$$

$$\Delta^{(S)}_{E,\ell}(k) = -\frac{3}{4}\sqrt{\frac{(\ell+2)!}{(\ell-2)!}}\int^{t_0}\mathrm{d}t\frac{\dot{\tau}e^{-\tau}\Pi}{k^2r^2}j_\ell(kr) \tag{1.67}$$

where j_ℓ is the spherical Bessel function.

For tensor fluctuations, the formulae are analogous, with

$$a^{(T)}_{T,\ell m} = \frac{T_0}{4}\sum_{\lambda=\pm2}\int \mathrm{d}^3\boldsymbol{k}\;\beta(\boldsymbol{k},\lambda)\int \mathrm{d}^2\hat{\boldsymbol{n}}\;Y^*_{\ell m}(\hat{\boldsymbol{n}})\hat{n}_i\hat{n}_j e_{ij}(\hat{\boldsymbol{k}},\lambda)\Delta^{(T)}_T(k,-\hat{\boldsymbol{k}}\cdot\hat{\boldsymbol{n}},t_0) \tag{1.68}$$

$$a^{(T)}_{\pm2,\ell m} = \frac{T_0}{2}\sum_{\lambda=\pm2}\int \mathrm{d}^3\boldsymbol{k}\;\beta(\boldsymbol{k},\lambda)\int \mathrm{d}^2\hat{\boldsymbol{n}},{}_{\pm2}Y^*_{\ell m}(\hat{\boldsymbol{n}})e_{\pm,i}(\hat{\boldsymbol{n}})e_{\pm,j}(\hat{\boldsymbol{n}})e_{ij}(\hat{\boldsymbol{k}},\lambda)\Delta^{(T)}_P(k,-\hat{\boldsymbol{k}}\cdot\hat{\boldsymbol{n}},t_0) \tag{1.69}$$

It is again possible to analytically marginalize over the directional dependence to obtain

$$a^{(T)}_{T,\ell m} = \pi T_0 i^\ell \frac{1}{\sqrt{2}} \sum_{\pm} \int \mathrm{d}^3\boldsymbol{k}\, \beta(\boldsymbol{k}, \pm 2)\, Y^*_{\ell m}(\hat{\boldsymbol{k}}) \Delta^{(T)}_{T,\ell}(k, t_0) \tag{1.70}$$

$$a^{(T)}_{\pm 2,\ell m} = -\pi T_0 i^\ell \frac{1}{\sqrt{2}} \sum_{\pm} \int \mathrm{d}^3\boldsymbol{k}\, \beta(\boldsymbol{k}, \pm 2)\, Y^*_{\ell m}(\hat{\boldsymbol{k}}) \left(\Delta^{(T)}_{E,\ell}(k, t_0) \pm i \Delta^{(T)}_{B,\ell}(k, t_0) \right). \tag{1.71}$$

The transfer functions for tensors are given by

$$\Delta^{(T)}_{T,\ell}(k, t_0) = \sqrt{\frac{(\ell+2)!}{(\ell-2)!}} \int^{t_0} \mathrm{d}t\, e^{-\tau} (2\dot{\mathcal{D}} - \dot{\tau}\Psi) \frac{j_\ell(kr)}{(kr)^2} \tag{1.72}$$

$$\Delta^{(T)}_{E,\ell}(k, t_0) = \int^{t_0} \mathrm{d}t\, \dot{\tau} e^{-\tau} \Psi(k, t) \left(12 + 8\rho \frac{\partial}{\partial \rho} - \rho^2 + \rho^2 \frac{\partial^2}{\partial \rho^2} \right) \frac{j_\ell(\rho)}{\rho^2} \bigg|_{\rho = kr} \tag{1.73}$$

$$\Delta^{(T)}_{B,\ell}(k, t_0) = -\int^{t_0} \mathrm{d}t\, \dot{\tau} e^{-\tau} \Psi \left(8\rho + 2\rho^2 \frac{\partial}{\partial \rho} \right) \frac{j_\ell(r\rho)}{\rho^2} \bigg|_{\rho = kr}. \tag{1.74}$$

It is worth pausing for a moment to note the differences between scalar and tensor modes, and why only tensor modes contribute to the B-mode transfer function. For both the tensor and scalar modes, the temperature fluctuations are given by the trace of the dimensionless intensity matrix J_{ii}, while the polarization components are given by $e_{\pm i} e_{\pm j} J_{ij}$. When we perform the analytical simplification, the polarization terms drop out of the scalar component, essentially because the source terms in the intensity matrix do not have any intrinsic directionality. The B-modes are generated by tensor perturbations because the polarization matrix e_{ij} from the metric includes contributions from every direction. When the equations and simplifications are performed, there are extra spin-weighted spherical harmonics that just do not simplify; these terms are there precisely because there is an off-diagonal contribution from the

metric fluctuations in the tensor fluctuations source terms.

The spherical harmonic decomposition in terms of Fourier modes is in general given by

$$C_{XY,\ell} = \pi^2 T_0^2 \int k^2 \, \mathrm{d}k \, \Delta_{X,\ell}(k, t_0) \Delta_{Y,\ell}(k, t_0). \tag{1.75}$$

For tensor modes, the EB and TB spectra vanish because the positive and negative helicity gravitons are equal and opposite and cancel. They will only be non-zero in a parity violating theory.

Given very few input parameters, the expected scalar power spectra can be computed. The Fourier space power spectrum of the scalar fluctuations is given by an amplitude (A_s) and its power law index in Fourier space ($n_s - 1$). Assuming a spatially flat universe, the subsequent expansion depends on the interactions and hence the relative densities of radiation (Ω_r), baryonic matter (Ω_b), and dark matter (Ω_c), and the rate at which their densities are increasing (H_0). The presence of free electrons since the CMB photons were emitted at last scattering reduces the amplitude of the fluctuation by the reionization optical depth τ. The amplitude of the power spectrum therefore makes the observed temperature power spectrum $A_s e^{-2\tau}$, a parameter combination that is very tightly constrained by high-ℓ C_ℓ^{TT} data. The onset of reionization induces polarization at large angular scales, and the epoch at which reionization occurs affects both the brightness and the apparent size of large angular scale fluctuations. This shifting of the amplitude and location of the reionization peak is demonstrated by the middle panel of Figure 1.1.

The tensor power spectrum is governed again by a power law power spectrum in Fourier space with amplitude A_t and spectral index n_t. The tensor fluctuations have non-zero power spectra, but all except the B-mode power spectra are dwarfed

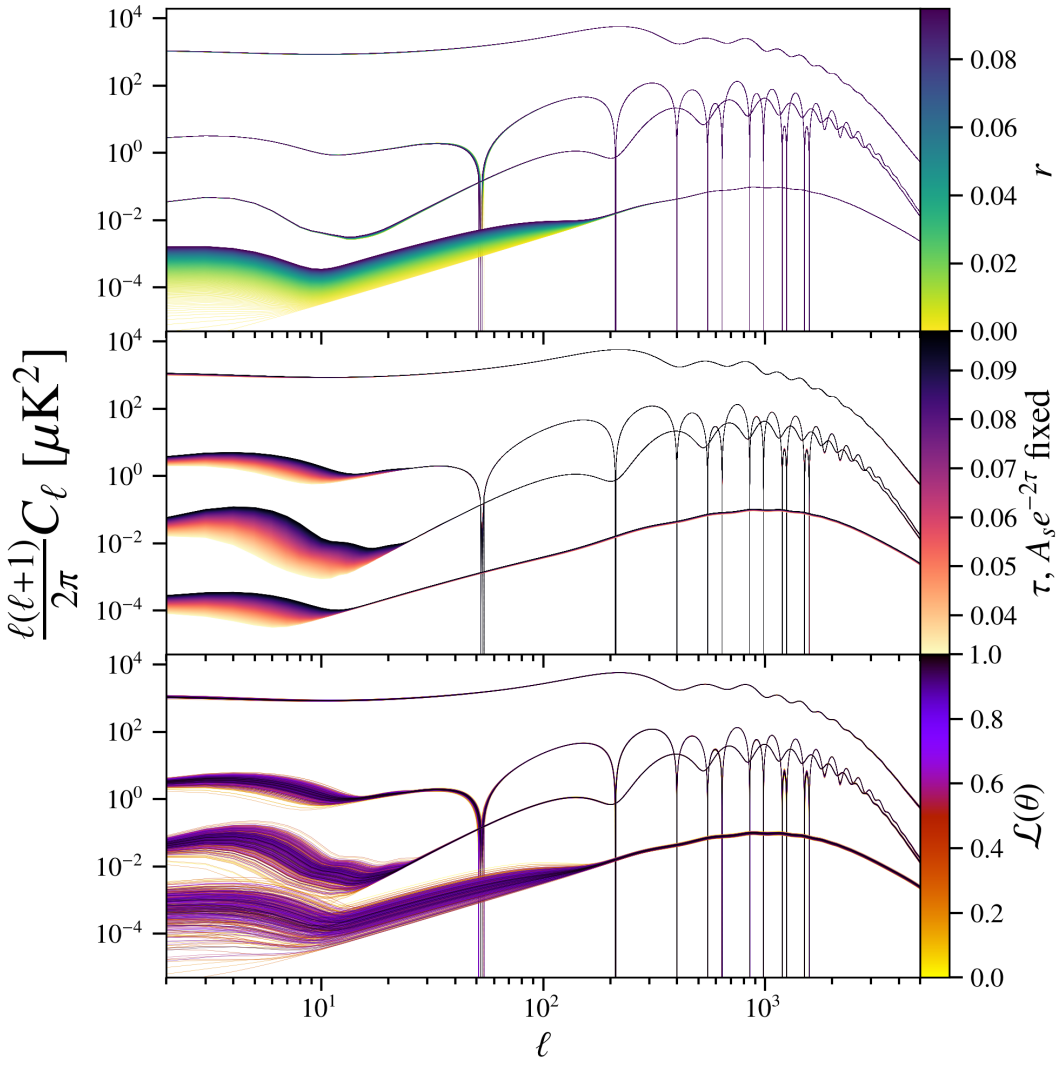

Figure 1.1: Theoretical power spectra with varying input cosmological parameters. Each of these plots displays C_ℓ^{TT}, C_ℓ^{TE}, C_ℓ^{EE}, and C_ℓ^{BB}, ordered by decreasing total power. In polarization-based power spectra, much of the variation comes from uncertainty in τ and r. The bottom panel shows theoretical power spectra drawn from the combined BICEP/*Planck* Monte Carlo Markov Chain analysis (BICEP2/Keck Collaboration et al., 2015), with $\tau = 0.08 \pm 0.02$ and $r = 0.02^{+0.03}_{-0.02}$.

by the scalar power spectrum. The B-mode amplitude at the reionization peak is also dependent on the reionization history, and from the B-mode reionization peak alone there is a degeneracy between r and τ.

While there are still uncertainties in all cosmological parameters that can be constrained by the CMB, the theoretical uncertainty in r and τ induce the most variation in the C_ℓ. I demonstrate this by plotting on the bottom panel of Figure 1.1 random draws from the best-fit parameters allowed by the joint BICEP2/Keck Collaboration et al. (2015) analysis. Most of the variation in these curves comes from the uncertainty in τ and r.

1.5 Galactic Sources of Microwave Emission

In order to make accurate maps of the Cosmic Microwave Background, it is necessary to remove intervening sources of microwave emission. Because extragalactic sources of microwave emission do not currently affect the determination of parameters related to inflation and reionization, they will not be discussed further. The remainder of the emission that concerns us is from inside of the Milky Way. In both intensity and polarization, the minimum contribution from Galactic foregrounds is between 60 and 100 GHz, depending on angular scale and sky fraction (Figure 1.2). This is a primary consideration in the design of CMB experiments.

1.5.1 Synchrotron

Synchrotron emission is generated by relativistic electrons being accelerated by the Galactic magnetic field (Rybicki and Lightman, 1979). Because of the inherent directionality of the underlying physics, synchrotron emission can be highly polarized,

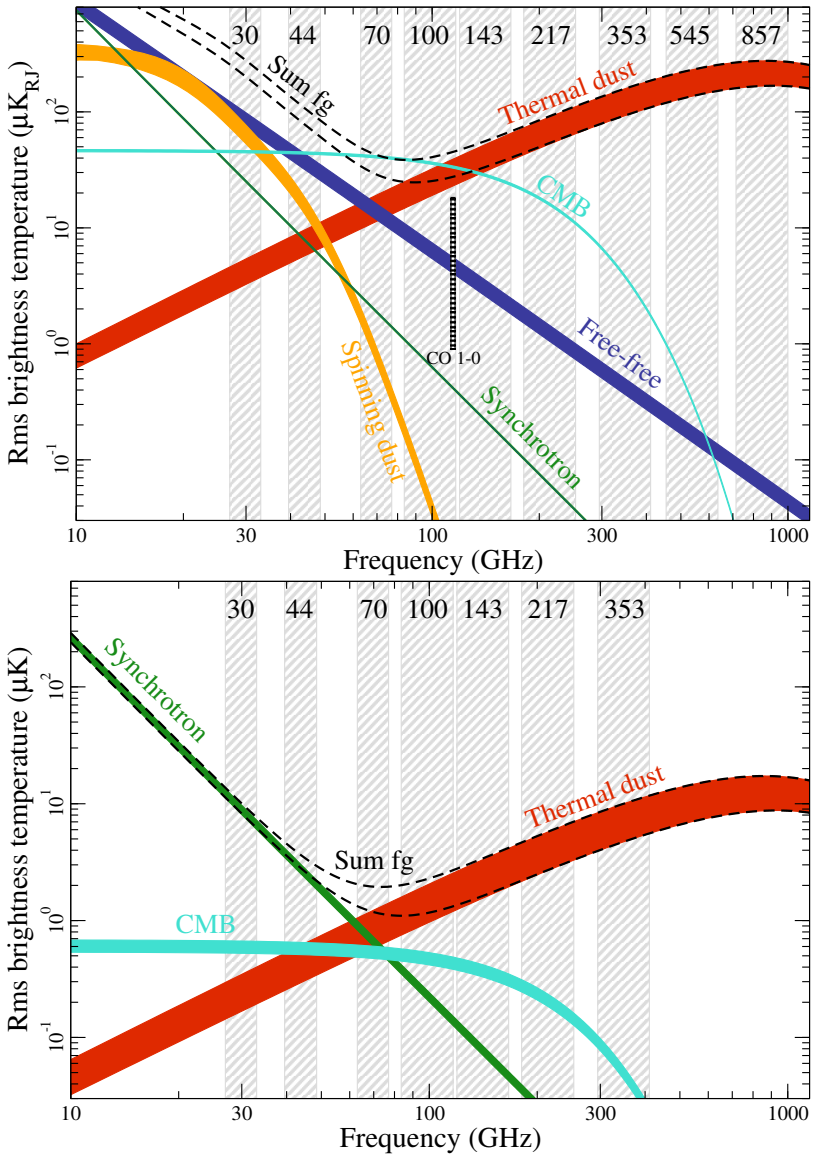

Figure 1.2: Summary of all measured Galactic foregrounds. This figure is reproduced from Planck Collaboration (2015a). This figure shows the root mean square brightness of each of the components, with the upper and lower lines using $f_{\rm sky}$ = 93% and 81% respectively for intensity, and 93% and 71% for polarization. The temperature (polarization) map was smoothed using a FWHM of 1° (40′).

and in fact can reach a polarization fraction of 70% in a perfectly regular magnetic field (Pacholczyk, 1970). Above 20 GHz, the synchrotron emission can be approximated by a power law with a spectral index $\beta_S \simeq -3$, although synchrotron self-absorption causes flattening at lower frequencies (Strong, Orlando, and Jaffe, 2011; Orlando and Strong, 2013, `GALPROP`). The power law index of the synchrotron spectral index is known to vary spatially, with $-3 \lesssim \beta_S \lesssim -2.5$ (Fuskeland et al., 2014). The global constraints on synchrotron intensity and polarization are plotted as green curves in the top and bottom panels of Figure 1.2. In multipole space, the polarized power spectra roughly scale as $C_\ell \propto \ell^{-2.6}$ (Thorne et al., 2017). The measured power spectra and their best-fit model are displayed in the left panel of Figure 1.3.

1.5.2 Thermal dust

The majority of dust in the Milky Way is in equilibrium at a temperature of 20 K. This cold neutral medium radiates as a modified blackbody with emissivity index β_D (Planck Collaboration, 2015a). Magnetic fields can align the major axes of aspherical dust grains, causing emission to be preferentially generated perpendicular to the local magnetic field, yielding a net polarization ranging from $1\% \lesssim p \lesssim 20\%$ (Planck Collaboration et al., 2015a; Planck Collaboration et al., 2015b). Polarized thermal dust has been measured by *Planck* using 100, 143, 217, and 353 GHz maps, and their angular scale dependence is consistent with a power law, $C_\ell^{\mathrm{EE/BB}} \propto \ell^\alpha$ with $\alpha_{\mathrm{EE}} = -2.42 \pm 0.02$ and $\alpha_{\mathrm{BB}} = -2.54 \pm 0.02$, while the frequency dependence $\beta_D = 1.53 \pm 0.02$ is consistent with a constant spectral energy distribution across the sky (Planck Collaboration et al., 2018). The global constraints on thermal dust intensity and polarization are plotted as red curves in the top and bottom panels

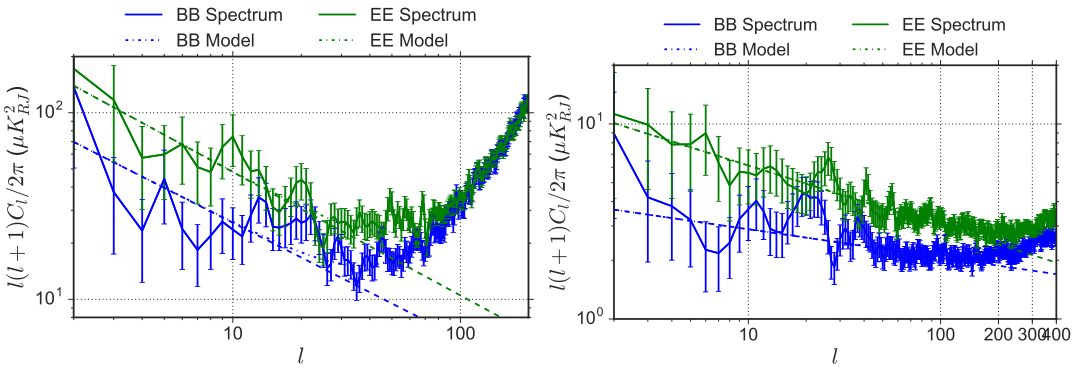

Figure 1.3: Multipole dependence of polarized foregrounds. This figure is reproduced from Thorne et al. (2017). On the left panel the power spectrum of the best-fit synchrotron model using the *WMAP* polarization analysis mask is displayed, for which the best-fit slopes of $\frac{\ell(\ell+1)}{2\pi}C_\ell = A\ell^\gamma + N\frac{\ell(\ell+1)}{2\pi}$ (where A and N are amplitude and noise terms) are $\gamma^{\mathrm{S,EE}} = -0.66$ and $\gamma^{\mathrm{S,BB}} = -0.62$. The right panel displays the power spectrum of the best-fit dust model using the *Planck* Gal 80 Galactic plane mask, and has $\gamma^{\mathrm{D,EE}} = -0.31$ and $\gamma^{\mathrm{D,BB}} = -0.15$.

of Figure 1.2. In multipole space, the polarized power spectra roughly scale as $C_\ell \propto \ell^{-2.3}$ (Thorne et al., 2017). The measured power spectra and their best-fit model are displayed in the right panel of Figure 1.3.

1.5.3 Spinning dust

If a dust grain has an intrinsic electric dipole, the changing local electric field will emit microwave radiation (Erickson, 1957; Draine and Lazarian, 1998). The precise spectral emission depends on dust grain properties. Although spinning dust does align with magnetic fields, energy dissipation causes the level of grain alignment to decrease, lowering the theoretical polarization fraction to be below 3%, with current measurements limiting $p \lesssim 1\%$ (Hoang, 2015). The frequency dependence is displayed in Figure 1.2, and its peak at ~ 40 GHz and steep dropoff could complicate estimates of polarized synchrotron emission, but the low limits on polarization fraction imply this will not be a factor for the current generation of CMB experiments'

sensitivity levels.

1.5.4 Free-free emission

Free-free radiation comes from the collision of electrons and ions, and is physically very well understood (Rybicki and Lightman, 1979). This emission is brightest in hot ionized regions with high emission measure, EM $\propto \int n_e^2 \, \mathrm{d}\ell$. The process itself is intrinsically direction independent, although in HII regions the gradient in n_e at the edges of the regions can theoretically induce polarization, but there is currently no evidence for polarized free-free emission (Macellari et al., 2011).

1.6 The State of the Field

Since the discovery of the Cosmic Microwave Background, there has been enormous progress in the characterization of this radiation field. With the *COBE*/FIRAS experiment, the CMB has been determined to be the most pure blackbody found in nature, with deviations in Compton-y parameter and chemical potential μ constrained to be $|y| \lesssim 10^{-5}$ and $|\mu| \lesssim 10^{-4}$ (Mather et al., 1994), although there are expected deviations from this that can be detected, and could yield a window into new physics (Chluba and Sunyaev, 2012). The CMB's temperature anisotropies on the full sky have been characterized exquisitely by the *WMAP* (Bennett et al., 2013) and *Planck* (Planck Collaboration et al., 2016) experiments up to $\ell \lesssim 2000$, while ACT and SPT have made small-scale temperature measurements up to $\ell \lesssim 10,000$ (Louis et al., 2017; George et al., 2015). E-mode measurements have also been made at all scales, although the constraints at greater than degree scales are still quite noisy (Bennett et al., 2013; Planck Collaboration, 2015b). B-mode measurements at degree scales

and smaller have been made, but as of writing they are all consistent with scalar E-modes that have been reshuffled into B-modes by gravitational lensing (BICEP2 Collaboration et al., 2016).

The anisotropies of the CMB have been well characterized by a number of experiments. Angular power spectra from a subset of these experiments are displayed in Figure 1.4. Other than the remarkable agreement between the theoretical curves and the amassed data, there are two obvious concerns. First, the effect of the primordial gravitational waves in the B-mode power spectrum is almost entirely obscured by gravitational lensing of E-modes, with only an upper limit on the primordial tensor contribution of $r < 0.07$ (BICEP2 Collaboration et al., 2016). Second, there are very few polarized measurements at large angular scales, $\ell \lesssim 50$ ($\theta \gtrsim 5.2°$). This technically and observationally difficult measurement has considerable discovery space. The poorly constrained large-scale E-modes and unmeasured large-scale B-modes are the most tantalizing data that promise to place meaningful constraints on the reionization and inflation epochs.

1.7 Measuring the Largest Modes with CLASS

The Cosmology Large Angular Scale Surveyor (CLASS) was designed to characterize the polarization of the CMB at the largest angular scales with high enough sensitivity to measure tensor-to-scalar fluctuations at the level of $r = 0.01$ (Essinger-Hileman et al., 2014; Harrington et al., 2016). The CLASS experiment surveys 70% of the microwave sky from the Atacama Desert in Chile. CLASS has two 93 GHz telescopes that target the frequency range where the combination of thermal dust and synchrotron are smallest, a 38 GHz telescope that characterizes the polarized

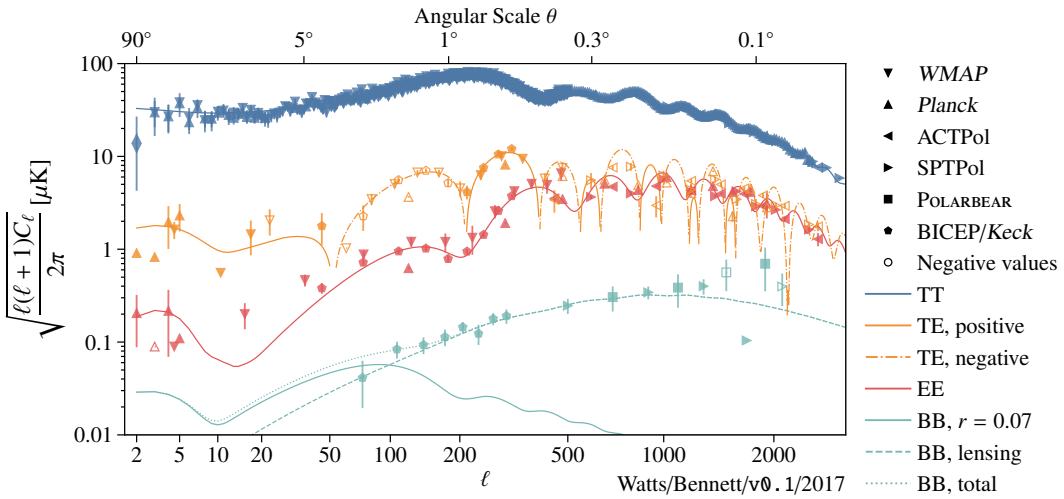

Figure 1.4: This figure shows a summary of all collected CMB anisotropy data at the time of this dissertation's publication. The temperature anisotropy has been measured to the extent that instrumental noise is no longer a factor. The E-mode polarization at smaller than $\sim 5^\circ$ scales has also been measured to this level of precision, as has the cross-correlation between temperature and E-modes. The observed B-mode signal at smaller than degree scales, induced by gravitational lensing of E-modes signal, has also been measured with high statistical significance. Polarization in general is still affected by instrumental noise at large scales; measurements at the reionization peak have been made by the *WMAP* and *Planck* experiments, but the true amplitude of the signal for E-modes is still quite uncertain. Characterization of the largest angular scale polarization is paramount to constraining the amplitude of gravitational waves and the onset of reionization.

synchrotron emission, and a 145/217 GHz dichroic receiver that maps the polarized dust emission. These bandpasses were chosen both to effectively characterize and remove Galactic emission and avoid atmospheric emission lines. The telescopes all have a VPM operating at 10 Hz as their first optical element to put the signal band at 10 Hz, above the $1/f$ noise that comes from instrumental and atmospheric fluctuations (Miller et al., 2016). CLASS's unique combination of large sky coverage, frequency range, front-end modulation, and high sensitivity detectors, make CLASS well poised to characterize the reionization and recombination peaks of the CMB E- and B-mode power spectra.

In this thesis, I present two of my publications that discuss CLASS's observational strategy, its strategy for removing Galactic foreground contamination, and projections for its constraints on the tensor-to-scalar ratio r and the reionization optical depth τ. In chapter 2, we reproduce Watts et al. (2015). We consider the effectiveness of foreground cleaning in the recovery of Cosmic Microwave Background (CMB) polarization sourced by gravitational waves for tensor-to-scalar ratios in the range $0 < r < 0.1$. Using the planned survey area, frequency bands, and sensitivity of CLASS, we simulate maps of Stokes Q and U parameters at 40, 90, 150, and 220 GHz, including realistic models of the CMB, diffuse Galactic thermal dust and synchrotron foregrounds, and Gaussian white noise. We use linear combinations (LCs) of the simulated multifrequency data and a correlation-function pixel-space based likelihood formalism to obtain maximum likelihood estimates of r, the relative scalar amplitude s, and LC coefficients. We find that for 10,000 simulations of a CLASS-like experiment using only measurements of the reionization peak ($\ell \leqslant 23$), there is a 95% C.L. upper limit of $r < 0.017$ in the case of no primordial gravitational

waves. For simulations with $r = 0.01$, we recover at 68% C.L. $r = 0.012^{+0.011}_{-0.006}$. The reionization peak corresponds to a fraction of the multipole moments probed by CLASS, and simulations including $30 \leqslant \ell \leqslant 100$ further improve our upper limits to $r < 0.008$ at 95% C.L. ($r = 0.01^{+0.004}_{-0.004}$ for primordial gravitational waves with $r = 0.01$).

We reproduce Watts et al. (2018) in chapter 3. We analyze simulated maps of CLASS experiment and recover a nearly cosmic-variance limited estimate of the reionization optical depth τ. We use a power spectrum-based likelihood to simultaneously clean foregrounds and estimate cosmological parameters in multipole space. Using software specifically designed to constrain τ, A_s, r, we demonstrate that the CLASS experiment will be able to estimate τ within a factor of two of the full-sky cosmic variance limit allowed by cosmic microwave background polarization measurements. Additionally, we discuss the role of CLASS's τ constraint in conjunction with gravitational lensing of the CMB on obtaining a $\gtrsim 4\sigma$ measurement of the sum of the neutrino masses.

Some useful tangential results are included in Appendix A, including appendices first published in Watts et al. (2015) and Watts et al. (2018), as well as explanations of the real-space spherical harmonic decomposition we implemented for these works and the code used to create a pixel-space covariance matrix from underlying theoretical power spectra.

References

Slipher, V. M. (1917). "Nebulae". In: *Proceedings of the American Philosophical Society* 56, pp. 403–409.

Hubble, E. P. (1926). "Extragalactic nebulae." In: ApJ 64. DOI: 10.1086/143018.

Hubble, E. (1929). "A Relation between Distance and Radial Velocity among Extra-Galactic Nebulae". In: *Proceedings of the National Academy of Science* 15, pp. 168–173. DOI: 10.1073/pnas.15.3.168.

Penzias, A. A. and R. W. Wilson (1965). "A Measurement of Excess Antenna Temperature at 4080 Mc/s." In: ApJ 142, pp. 419–421. DOI: 10.1086/148307.

Dicke, R. H., P. J. E. Peebles, P. G. Roll, and D. T. Wilkinson (1965). "Cosmic Black-Body Radiation." In: ApJ 142, pp. 414–419. DOI: 10.1086/148306.

Mather, J. C., E. S. Cheng, D. A. Cottingham, R. E. Eplee Jr., D. J. Fixsen, T. Hewagama, R. B. Isaacman, K. A. Jensen, S. S. Meyer, P. D. Noerdlinger, S. M. Read, L. P. Rosen, R. A. Shafer, E. L. Wright, C. L. Bennett, N. W. Boggess, M. G. Hauser, T. Kelsall, S. H. Moseley Jr., R. F. Silverberg, G. F. Smoot, R. Weiss, and D. T. Wilkinson (1994). "Measurement of the cosmic microwave background spectrum by the COBE FIRAS instrument". In: ApJ 420, pp. 439–444. DOI: 10.1086/173574.

Planck Collaboration (2015b). "Planck 2015 results. XIII. Cosmological parameters". In: *ArXiv e-prints*. arXiv: 1502.01589.

King, S. and P. Lubin (2016). "Circular polarization of the CMB: Foregrounds and detection prospects". In: Phys. Rev. D 94.2, 023501, p. 023501. DOI: 10.1103/PhysRevD.94.023501. arXiv: 1606.04112.

Montero-Camacho, P. and C. M. Hirata (2018). "Exploring circular polarization in the CMB due to conventional sources of cosmic birefringence". In: *ArXiv e-prints*. arXiv: 1803.04505.

Fixsen, D. J. (2009). "The Temperature of the Cosmic Microwave Background". In: ApJ 707, pp. 916–920. DOI: 10.1088/0004-637X/707/2/916.

Krejny, M., D. T. Chuss, G. Novak, G. M. Voellmer, E. J. Wollack, C. K. Walker, M. Jackson, D. J. Benford, J. G. Staguhn, Jr. Moseley S. H., C. Kulesa, C. Y. Drouet

d'Aubigny, D. R. Golish, and R. F. Loewenstein (2006). "The variable-delay polarization modulator". In: *Society of Photo-Optical Instrumentation Engineers (SPIE) Conference Series*. Vol. 6275, 62751N. DOI: 10.1117/12.671927.

Chuss, D. T., E. J. Wollack, R. Henry, H. Hui, A. J. Juarez, M. Krejny, S. H. Moseley, and G. Novak (2012). "Properties of a variable-delay polarization modulator". In: Appl. Opt. 51, p. 197. DOI: 10.1364/AO.51.000197. arXiv: 1106.5984 [astro-ph.IM].

Flauger, R. M. (2009). "Constraining fundamental physics with cosmology". PhD thesis. The University of Texas at Austin.

Lewis, A., A. Challinor, and A. Lasenby (2000). "Efficient Computation of Cosmic Microwave Background Anisotropies in Closed Friedmann-Robertson-Walker Models". In: ApJ 538, pp. 473–476. DOI: 10.1086/309179. eprint: astro-ph/9911177.

Blas, D., J. Lesgourgues, and T. Tram (2011). "The Cosmic Linear Anisotropy Solving System (CLASS). Part II: Approximation schemes". In: J. Cosmology Astropart. Phys. 7, 034, p. 034. DOI: 10.1088/1475-7516/2011/07/034. arXiv: 1104.2933.

BICEP2/Keck Collaboration, Planck Collaboration, P. A. R. Ade, N. Aghanim, Z. Ahmed, R. W. Aikin, K. D. Alexander, M. Arnaud, J. Aumont, C. Baccigalupi, and et al. (2015). "Joint Analysis of BICEP2/Keck Array and Planck Data". In: *Physical Review Letters* 114.10, 101301, p. 101301. DOI: 10.1103/PhysRevLett.114.101301. arXiv: 1502.00612.

Planck Collaboration (2015a). "Planck 2015 results. X. Diffuse component separation: Foreground maps". In: *ArXiv e-prints*. arXiv: 1502.01588.

Rybicki, George B. and Alan P. Lightman (1979). *Radiative processes in astrophysics*.

Pacholczyk, A. G. (1970). *Radio astrophysics. Nonthermal processes in galactic and extragalactic sources*.

Strong, A. W., E. Orlando, and T. R. Jaffe (2011). "The interstellar cosmic-ray electron spectrum from synchrotron radiation and direct measurements". In: A&A 534, A54, A54. DOI: 10.1051/0004-6361/201116828.

Orlando, Elena and Andrew Strong (2013). "Galactic synchrotron emission with cosmic ray propagation models". In: MNRAS 436, pp. 2127–2142. DOI: 10.1093/mnras/stt1718.

Fuskeland, U., I. K. Wehus, H. K. Eriksen, and S. K. Næss (2014). "Spatial Variations in the Spectral Index of Polarized Synchrotron Emission in the 9 yr WMAP Sky Maps". In: ApJ 790, 104, p. 104. DOI: 10.1088/0004-637X/790/2/104. arXiv: 1404.5323.

Thorne, B., J. Dunkley, D. Alonso, and S. Næss (2017). "The Python Sky Model: software for simulating the Galactic microwave sky". In: MNRAS 469, pp. 2821–2833. DOI: 10.1093/mnras/stx949. arXiv: 1608.02841.

Planck Collaboration et al. (2015a). "Planck intermediate results. XIX. An overview of the polarized thermal emission from Galactic dust". In: A&A 576, A104, A104. DOI: 10.1051/0004-6361/201424082. arXiv: 1405.0871.

Planck Collaboration et al. (2015b). "Planck intermediate results. XX. Comparison of polarized thermal emission from Galactic dust with simulations of MHD turbulence". In: A&A 576, A105, A105. DOI: 10.1051/0004-6361/201424086. arXiv: 1405.0872.

Planck Collaboration et al. (2018). "Planck intermediate results. LIV. Polarized dust foregrounds". In: *ArXiv e-prints*. arXiv: 1801.04945.

Erickson, William C. (1957). "A Mechanism of Non-Thermal Radio-Noise Origin." In: ApJ 126, p. 480. DOI: 10.1086/146421.

Draine, B. T. and A. Lazarian (1998). "Diffuse Galactic Emission from Spinning Dust Grains". In: ApJ 494, pp. L19–L22. DOI: 10.1086/311167.

Hoang, T. (2015). "Anomalous Microwave Emission from Spinning Dust and its Polarization Spectrum". In: *ArXiv e-prints*. arXiv: 1511.05997.

Macellari, N., E. Pierpaoli, C. Dickinson, and J. E. Vaillancourt (2011). "Galactic foreground contributions to the 5-year Wilkinson Microwave Anisotropy Probe maps". In: MNRAS 418, pp. 888–905. DOI: 10.1111/j.1365-2966.2011.19542.x.

Chluba, J. and R. A. Sunyaev (2012). "The evolution of CMB spectral distortions in the early Universe". In: MNRAS 419, pp. 1294–1314. DOI: 10.1111/j.1365-2966.2011.19786.x. arXiv: 1109.6552.

Bennett, C. L., D. Larson, J. L. Weiland, N. Jarosik, G. Hinshaw, N. Odegard, K. M. Smith, R. S. Hill, B. Gold, M. Halpern, E. Komatsu, M. R. Nolta, L. Page, D. N. Spergel, E. Wollack, J. Dunkley, A. Kogut, M. Limon, S. S. Meyer, G. S. Tucker, and E. L. Wright (2013). "Nine-year Wilkinson Microwave Anisotropy Probe (WMAP) Observations: Final Maps and Results". In: ApJS 208, 20, p. 20. DOI: 10.1088/0067-0049/208/2/20. arXiv: 1212.5225.

Planck Collaboration et al. (2016). "Planck 2015 results. I. Overview of products and scientific results". In: A&A 594, A1, A1. DOI: 10.1051/0004-6361/201527101.

Louis, T., E. Grace, M. Hasselfield, M. Lungu, L. Maurin, G. E. Addison, P. A. R. Ade, S. Aiola, R. Allison, M. Amiri, E. Angile, N. Battaglia, J. A. Beall, F. de Bernardis, J. R. Bond, J. Britton, E. Calabrese, H.-m. Cho, S. K. Choi, K. Coughlin, D. Crichton, K. Crowley, R. Datta, M. J. Devlin, S. R. Dicker, J.

Dunkley, R. Dünner, S. Ferraro, A. E. Fox, P. Gallardo, M. Gralla, M. Halpern, S. Henderson, J. C. Hill, G. C. Hilton, M. Hilton, A. D. Hincks, R. Hlozek, S. P. P. Ho, Z. Huang, J. Hubmayr, K. M. Huffenberger, J. P. Hughes, L. Infante, K. Irwin, S. Muya Kasanda, J. Klein, B. Koopman, A. Kosowsky, D. Li, M. Madhavacheril, T. A. Marriage, J. McMahon, F. Menanteau, K. Moodley, C. Munson, S. Naess, F. Nati, L. Newburgh, J. Nibarger, M. D. Niemack, M. R. Nolta, C. Nuñez, L. A. Page, C. Pappas, B. Partridge, F. Rojas, E. Schaan, B. L. Schmitt, N. Sehgal, B. D. Sherwin, J. Sievers, S. Simon, D. N. Spergel, S. T. Staggs, E. R. Switzer, R. Thornton, H. Trac, J. Treu, C. Tucker, A. Van Engelen, J. T. Ward, and E. J. Wollack (2017). "The Atacama Cosmology Telescope: two-season ACTPol spectra and parameters". In: J. Cosmology Astropart. Phys. 6, 031, p. 031. DOI: 10.1088/1475-7516/2017/06/031. arXiv: 1610.02360.

George, E. M., C. L. Reichardt, K. A. Aird, B. A. Benson, L. E. Bleem, J. E. Carlstrom, C. L. Chang, H.-M. Cho, T. M. Crawford, A. T. Crites, T. de Haan, M. A. Dobbs, J. Dudley, N. W. Halverson, N. L. Harrington, G. P. Holder, W. L. Holzapfel, Z. Hou, J. D. Hrubes, R. Keisler, L. Knox, A. T. Lee, E. M. Leitch, M. Lueker, D. Luong-Van, J. J. McMahon, J. Mehl, S. S. Meyer, M. Millea, L. M. Mocanu, J. J. Mohr, T. E. Montroy, S. Padin, T. Plagge, C. Pryke, J. E. Ruhl, K. K. Schaffer, L. Shaw, E. Shirokoff, H. G. Spieler, Z. Staniszewski, A. A. Stark, K. T. Story, A. van Engelen, K. Vanderlinde, J. D. Vieira, R. Williamson, and O. Zahn (2015). "A Measurement of Secondary Cosmic Microwave Background Anisotropies from the 2500 Square-degree SPT-SZ Survey". In: ApJ 799, 177, p. 177. DOI: 10.1088/0004-637X/799/2/177. arXiv: 1408.3161.

BICEP2 Collaboration, Keck Array Collaboration, P. A. R. Ade, Z. Ahmed, R. W. Aikin, K. D. Alexander, D. Barkats, S. J. Benton, C. A. Bischoff, J. J. Bock, R. Bowens-Rubin, J. A. Brevik, I. Buder, E. Bullock, V. Buza, J. Connors, B. P. Crill, L. Duband, C. Dvorkin, J. P. Filippini, S. Fliescher, J. Grayson, M. Halpern, S. Harrison, G. C. Hilton, H. Hui, K. D. Irwin, K. S. Karkare, E. Karpel, J. P. Kaufman, B. G. Keating, S. Kefeli, S. A. Kernasovskiy, J. M. Kovac, C. L. Kuo, E. M. Leitch, M. Lueker, K. G. Megerian, C. B. Netterfield, H. T. Nguyen, R. O'Brient, R. W. Ogburn, A. Orlando, C. Pryke, S. Richter, R. Schwarz, C. D. Sheehy, Z. K. Staniszewski, B. Steinbach, R. V. Sudiwala, G. P. Teply, K. L. Thompson, J. E. Tolan, C. Tucker, A. D. Turner, A. G. Vieregg, A. C. Weber, D. V. Wiebe, J. Willmert, C. L. Wong, W. L. K. Wu, and K. W. Yoon (2016). "Improved Constraints on Cosmology and Foregrounds from BICEP2 and Keck Array Cosmic Microwave Background Data with Inclusion of 95 GHz Band". In: *Physical Review Letters* 116.3, 031302, p. 031302. DOI: 10.1103/PhysRevLett.116.031302. arXiv: 1510.09217.

Essinger-Hileman, Thomas, Aamir Ali, Mandana Amiri, John W. Appel, Derek Araujo, Charles L. Bennett, Fletcher Boone, Manwei Chan, Hsiao-Mei Cho, David T. Chuss, Felipe Colazo, Erik Crowe, Kevin Denis, Rolando Dünner, Joseph Eimer, Dominik Gothe, Mark Halpern, Kathleen Harrington, Gene C. Hilton, Gary F. Hinshaw, Caroline Huang, Kent Irwin, Glenn Jones, John Karakla, Alan J. Kogut, David Larson, Michele Limon, Lindsay Lowry, Tobias Marriage, Nicholas Mehrle, Amber D. Miller, Nathan Miller, Samuel H. Moseley, Giles Novak, Carl Reintsema, Karwan Rostem, Thomas Stevenson, Deborah Towner, Kongpop U-Yen, Emily Wagner, Duncan Watts, Edward J. Wollack, Zhilei Xu, and Lingzhen Zeng (2014). "CLASS: the cosmology large angular scale surveyor". In: *Millimeter, Submillimeter, and Far-Infrared Detectors and Instrumentation for Astronomy VII*. Vol. 9153, p. 91531I. DOI: 10.1117/12.2056701.

Harrington, Kathleen, Tobias Marriage, Aamir Ali, John W. Appel, Charles L. Bennett, Fletcher Boone, Michael Brewer, Manwei Chan, David T. Chuss, Felipe Colazo, Sumit Dahal, Kevin Denis, Rolando Dünner, Joseph Eimer, Thomas Essinger- Hileman, Pedro Fluxa, Mark Halpern, Gene Hilton, Gary F. Hinshaw, Johannes Hubmayr, Jeffrey Iuliano, John Karakla, Jeff McMahon, Nathan T. Miller, Samuel H. Moseley, Gonzalo Palma, Lucas Parker, Matthew Petroff, Bastián. Pradenas, Karwan Rostem, Marco Sagliocca, Deniz Valle, Duncan Watts, Edward Wollack, Zhilei Xu, and Lingzhen Zeng (2016). "The Cosmology Large Angular Scale Surveyor". In: *Millimeter, Submillimeter, and Far-Infrared Detectors and Instrumentation for Astronomy VIII*. Vol. 9914, 99141K. DOI: 10.1117/12.2233125.

Miller, N. J., D. T. Chuss, T. A. Marriage, E. J. Wollack, J. W. Appel, C. L. Bennett, J. Eimer, T. Essinger-Hileman, D. J. Fixsen, K. Harrington, S. H. Moseley, K. Rostem, E. R. Switzer, and D. J. Watts (2016). "Recovery of Large Angular Scale CMB Polarization for Instruments Employing Variable-delay Polarization Modulators". In: ApJ 818, 151, p. 151. DOI: 10.3847/0004-637X/818/2/151.

Watts, D. J., D. Larson, T. A. Marriage, M. H. Abitbol, J. W. Appel, C. L. Bennett, D. T. Chuss, J. R. Eimer, T. Essinger-Hileman, N. J. Miller, K. Rostem, and E. J. Wollack (2015). "Measuring the Largest Angular Scale CMB B-mode Polarization with Galactic Foregrounds on a Cut Sky". In: ApJ 814, 103, p. 103. DOI: 10.1088/0004-637X/814/2/103. arXiv: 1508.00017.

Watts, D. J., B. Wang, A. Ali, J. W. Appel, C. L. Bennett, D. T. Chuss, S. Dahal, J. R. Eimer, T. Essinger-Hileman, K. Harrington, G. Hinshaw, J. Iuliano, T. A. Marriage, N. J. Miller, I. L. Padilla, M. Petroff, K. Rostem, E. J. Wollack, and Z. Xu (2018). "A Projected Estimate of the Reionization Optical Depth Using

the CLASS Experiment's Sample-Variance Limited E-Mode Measurement". In: *ArXiv e-prints*. arXiv: 1801.01481.

Chapter 2

Measuring the Largest Angular Scale CMB B-mode Polarization with Galactic Foregrounds on a Cut Sky

2.1 Introduction

All astronomical data on cosmological scales conform to a six-parameter model of the Universe (ΛCDM) with dark matter and a cosmological constant as the dominant components (Hinshaw et al., 2013; Planck Collaboration, 2015c). The inflationary paradigm, which postulates a short period of exponential expansion in the early Universe, accounts for features in ΛCDM, including the high degree of homogeneity and flatness and the scalar spectral index $n_s \lesssim 1$ (e.g. Guth, 1981; Starobinsky, 1980; Kazanas, 1980; Mukhanov and Chibisov, 1981; Einhorn and Sato, 1981; Linde, 1982; Albrecht and Steinhardt, 1982; Hinshaw et al., 2013; Bennett et al., 2013). One of inflation's predictions is a super-horizon stochastic gravitational wave background that induces polarization in the CMB (Polnarev, 1985). We can decompose

the CMB's polarization field into E-modes with $(-1)^{\ell}$ parity, and B-modes with $(-1)^{\ell+1}$ parity (Seljak and Zaldarriaga, 1997; Kamionkowski, Kosowsky, and Stebbins, 1997; Hu and White, 1997). An inflationary B-mode signal can only come from primordial gravitational waves (tensor fluctuations of the metric), so a measurement of such a signal would be strong evidence for an inflationary epoch. We quantify constraints on B-modes in terms of the ratio of tensor fluctuations to scalar (density) fluctuations, r, evaluated at $k = 0.05\,\mathrm{Mpc}^{-1}$. The current upper limit on tensor fluctuations ($r < 0.09$) using polarization only comes from a combination of *Planck* and BICEP2 measurements (BICEP2/Keck Collaboration et al., 2015; Planck Collaboration, 2015e).

The Cosmology Large Angular Scale Surveyor (CLASS) is a ground-based experiment that will observe 70% of the sky from Cerro Toco in the Atacama Desert at frequencies of 40, 90, 150, and 220 GHz (Eimer et al., 2012; Essinger-Hileman et al., 2014; Rostem et al., 2014; Appel et al., 2014). CLASS's 90 GHz band has a projected sensitivity of 10 μK arcmin, an improvement over the *Planck* 100 GHz map (118 μK arcmin at high-ℓ, Planck Collaboration, 2015a), and will achieve the measurement stability required to reach low multipoles using front end modulation by a variable-delay polarization modulator (VPM) (Chuss et al., 2012). CLASS is currently the only planned sub-orbital mission exploring the combination of frequency and multipole ranges described above. CLASS will probe the reionization peak in the BB power spectrum ($\theta \gtrsim 2^{\circ}$) along with other missions including PIPER (Lazear et al., 2014), QUIJOTE (López-Caniego et al., 2014), LSPE (Aiola et al., 2012), and GroundBird (Tajima et al., 2012). CLASS will also probe the recombination peak explored by BICEP2 (Ogburn et al., 2010), SPTpol (Austermann et al., 2012),

ABS (Essinger-Hileman et al., 2010), ACTPol (Niemack et al., 2010), POLARBEAR (Kermish et al., 2012), EBEX (Oxley et al., 2004), and SPIDER (Filippini et al., 2010). In contrast with other surveys that focus on higher multipoles or have different frequency ranges, CLASS probes a unique combination of frequency and multipole space, as illustrated in Figure 2.1. In addition to constraining inflation at all of the angular scales where B-modes are predominantly inflationary, we show that a noise-dominated BB spectrum $C_\ell \propto \ell^{-2}$ has signal-to-noise that scales as $\ell^{-3/2}$, as opposed to the well-known result $\ell^{1/2}$ found in the cosmic variance limit. In this era of initial measurements of B-mode polarization, we gain more information from large angular scale measurements than conventional wisdom would suggest, as we show in §A.1.

In this paper we explore the recovery of B-modes in the presence of foregrounds, instrument noise, and a cut sky. This analysis will focus on a subset of the simulated CLASS data using only the multipoles $\ell \leqslant 23$, to distill the information available from measurements of the reionization peak alone. In §2.2 we describe simulations of the CMB with $0 < r < 0.1$ and foreground components in 40, 90, 150, and 220 GHz frequency bands using the CLASS sensitivity and sky coverage. In §2.3 we describe the maximum likelihood method for recovering the primordial B-mode signal in the presence of foregrounds. We forecast constraints on r from this method applied to the simulations in §2.4.

2.2 Multifrequency Simulations

We use publicly available data to simulate the polarized Galactic synchrotron and dust foregrounds. Our synchrotron map templates are based on the *WMAP*9 *K*-band (23 GHz) polarization data (Bennett et al., 2013). Synchrotron polarization

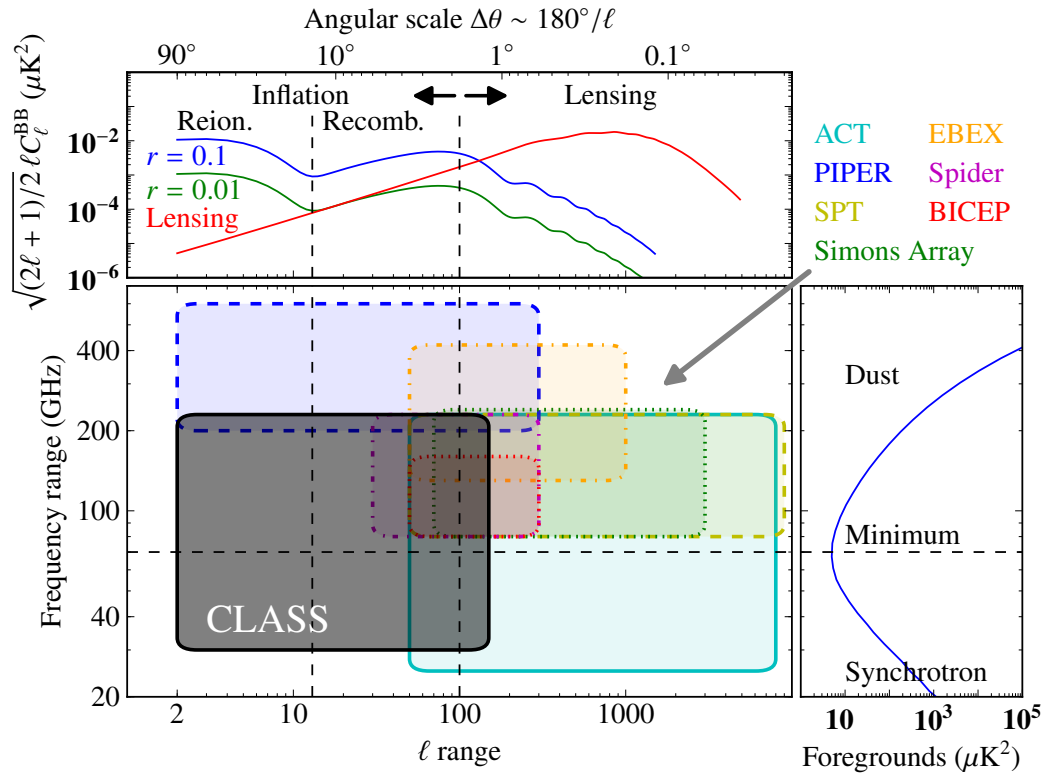

Figure 2.1: We display schematically the regions of purview corresponding to balloon-borne and ground-based CMB polarization experiments. CLASS is unique in measuring both the reionization and recombination peaks while straddling the foreground minimum. As upper limits on r decrease, inflationary B-modes will dominate over lensing at increasing larger scales. The foreground model shown comes from Planck Collaboration (2015b) using measurements of 73% of the sky. We plot the frequency dependence of foregrounds in thermodynamic temperature units.

Table 2.1: Noise Contribution from Rescaled Foreground Templates

Frequency ν (GHz)	$w_\nu^{-1/2}$ (μK arcmin)	$\alpha_S^{\nu\,\dagger}$	$\alpha_S^\nu w_{40}^{-1/2}$ (μK arcmin)	$\alpha_D^{\nu\,\dagger}$	$\alpha_D^\nu w_{220}^{-1/2}$ (μK arcmin)
40	39	1	39	0.022	0.95
90	10	0.103	4.02	0.095	4.09
150	15	0.032	1.25	0.306	13.2
220	43	0.018	0.70	1	43

Note – For each band we list the expected 5-year polarized noise at each frequency ($w_\nu^{-1/2}$). The columns for $\alpha_i^\nu w_{\nu_i}^{-1/2}$ show the expected noise contribution in each band when we rescale the 40 and 220 GHz channels according to the synchrotron and dust template scalings used in simulations (Equation 2.2). The values of $w_\nu^{-1/2}$ are estimated in Essinger-Hileman et al., 2014.

† Values for the amplitude of synchrotron and dust templates at frequency ν, α_i^ν, come from Equation 2.2 and assume $\beta_S = -3$ and $\beta_D = 1.6$.

dominates the data in this band with negligible contribution from CMB polarization. Our dust polarization templates are based on the *Planck* 353 GHz maps (Planck Collaboration, 2015a). In units of antenna temperature $T_A(\nu) \equiv c^2 I_\nu / 2k_B\nu^2$, with I_ν the specific intensity, we approximate the modified blackbody emission of dust as a power law with index $\beta_D = 1.6$ (Planck Collaboration, 2015f) and the synchrotron emission as a power law with $\beta_S = -3.0$ (Bennett et al., 2013; Fuskeland et al., 2014). Using these power law indices we rescale the *WMAP* and *Planck* data to create templates for synchrotron and dust at 40 and 220 GHz, respectively. The minimum contamination from foregrounds is around 70 GHz (Bennett et al., 2013; Planck Collaboration, 2015b), which, along with the location of atmospheric water and oxygen lines, informs the CLASS experiment's choice of band center frequencies (Eimer et al., 2012).

We estimate CLASS's sensitivity to tensor modes using random realizations of

Gaussian CMB fluctuations with white Gaussian detector noise, all with the same model of foreground contamination. We use the fiducial ΛCDM parameters from *WMAP*9 (Hinshaw et al., 2013) to simulate the scalar perturbation field, with a tensor contribution added in via $C_\ell = rC_\ell^{\rm tensor} + sC_\ell^{\rm scalar}$. The contribution from gravitational lensing is included in the $C_\ell^{\rm scalar}$ term. We generate the theoretical spectra C_ℓ using CAMB,[1] smoothed in multipole space using a Gaussian window function with $\theta_{\rm FWHM} = 15^\circ$ to reduce aliasing from pixelization. We derive random Q and U maps from the theoretical C_ℓ values using the Healpix package `synfast` (Górski et al., 2005) with pixels at resolution $\theta_{\rm pix} \sim 7^\circ$ ($N_{\rm side} = 8$),[2] including multipoles $2 \leqslant \ell \leqslant 23$. We then add dust and synchrotron polarization to each band, along with white Gaussian noise corresponding to the experiment sensitivity, given here in units of μK arcmin (see Table 2.1).

Given CLASS's wide scan strategy from its site in the Atacama Desert at latitude -23° (Essinger-Hileman et al., 2014), we include data with declination $-73^\circ < \delta < 27^\circ$ so that $f_{\rm sky} \simeq 0.7$. We mask out the Galactic equator based on the *WMAP* P06 mask, defined in Page et al., 2007, resulting in a final $f_{\rm sky} \simeq 0.5$.

We define the polarization maps $\boldsymbol{P}$ as a vector with the Q and U Stokes parameters as components. We use $\boldsymbol{P}^{\rm S}$ and $\boldsymbol{P}^{\rm D}$ as the synchrotron and dust templates at 40 GHz and 220 GHz respectively, and $\boldsymbol{P}^{\rm CMB}$ the simulated CMB. This allows us to generate the simulated multifrequency CLASS polarization data,

$$\boldsymbol{P}^\nu = \alpha_{\rm S}^\nu \boldsymbol{P}^{\rm S} + \alpha_{\rm D}^\nu \boldsymbol{P}^{\rm D} + \boldsymbol{P}^{\rm CMB} + \boldsymbol{N}^\nu \tag{2.1}$$

[1] http://camb.info

[2] Healpix maps have resolutions denoted $r = 0, 1, 2, \ldots$. Each of the 12 lowest resolution pixels that characterize $N_{\rm side} = 1$ divides into $N_{\rm side} \times N_{\rm side}$ regions where $N_{\rm side} \equiv 2^r$, and the total number of pixels is $N_{\rm pix} = 12N_{\rm side}^2$ with characteristic pixel size $\theta_{\rm pix} \sim 58.6^\circ/N_{\rm side}$. The full documentation is at http://healpix.sf.net.

where $\boldsymbol{N}^{\nu}$ contains the Gaussian white noise maps for Q and U, with the amplitude of the noise determined by the survey sensitivity given in Table 2.1 (Essinger-Hileman et al., 2014). Because we define the power law spectral indices β_i in terms of antenna temperature and our data are in units of thermodynamic temperature, we scale the foreground channels using the factor

$$\alpha_i^{\nu}(\hat{\boldsymbol{n}}) \equiv \left(\frac{\nu}{\nu_i}\right)^{\beta_i(\hat{\boldsymbol{n}})} \frac{g(\nu)}{g(\nu_i)} \tag{2.2}$$

with $g(\nu) \equiv \partial T/\partial T_A = (e^x - 1)^2/(x^2 e^x)$ the conversion factor from thermodynamic to antenna temperatures with $x \equiv h\nu/kT_{\rm CMB} = \nu/56.78\,{\rm GHz}$. These α_i^{ν} give the relative strength of each foreground component i normalized by its strength at template frequencies ν_i. As described above these templates are based on the *WMAP* K-band for synchrotron and *Planck* 353 GHz band for dust scaled to $\nu_{\rm S} = 40\,{\rm GHz}$ and $\nu_{\rm D} = 220\,{\rm GHz}$, respectively. For these chosen frequencies and spectral indices, these strengths are $\alpha_{\rm S}^{90} = 0.103$ and $\alpha_{\rm D}^{90} = 0.095$ at 90 GHz while for 150 GHz, we have $\alpha_{\rm S}^{150} = 0.032$ and $\alpha_{\rm D}^{150} = 0.305$, as shown in Table 2.1. We display sample maps of our simulated CLASS data in Figure 2.2, along with the best-fit cleaned data and the residuals, to be described in §2.3.

The spatial dependence of the spectral indices is based on the pre-flight *Planck* Sky Model (PSM) (Delabrouille et al., 2013), which we display in Figure 2.3. As we demonstrate below, the PSM is consistent with current data. The β_i from this model come from intensity measurements of foreground components, and are not expected to be the same as the polarized power law indices. For this work, we rescale the PSM spectral indices to have mean values $\langle\beta_{\rm S}\rangle = -3.0$ and $\langle\beta_{\rm D}\rangle = 1.6$. The amplitude of synchrotron spectral index fluctuations in the *WMAP* estimate derived from the K

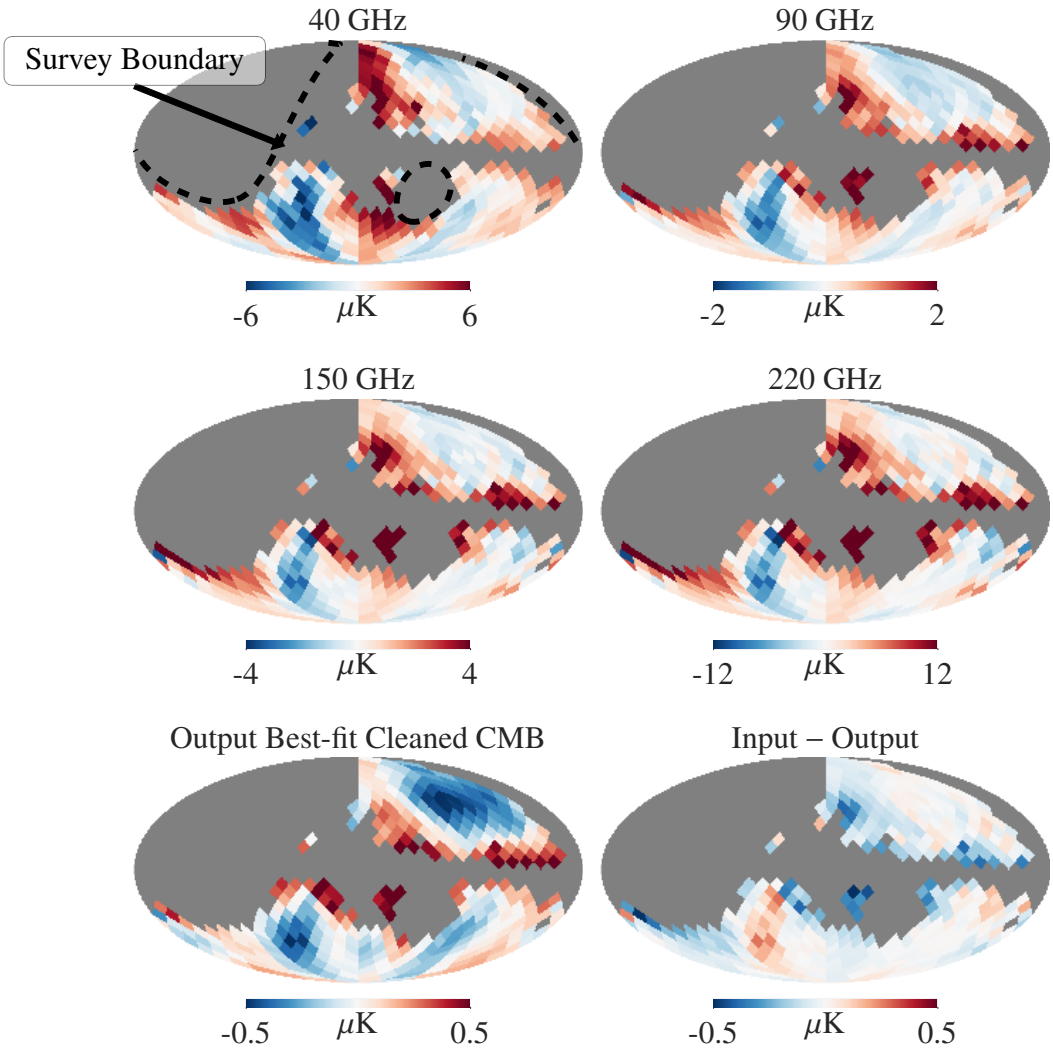

Figure 2.2: The top four plots show simulated CLASS observations of Q polarization assuming spatially varying spectral indices (as defined in Equation 2.2). The bottom two plots show (left) the output maximum likelihood CMB map with the simulation's best-fit LC parameters as described in §2.3 and (right) the difference between the input CMB and the output maximum likelihood estimate. The difference map shows the effectiveness of our method for reconstructing the CMB, and the temperature range is representative of the noise in our map. Note that each of these maps uses a different color scale. We present the maps in Galactic coordinates (Mollweide projection) with gray pixels representing regions of the sky outside of the CLASS survey boundary or inside the Galactic mask. The black dashed lines on the 40 GHz map denote the declination limits of $-73°$ and $27°$ in celestial coordinates.

and *Ka* band data (Bennett et al., 2013; Fuskeland et al., 2014) is broadly consistent with the variation in the PSM's β_S Miville-Deschênes et al., 2008, model 4. The variation in the dust spectral index has variation $\Delta\beta_D$ (Planck Collaboration, 2015f) that is consistent with a constant spectral index (see §A.2) and hence with the small variation in the PSM (Finkbeiner, Davis, and Schlegel, 1999, model 8). Note that we only use the pre-flight PSM for spectral variation, while we derive the 40 and 220 GHz polarization templates from *WMAP* and *Planck* data respectively, as described above. However, the CLASS dataset itself will improve on this and be used in our final analysis.

In this study we focus on the effects of foregrounds and a cut sky on the recoverability of primordial B-modes. To isolate these effects we do not include potential instrumental systematics. For measurements that use a VPM to suppress $1/f$ noise, Miller et al. (2015) find that B-mode power from systematic effects can be suppressed to levels below the primordial level for $r = 0.01$, which suggests such effects are negligible in the context of this work.

2.3 Pixelized Likelihood Analysis

We base our analysis on methods developed in Efstathiou, 2006 and Katayama and Komatsu, 2011, and extend the Gaussian likelihood formalism to an arbitrary number of frequency channels, each with its own linear fit coefficient. We define the likelihood

$$\mathcal{L} \propto \frac{\exp[-\frac{1}{2}\boldsymbol{x}(a_\nu)^T \boldsymbol{C}_p^{-1}(r, s, a_\nu)\boldsymbol{x}(a_\nu)]}{\sqrt{\det[\boldsymbol{C}_p(r, s, a_\nu)]}}, \tag{2.3}$$

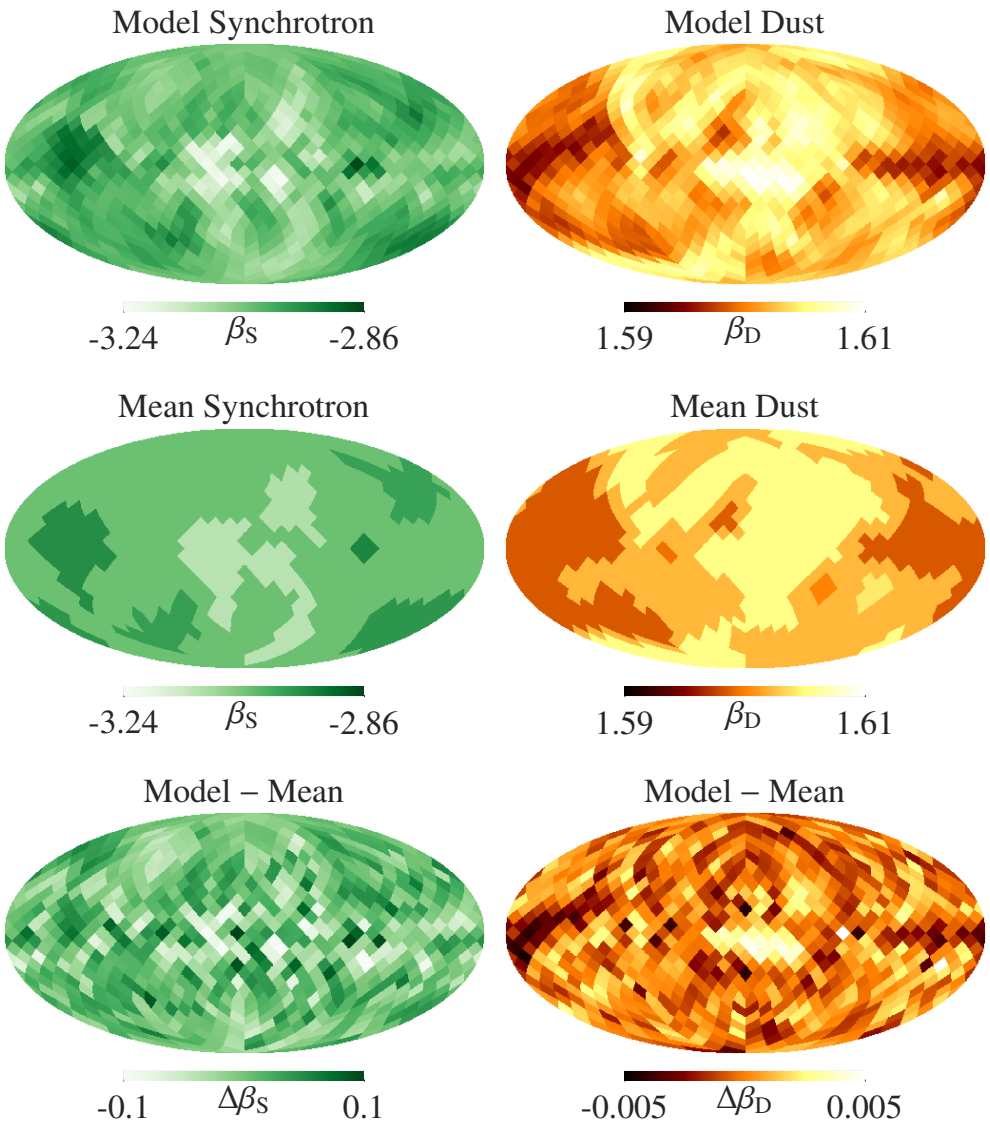

Figure 2.3: The top row of foreground spectral indices from the PSM (Delabrouille et al., 2013) are used in our simulations. We model the variation in spectral index by breaking the sky into 14 regions (middle row, labelled "Mean") with distinct LC fit coefficients. The β_i in the middle row are the means of the PSM spectral indices within each region. This modelling trades off accuracy at small scales for computational efficiency.

where

$$\boldsymbol{x} = \sum_{\nu}^{n} a_\nu \boldsymbol{P}^\nu, \quad \sum_{\nu}^{n} a_\nu = 1 \tag{2.4}$$

is the CMB map cleaned using n frequency channels, with $\sum_\nu a_\nu = 1$ preserving the CMB's frequency spectrum. We achieve this constraint defining a_{90} as $1 - a_{40} - a_{150} - a_{220}$. We define the pixel-space covariance matrix,

$$\boldsymbol{C}_p = r\boldsymbol{C}_p^{\text{tensor}} + s\boldsymbol{C}_p^{\text{scalar}} + \boldsymbol{I}_p\sigma^2. \tag{2.5}$$

Here $\boldsymbol{I}_p$ is the identity matrix in pixel space, and $\sigma^2 = \sum_\nu (a_\nu\sigma_\nu)^2$ is the survey noise. The $\boldsymbol{C}_p$'s are the theoretical signal covariance matrices, which themselves come from the power spectra, C_ℓ^{BB} and C_ℓ^{EE}, assuming uncorrelated E- and B-modes, as detailed in Appendix A of Katayama and Komatsu, 2011. We vary s, the amplitude of scalar fluctuations normalized by a fiducial value, to mitigate spurious correlations between the CMB and foregrounds in the maximum likelihood fitting as in §5.1 of Katayama and Komatsu, 2011. We use uniform unbounded priors on all parameters except for the tensor-to-scalar ratio and the 40 GHz and 220 GHz coefficients. We impose the prior $r \geqslant 0$ to avoid singular covariance matrices in Equation 2.5, and we impose the prior that the 40 and 220 GHz coefficients are negative to avoid numerical errors (which does not affect our overall results, as seen in Figure 2.4). The product of our likelihood and priors is proportional to the Bayesian posterior probability distribution for our parameters. We emphasize that this method differs from the internal linear combination method described in Efstathiou, Gratton, and Paci, 2009 due to our simultaneous variation of cosmological and foreground LC parameters and also due to the presence of the $\boldsymbol{C}_p^{-1}$ weighting for the solution of LC coefficients. When we maximize the likelihood (Equation 2.3) using the covariance

matrix (Equation 2.5), the maximum likelihood LC coefficients, $\{a_\nu\}$, we create a map, $\boldsymbol{x}$, that best approximates a realization of the CMB with Gaussian noise. The modified foreground removal method is effective because the pixel-pixel correlations, $\boldsymbol{C}_p$, drive the fit so that the mean of the map, $\langle \boldsymbol{x} \rangle$, is zero, with variance corresponding to CMB fluctuations and instrumental white noise.

We obtain an estimate of the CMB, $\boldsymbol{x}$, by finding the parameters r, s, a_{40}, a_{90}, a_{150}, and a_{220} that maximize the likelihood $\mathcal{L}$ with the priors $r \geqslant 0$ and $a_{40}, a_{220} \leqslant 0$. We find that although a Monte Carlo Markov Chain (MCMC) estimation gives posterior distributions and suitable estimators for these parameters, using the `scipy` minimization routine `fmin_l_bfgs_b`, an implementation of the limited-memory Broyden-Fletcher-Goldfarb-Shanno (BFGS) algorithm (Byrd et al., 1995), gives estimates of the maximum likelihood values for parameters $\{r_{\rm ML}, s_{\rm ML}, a_{\nu,{\rm ML}}\}$ at a fraction of the time required to compute the full MCMC posterior distributions. We plan to use MCMC methods for the analysis of the actual multi-frequency CLASS observed maps, but cosmic variance can cause different posterior distributions for the same underlying value of r. For our $\sim 10^4$ simulations with random realizations of CMB and noise, the distribution of maximum likelihood values for r is comparable to the width of the posterior distribution of a single Monte Carlo chain. For forecasting purposes, we therefore run large numbers of simulations and study the posterior distribution of maximum likelihood values of the model parameters.

We also model spatially varying spectral behavior in the foregrounds. In practice, we split the map into fourteen separate foreground regions defined by the intersection of unmasked dust and synchrotron regions shown in Figure 2.3, which results in a 44-parameter fit (four a_ν coefficients with one constraint $\times$ 14 regions, s, and r) for

varying spectral behavior. We define the regions in the middle row of Figure 2.3 using the PSM components in the top row. To construct these regions, we smooth the PSM β_i maps, find all local minima and maxima, and choose contiguous pixels with roughly constant spectral index values. We choose thresholds such that the regions are small enough to make a constant index a good approximation, and large enough that we maintain computational efficiency that follows from the smaller number of parameters. Defining these regions according to existing measurements of spectral variation is the only part of our analysis that requires data external to CLASS. When the CLASS data are available, they will be the best probe of this large-scale position dependence of the foreground spectral indices.

We discuss the distribution of maximum likelihood r values in the following section. For typical simulations with input $r = 0.01$, the other parameters for a single representative region have sample mean and standard deviation $s = 0.97 \pm 0.13$, $a_{40} = -0.1 \pm 0.01$, $a_{90} = 0.9 \pm 0.1$, $a_{150} = 0.3 \pm 0.1$, and $a_{220} = -0.16 \pm 0.03$. Both a_{40} and a_{220} are negative because data at these frequencies serve to remove foregrounds, while the 90 and 150 GHz coefficients contribute positively, with most of the weight coming from a_{90}. We display the distribution of ML values for these parameters and r in Figure 2.4.

2.4 Recovery of r

If the uncertainty were only dependent on instrument noise and not a function of the cosmological value of r, we would choose a threshold based on this uncertainty, such as $3\sigma_r$, and claim this as a detection limit. However, the prediction problem is more complicated, as σ_r depends on r as well as dust and synchrotron emission in the

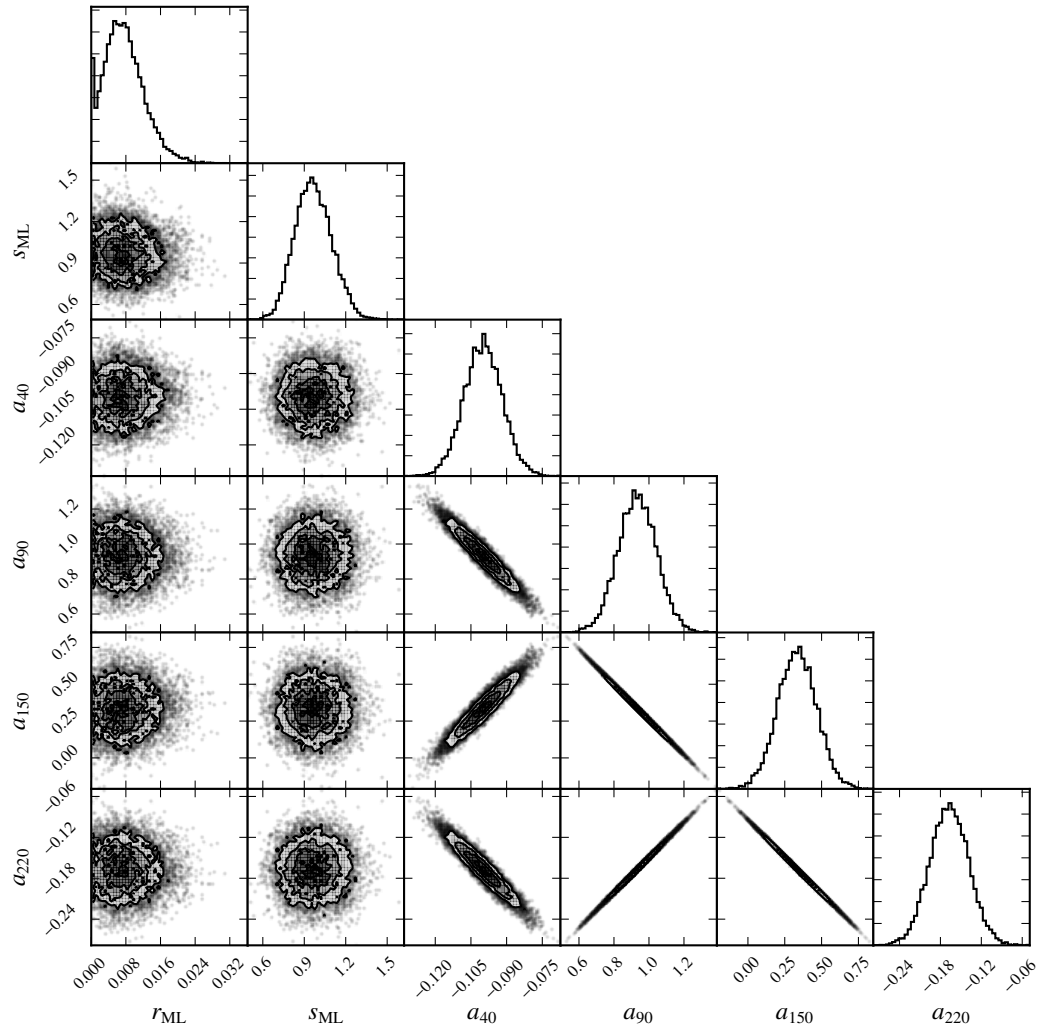

Figure 2.4: Distribution of the output maximum likelihood parameters for 10^4 simulations using the sensitivities from Table 2.1 with an input $r = 0.01$. The simulation features spatially varying spectral indices and the distribution of LC coefficients a_ν are displayed for one of the fourteen regions in Figure 2.3. This demonstrates that the maximum likelihood solutions for $r_{\rm ML}$ and $s_{\rm ML}$ are uncorrelated with each other and the LC coefficients.

Galaxy through chance cross-correlations. We focus on the effect of varying r on the detection limit, which we will not know until real measurements are made. We find the distribution of recovered maximum likelihood values $r_{\rm ML}$ for a given input r.

Using the simulations described in §2.2 and the maximum likelihood method described in §2.3, we generate realizations of CLASS-like data and infer best-fit parameters from them. The maps all have scalar fluctuations with a fixed normalization ($s = 1$) and the same foreground simulation from §2.2, while the tensor modes have varying strength $0 < r < 0.1$ uniformly sampled with one r every $\delta r = 5 \times 10^{-6}$. We display a subset of these simulations in Figure 2.5, marginalized over s and the LC coefficients.

Actual CLASS data will provide a maximum likelihood estimate $r_{\rm ML}$. Using simulated data similar to those from Figure 2.5, we will estimate the distribution of r using the slice $p(r|r_{\rm ML})$. Without knowledge of $r_{\rm ML}$, however, we need to marginalize over the possible values of $r_{\rm ML}$ that result from cosmic variance given a "true" r.

We estimate the constraining power of CLASS prior to a specific measurement $r_{\rm ML}$. Our goal is to calculate a probability distribution $p(r|r_{\rm true})$ that indicates our best estimate of r given some true value, $r_{\rm true}$. From simulations, we calculate the probability of a specific value of r given a measured $r_{\rm ML}$, $p(r|r_{\rm ML})$, and the probability of obtaining a given maximum likelihood result $r_{\rm ML}$ given the true value of r, $p(r_{\rm ML}|r_{\rm true})$. Using this information, we can marginalize over the nuisance parameter, $r_{\rm ML}$, i.e.

$$p(r|r_{\rm true}) = \int p(r|r_{\rm ML}) p(r_{\rm ML}|r_{\rm true})\, {\rm d}r_{\rm ML}. \tag{2.6}$$

The quantity $p(r|r_{\rm true})$ represents the average of a CLASS-like experiment's posterior

distribution for r over many realizations, given that the true amplitude of tensor fluctuations is $r_{\rm true}$. This statistic is motivated by noting a single CLASS-like experiment will produce a probability distribution $p(r|r_{\rm ML})$. The random variable $r_{\rm ML}$ is a draw from the distribution $p(r_{\rm ML}|r_{\rm true})$, and is not of inherent interest to this discussion. The $p(r_{\rm ML}|r_{\rm true})$ function acts as a kernel for a weighted average, and is used here to create a weighted average of each $p(r|r_{\rm ML})$, which results in the distribution $p(r|r_{\rm true})$. We illustrate this process in Figure 2.5 in which the histogram across the top gives a single realization of $p(r|r_{\rm ML})$ and the histogram on the right shows $p(r_{\rm ML}|r_{\rm true})$ for a specific value $r = r_{\rm true}$ for the input model. In this formalism, we can obtain a distribution of expected estimates of r given $r_{\rm true}$.

We also estimate the constraining power of CLASS's high-multipole data, with $\theta_{\rm pix} \sim 27.5'$ ($N_{\rm side} = 64$, $\ell \lesssim 100$). The model used here has a fixed scalar fluctuation amplitude $s = 1$ and spatially constant spectral indices. These simplifications are justified because foreground power spectra decay approximately as $C_\ell \propto \ell^{-2.5}$, and spurious correlations between the CMB and foregrounds are negligible at these scales (Page et al., 2007; Planck Collaboration, 2014). We use an internal linear combination (ILC) method similar to that used in the *WMAP* analysis (Hinshaw et al., 2007) to clean foregrounds, and then use PolSpice (Chon et al., 2004) to extract the B-mode power spectrum for multipoles $30 \leqslant \ell \leqslant 100$. By simulating maps with varying r as in the low-ℓ simulations, we find that we can describe the likelihood of r from the high-ℓ distribution with a Gaussian probability distribution $p(r|r_{\rm true}) \propto e^{-(r-r_{\rm true})^2/2\sigma^2}$ with $\sigma = 0.005$.

This analysis omits multipoles $24 \leqslant \ell \leqslant 29$, due to constraints from both the low-ℓ and high-ℓ software. For the pixel-based approach at low-ℓ, the Healpix

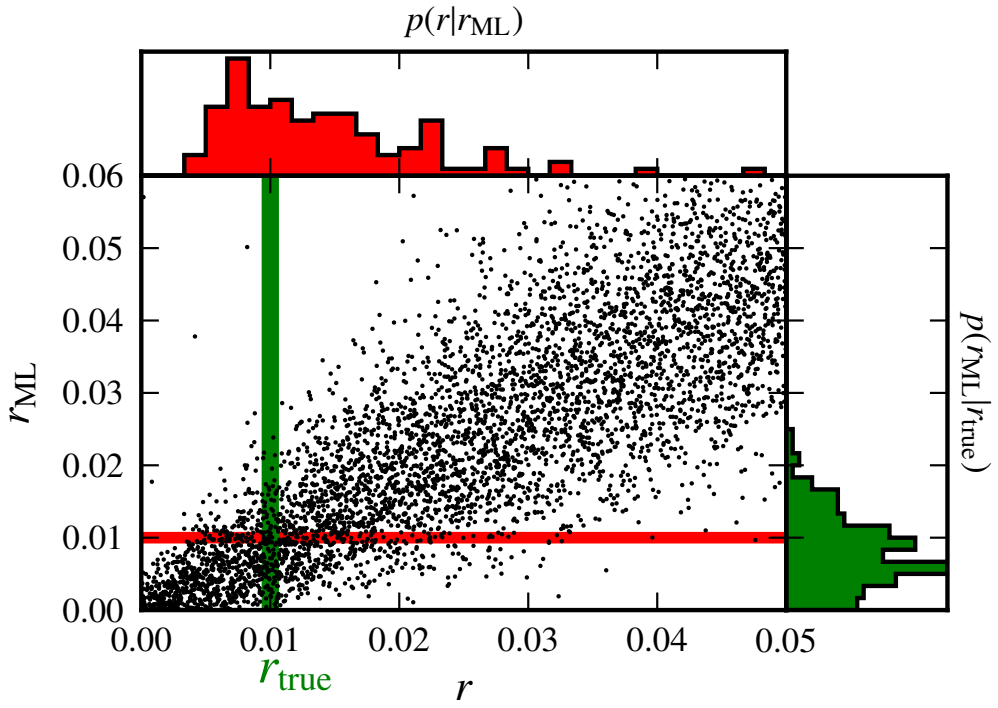

Figure 2.5: Each point in the bottom-left plot represents a unique realization of the simulations described in §2.2. Given an input tensor-to-scalar ratio r we compute the distribution of recovered maximum likelihood values $r_{\rm ML}$. We also display sample distributions of $r_{\rm ML}$ given an $r_{\rm true} = 0.01 \pm 0.0005$ (green histogram) in the right plot, and of r given an $r_{\rm ML} = 0.01 \pm 0.0005$ (red histogram) in the top plot. To obtain our posterior distribution of r given a value $r_{\rm true}$, we integrate the product of these distributions over $r_{\rm ML}$ (Equation 2.6).

documentation recommends using $\ell_{\rm max} = 3N_{\rm side} - 1 = 23$ to avoid oversampling each pixel, while PolSpice introduces mode-coupling effects in the power spectrum for $\ell \lesssim 30$.

With the distribution for $r_{\rm true} = 0$, we obtain the range of potential false positive results, which suggests a definition of our upper limit as the value of r that contains 95% of the area under the curve from $r = 0$, yielding $r < 0.017$ for low-ℓ data alone, and $r < 0.008$ using the high-ℓ simulations as well. Similarly, we estimate the expected range of recovered r for $r_{\rm true} = 0.01$, and find that the 68% confidence interval, defined as the percentiles $(0.16, 0.5, 0.84)$, gives $r = 0.011^{+0.011}_{-0.007}$ ($r = 0.010^{+0.004}_{-0.004}$ including high-ℓ). These distributions are displayed in Figure 2.6. Using a simple likelihood ratio test based on these curves with $\mathscr{L}(r) \equiv p(r|r_{\rm true} = 0.01)$, we find a likelihood ratio for the low-ℓ data with $\mathscr{L}(0)/\mathscr{L}(0.01) = 0.52$, corresponding to a PTE of 0.13, or a significance of 1.2σ. Including high-ℓ data gives a projected $\mathscr{L}(0)/\mathscr{L}(0.01) = 0.07$, corresponding to a PTE of 0.01, or a significance of 2.3σ.

2.5 Conclusions

In this work, we have simulated CMB polarization maps on a cut sky contaminated by diffuse foreground emission and Gaussian white noise. We recovered the input CMB by solving for maximum-likelihood maps using a pixel-based maximum likelihood method tailored to measure the reionization peak ($\ell \leqslant 23$). We have found the following.

- We found unbiased estimates of the amplitudes of scalar and tensor fluctuations with a four-frequency maximum likelihood analysis accounting for CLASS-like noise, a cut sky, and foregrounds with spatially varying spectral indices.

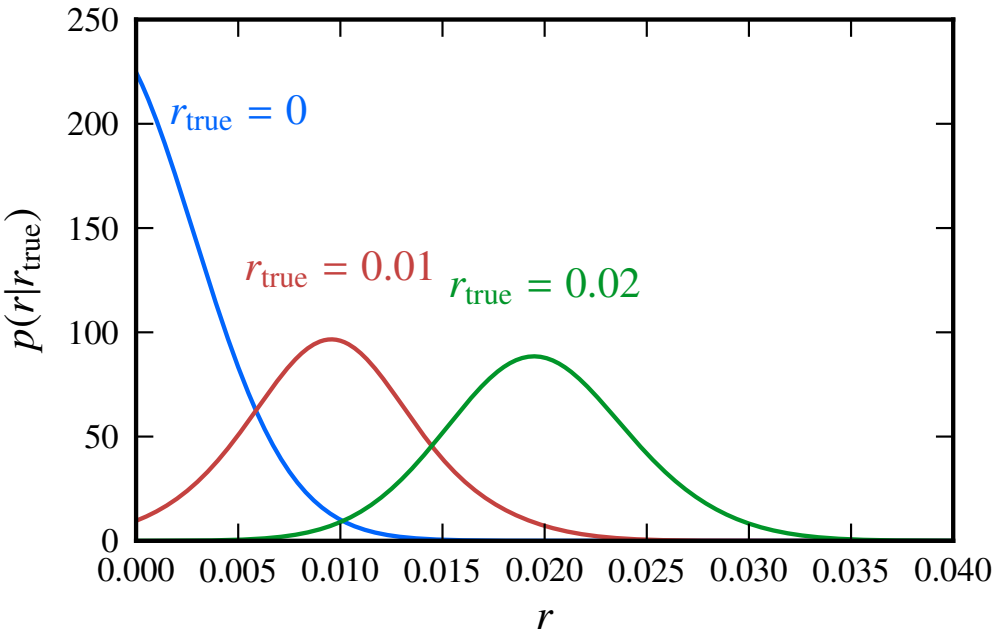

Figure 2.6: We estimate the distributions for r from Equation 2.6, and use a Gaussian kernel density estimator to obtain a continuous curve, which returns a normalized probability density by default. The dashed lines are the distributions given only the low-ℓ data ($2 \leqslant \ell \leqslant 23$), while the solid curves are a product of the low-ℓ distributions and a Gaussian estimate of the high-ℓ ($30 \leqslant \ell \leqslant 100$) distribution with mean $\mu = r_{\rm true}$ and standard deviation $\sigma = 0.005$. The solid curve for $r_{\rm true} = 0$ gives a 95% C.L. upper limit $r < 0.008$, while for the other solid curves the 95% C.L. limits are $0.006 < r < 0.014$ and $0.015 < r < 0.024$.

- We have found that, by using only polarization the reionization peak ($2 \leqslant \ell \leqslant 23$), data from a five-year CLASS-like experiment would produce a 95% upper limit of $r < 0.017$, which improves to $r < 0.008$ when we include high-ℓ data ($30 \leqslant \ell \leqslant 100$).

- Our pixel-based low-multipole maximum likelihood solution is straightforward to run and implement, and is stable to foreground complications, i.e. variable spectral indices and polarization fractions.

Although CLASS's primary purpose is constraining the amplitude of tensor fluctuations, a foreground-cleaned measurement of CMB polarization on the largest scales can help constrain several other cosmological parameters. Our cosmic variance-limited measurement of the large-scale E-mode power spectrum will improve on the current *WMAP* and *Planck* measurements of the optical depth τ to reionization by a factor of four. Not only can optical depth measurements constrain cosmic reionization scenarios, but it can also further constrain the amplitude of primordial density fluctuations A_s, whose precision is limited by its degeneracy with τ. With a tightly constrained A_s measurement, comparisons with the amplitude of large scale structure of the Universe, σ_8, can be used to infer the sum of neutrino masses to 0.015 eV (Allison et al., 2015). Finally, the observed anomalies in the temperature fluctuations on large angular scales require polarization measurements on the same scales to probe physics beyond standard ΛCDM (Bennett et al., 2011; Planck Collaboration, 2015d).

References

Hinshaw, G., D. Larson, E. Komatsu, D. N. Spergel, C. L. Bennett, J. Dunkley, M. R. Nolta, M. Halpern, R. S. Hill, N. Odegard, L. Page, K. M. Smith, J. L. Weiland, B. Gold, N. Jarosik, A. Kogut, M. Limon, S. S. Meyer, G. S. Tucker, E. Wollack, and E. L. Wright (2013). "Nine-year Wilkinson Microwave Anisotropy Probe (WMAP) Observations: Cosmological Parameter Results". In: ApJS 208, 19, p. 19. DOI: 10.1088/0067-0049/208/2/19. arXiv: 1212.5226.

Planck Collaboration (2015c). "Planck 2015 results. XIII. Cosmological parameters". In: *ArXiv e-prints*. arXiv: 1502.01589.

Guth, A. H. (1981). "Inflationary universe: A possible solution to the horizon and flatness problems". In: Phys. Rev. D 23, pp. 347–356. DOI: 10.1103/PhysRevD.23.347.

Starobinsky, A. A. (1980). "A new type of isotropic cosmological models without singularity". In: *Physics Letters B* 91, pp. 99–102. DOI: 10.1016/0370-2693(80)90670-X.

Kazanas, D. (1980). "Dynamics of the universe and spontaneous symmetry breaking". In: ApJ 241, pp. L59–L63. DOI: 10.1086/183361.

Mukhanov, V. F. and G. V. Chibisov (1981). "Quantum fluctuations and a nonsingular universe". In: *Soviet Journal of Experimental and Theoretical Physics Letters* 33, p. 532.

Einhorn, M. B. and K. Sato (1981). "Monopole production in the very early universe in a first-order phase transition". In: *Nuclear Physics B* 180, pp. 385–404. DOI: 10.1016/0550-3213(81)90057-2.

Linde, A. D. (1982). "A new inflationary universe scenario: A possible solution of the horizon, flatness, homogeneity, isotropy and primordial monopole problems". In: *Physics Letters B* 108, pp. 389–393. DOI: 10.1016/0370-2693(82)91219-9.

Albrecht, A. and P. J. Steinhardt (1982). "Cosmology for grand unified theories with radiatively induced symmetry breaking". In: *Physical Review Letters* 48, pp. 1220–1223. DOI: 10.1103/PhysRevLett.48.1220.

Bennett, C. L., D. Larson, J. L. Weiland, N. Jarosik, G. Hinshaw, N. Odegard, K. M. Smith, R. S. Hill, B. Gold, M. Halpern, E. Komatsu, M. R. Nolta, L. Page, D. N. Spergel, E. Wollack, J. Dunkley, A. Kogut, M. Limon, S. S. Meyer, G. S. Tucker, and E. L. Wright (2013). "Nine-year Wilkinson Microwave Anisotropy Probe (WMAP) Observations: Final Maps and Results". In: ApJS 208, 20, p. 20. DOI: 10.1088/0067-0049/208/2/20. arXiv: 1212.5225.

Polnarev, A. G. (1985). "Polarization and Anisotropy Induced in the Microwave Background by Cosmological Gravitational Waves". In: Soviet Ast. 62, pp. 1041–1052.

Seljak, U. and M. Zaldarriaga (1997). "Signature of Gravity Waves in the Polarization of the Microwave Background". In: *Physical Review Letters* 78, pp. 2054–2057. DOI: 10.1103/PhysRevLett.78.2054. eprint: astro-ph/9609169.

Kamionkowski, M., A. Kosowsky, and A. Stebbins (1997). "Statistics of cosmic microwave background polarization". In: Phys. Rev. D 55, pp. 7368–7388. DOI: 10.1103/PhysRevD.55.7368. eprint: astro-ph/9611125.

Hu, W. and M. White (1997). "A CMB Polarization Primer". In: *New Astronomy* 2.4, pp. 323 –344. ISSN: 1384-1076. DOI: http://dx.doi.org/10.1016/S1384-1076(97)00022-5. eprint: astro-ph/9706147. URL: http://www.sciencedirect.com/science/article/pii/S1384107697000225.

BICEP2/Keck Collaboration, Planck Collaboration, P. A. R. Ade, N. Aghanim, Z. Ahmed, R. W. Aikin, K. D. Alexander, M. Arnaud, J. Aumont, C. Baccigalupi, and et al. (2015). "Joint Analysis of BICEP2/Keck Array and Planck Data". In: *Physical Review Letters* 114.10, 101301, p. 101301. DOI: 10.1103/PhysRevLett.114.101301. arXiv: 1502.00612.

Planck Collaboration (2015e). "Planck 2015 results. XX. Constraints on inflation". In: *ArXiv e-prints*. arXiv: 1502.02114.

Eimer, J. R., C. L. Bennett, D. T. Chuss, T. Marriage, E. J. Wollack, and L. Zeng (2012). "The cosmology large angular scale surveyor (CLASS): 40 GHz optical design". In: *Society of Photo-Optical Instrumentation Engineers (SPIE) Conference Series*. Vol. 8452. Society of Photo-Optical Instrumentation Engineers (SPIE) Conference Series, pp. 845220–845220–15. DOI: 10.1117/12.925464. arXiv: 1211.0041 [astro-ph.IM].

Essinger-Hileman, T., A. Ali, M. Amiri, J. W. Appel, D. Araujo, C. L. Bennett, F. Boone, M. Chan, H.-M. Cho, D. T. Chuss, F. Colazo, E. Crowe, K. Denis, R. Dünner, J. Eimer, D. Gothe, M. Halpern, K. Harrington, G. C. Hilton, G. F. Hinshaw, C. Huang, K. Irwin, G. Jones, J. Karakla, A. J. Kogut, D. Larson, M. Limon, L. Lowry, T. Marriage, N. Mehrle, A. D. Miller, N. Miller, S. H.

Moseley, G. Novak, C. Reintsema, K. Rostem, T. Stevenson, D. Towner, K. U-Yen, E. Wagner, D. Watts, E. J. Wollack, Z. Xu, and L. Zeng (2014). "CLASS: the cosmology large angular scale surveyor". In: *Millimeter, Submillimeter, and Far-Infrared Detectors and Instrumentation for Astronomy VII*. Vol. 9153. Proc. SPIE, p. 91531I. DOI: 10.1117/12.2056701. arXiv: 1408.4788 [astro-ph.IM].

Rostem, K., A. Ali, J. W. Appel, C. L. Bennett, D. T. Chuss, F. A. Colazo, E. Crowe, K. L. Denis, T. Essinger-Hileman, T. A. Marriage, S. H. Moseley, T. R. Stevenson, D. W. Towner, K. U-Yen, and E. J. Wollack (2014). "Scalable background-limited polarization-sensitive detectors for mm-wave applications". In: *Society of Photo-Optical Instrumentation Engineers (SPIE) Conference Series*. Vol. 9153. Society of Photo-Optical Instrumentation Engineers (SPIE) Conference Series, 91530B–91530B–7. DOI: 10.1117/12.2057266. arXiv: 1408.4790 [astro-ph.IM].

Appel, J. W., A. Ali, M. Amiri, D. Araujo, C. L. Bennet, F. Boone, M. Chan, H.-M. Cho, D. T. Chuss, F. Colazo, E. Crowe, K. Denis, R. Dünner, J. Eimer, T. Essinger-Hileman, D. Gothe, M. Halpern, K. Harrington, G. Hilton, G. F. Hinshaw, C. Huang, K. Irwin, G. Jones, J. Karakula, A. J. Kogut, D. Larson, M. Limon, L. Lowry, T. Marriage, N. Mehrle, A. D. Miller, N. Miller, S. H. Moseley, G. Novak, C. Reintsema, K. Rostem, T. Stevenson, D. Towner, K. U-Yen, E. Wagner, D. Watts, E. Wollack, Z. Xu, and L. Zeng (2014). "The cosmology large angular scale surveyor (CLASS): 38-GHz detector array of bolometric polarimeters". In: *Society of Photo-Optical Instrumentation Engineers (SPIE) Conference Series*. Vol. 9153. Society of Photo-Optical Instrumentation Engineers (SPIE) Conference Series, 91531J–91531J–15. DOI: 10.1117/12.2056530. arXiv: 1408.4789 [astro-ph.IM].

Planck Collaboration (2015a). "Planck 2015 results. I. Overview of products and scientific results". In: *ArXiv e-prints*. arXiv: 1502.01582.

Chuss, D. T., E. J. Wollack, R. Henry, H. Hui, A. J. Juarez, M. Krejny, S. H. Moseley, and G. Novak (2012). "Properties of a variable-delay polarization modulator". In: Appl. Opt. 51, p. 197. DOI: 10.1364/AO.51.000197. arXiv: 1106.5984 [astro-ph.IM].

Lazear, J., P. A. R. Ade, D. Benford, C. L. Bennett, D. T. Chuss, J. L. Dotson, J. R. Eimer, D. J. Fixsen, M. Halpern, G. Hilton, J. Hinderks, G. F. Hinshaw, K. Irwin, C. Jhabvala, B. Johnson, A. Kogut, L. Lowe, J. J. McMahon, T. M. Miller, P. Mirel, S. H. Moseley, S. Rodriguez, E. Sharp, J. G. Staguhn, E. R. Switzer, C. E. Tucker, A. Weston, and E. J. Wollack (2014). "The Primordial Inflation Polarization Explorer (PIPER)". In: Society of Photo-Optical Instrumentation Engineers (SPIE) Conference Series 9153, 91531L, pp. 91531L–91531L–11. DOI: 10.1117/12.2056806. arXiv: 1407.2584 [astro-ph.IM].

López-Caniego, M., R. Rebolo, M. Aguiar, R. Génova-Santos, F. Gómez-Reñasco, C. Gutierrez, J. M. Herreros, R. J. Hoyland, C. López-Caraballo, A. E. Pelaez Santos, F. Poidevin, J. A. Rubiño-Martín, V. Sanchez de la Rosa, D. Tramonte, A. Vega-Moreno, T. Viera-Curbelo, R. Vignaga, E. Martínez-González, R. B. Barreiro, B. Casaponsa, F. J. Casas, J. M. Diego, R. Fernández-Cobos, D. Herranz, D. Ortiz, P. Vielva, E. Artal, B. Aja, J. Cagigas, J. L. Cano, L. de la Fuente, A. Mediavilla, J. V. Terán, E. Villa, L. Piccirillo, R. Battye, E. Blackhurst, M. Brown, R. D. Davies, R. J. Davis, C. Dickinson, K. Grainge, S. Harper, B. Maffei, M. McCulloch, S. Melhuish, G. Pisano, R. A. Watson, M. Hobson, A. Lasenby, R. Saunders, and P. Scott (2014). "The QUIJOTE CMB Experiment: status and first results with the multi-frequency instrument". In: *ArXiv e-prints*. arXiv: 1401.4690 [astro-ph.IM].

Aiola, S., G. Amico, P. Battaglia, E. Battistelli, A. Baó, P. de Bernardis, M. Bersanelli, A. Boscaleri, F. Cavaliere, A. Coppolecchia, A. Cruciani, F. Cuttaia, A. D'Addabbo, G. D'Alessandro, S. De Gregori, F. Del Torto, M. De Petris, L. Fiorineschi, C. Franceschet, E. Franceschi, M. Gervasi, D. Goldie, A. Gregorio, V. Haynes, N. Krachmalnicoff, L. Lamagna, B. Maffei, D. Maino, S. Masi, A. Mennella, G. Morgante, F. Nati, M. W. Ng, L. Pagano, A. Passerini, O. Peverini, F. Piacentini, L. Piccirillo, G. Pisano, S. Ricciardi, P. Rissone, G. Romeo, M. Salatino, M. Sandri, A. Schillaci, L. Stringhetti, A. Tartari, R. Tascone, L. Terenzi, M. Tomasi, E. Tommasi, F. Villa, G. Virone, S. Withington, A. Zacchei, and M. Zannoni (2012). "The Large-Scale Polarization Explorer (LSPE)". In: *Society of Photo-Optical Instrumentation Engineers (SPIE) Conference Series*. Vol. 8446. Society of Photo-Optical Instrumentation Engineers (SPIE) Conference Series, 84467A–84467A–12. DOI: 10.1117/12.926095.

Tajima, O., J. Choi, M. Hazumi, H. Ishitsuka, M. Kawai, and M. Yoshida (2012). "GroundBIRD: an experiment for CMB polarization measurements at a large angular scale from the ground". In: *Society of Photo-Optical Instrumentation Engineers (SPIE) Conference Series*. Vol. 8452. Society of Photo-Optical Instrumentation Engineers (SPIE) Conference Series, pp. 84521M–84521M–9. DOI: 10.1117/12.925816.

Ogburn IV, R. W., P. A. R. Ade, R. W. Aikin, M. Amiri, S. J. Benton, J. J. Bock, J. A. Bonetti, J. A. Brevik, B. Burger, C. D. Dowell, L. Duband, J. P. Filippini, S. R. Golwala, M. Halpern, M. Hasselfield, G. Hilton, V. V. Hristov, K. Irwin, J. P. Kaufman, B. G. Keating, J. M. Kovac, C. L. Kuo, A. E. Lange, E. M. Leitch, C. B. Netterfield, H. T. Nguyen, A. Orlando, C. L. Pryke, C. Reintsema, S. Richter, J. E. Ruhl, M. C. Runyan, C. D. Sheehy, Z. K. Staniszewski, S. A. Stokes, R. V. Sudiwala, G. P. Teply, J. E. Tolan, A. D. Turner, P. Wilson, and

C. L. Wong (2010). “The BICEP2 CMB polarization experiment”. In: *Society of Photo-Optical Instrumentation Engineers (SPIE) Conference Series*. Vol. 7741. Society of Photo-Optical Instrumentation Engineers (SPIE) Conference Series, 77411G–77411G–11. DOI: 10.1117/12.857864.

Austermann, J. E., K. A. Aird, J. A. Beall, D. Becker, A. Bender, B. A. Benson, L. E. Bleem, J. Britton, J. E. Carlstrom, C. L. Chang, H. C. Chiang, H.-M. Cho, T. M. Crawford, A. T. Crites, A. Datesman, T. de Haan, M. A. Dobbs, E. M. George, N. W. Halverson, N. Harrington, J. W. Henning, G. C. Hilton, G. P. Holder, W. L. Holzapfel, S. Hoover, N. Huang, J. Hubmayr, K. D. Irwin, R. Keisler, J. Kennedy, L. Knox, A. T. Lee, E. Leitch, D. Li, M. Lueker, D. P. Marrone, J. J. McMahon, J. Mehl, S. S. Meyer, T. E. Montroy, T. Natoli, J. P. Nibarger, M. D. Niemack, V. Novosad, S. Padin, C. Pryke, C. L. Reichardt, J. E. Ruhl, B. R. Saliwanchik, J. T. Sayre, K. K. Schaffer, E. Shirokoff, A. A. Stark, K. Story, K. Vanderlinde, J. D. Vieira, G. Wang, R. Williamson, V. Yefremenko, K. W. Yoon, and O. Zahn (2012). “SPTpol: an instrument for CMB polarization measurements with the South Pole Telescope”. In: *Society of Photo-Optical Instrumentation Engineers (SPIE) Conference Series*. Vol. 8452. Society of Photo-Optical Instrumentation Engineers (SPIE) Conference Series, 84521E–84521E–18. DOI: 10.1117/12.927286. arXiv: 1210.4970 [astro-ph.IM].

Essinger-Hileman, T., J. W. Appel, J. A. Beall, H. M. Cho, J. Fowler, M. Halpern, M. Hasselfield, K. D. Irwin, T. A. Marriage, M. D. Niemack, L. Page, L. P. Parker, S. Pufu, S. T. Staggs, O. Stryzak, C. Visnjic, K. W. Yoon, and Y. Zhao (2010). “The Atacama B-Mode Search: CMB Polarimetry with Transition-Edge-Sensor Bolometers”. In: *ArXiv e-prints*. arXiv: 1008.3915 [astro-ph.IM].

Niemack, M. D., P. A. R. Ade, J. Aguirre, F. Barrientos, J. A. Beall, J. R. Bond, J. Britton, H. M. Cho, S. Das, M. J. Devlin, S. Dicker, J. Dunkley, R. Dünner, J. W. Fowler, A. Hajian, M. Halpern, M. Hasselfield, G. C. Hilton, M. Hilton, J. Hubmayr, J. P. Hughes, L. Infante, K. D. Irwin, N. Jarosik, J. Klein, A. Kosowsky, T. A. Marriage, J. McMahon, F. Menanteau, K. Moodley, J. P. Nibarger, M. R. Nolta, L. A. Page, B. Partridge, E. D. Reese, J. Sievers, D. N. Spergel, S. T. Staggs, R. Thornton, C. Tucker, E. Wollack, and K. W. Yoon (2010). “ACTPol: a polarization-sensitive receiver for the Atacama Cosmology Telescope”. In: *Society of Photo-Optical Instrumentation Engineers (SPIE) Conference Series*. Vol. 7741. Society of Photo-Optical Instrumentation Engineers (SPIE) Conference Series, 77411S–77411S–21. DOI: 10.1117/12.857464. arXiv: 1006.5049 [astro-ph.IM].

Kermish, Z. D., P. Ade, A. Anthony, K. Arnold, D. Barron, D. Boettger, J. Borrill, S. Chapman, Y. Chinone, M. A. Dobbs, J. Errard, G. Fabbian, D. Flanigan, G. Fuller,

A. Ghribi, W. Grainger, N. Halverson, M. Hasegawa, K. Hattori, M. Hazumi, W. L. Holzapfel, J. Howard, P. Hyland, A. Jaffe, B. Keating, T. Kisner, A. T. Lee, M. Le Jeune, E. Linder, M. Lungu, F. Matsuda, T. Matsumura, X. Meng, N. J. Miller, H. Morii, S. Moyerman, M. J. Myers, H. Nishino, H. Paar, E. Quealy, C. L. Reichardt, P. L. Richards, C. Ross, A. Shimizu, M. Shimon, C. Shimmin, M. Sholl, P. Siritanasak, H. Spieler, N. Stebor, B. Steinbach, R. Stompor, A. Suzuki, T. Tomaru, C. Tucker, and O. Zahn (2012). "The POLARBEAR experiment". In: *Society of Photo-Optical Instrumentation Engineers (SPIE) Conference Series*. Vol. 8452. Society of Photo-Optical Instrumentation Engineers (SPIE) Conference Series, pp. 84521C–84521C–15. DOI: 10.1117/12.926354. arXiv: 1210.7768 [astro-ph.IM].

Oxley, P., P. A. Ade, C. Baccigalupi, P. deBernardis, H.-M. Cho, M. J. Devlin, S. Hanany, B. R. Johnson, T. Jones, A. T. Lee, T. Matsumura, A. D. Miller, M. Milligan, T. Renbarger, H. G. Spieler, R. Stompor, G. S. Tucker, and M. Zaldarriaga (2004). "The EBEX experiment". In: *Infrared Spaceborne Remote Sensing XII*. Ed. by M. Strojnik. Vol. 5543. Society of Photo-Optical Instrumentation Engineers (SPIE) Conference Series, pp. 320–331. DOI: 10.1117/12.563447. eprint: astro-ph/0501111.

Filippini, J. P., P. A. R. Ade, M. Amiri, S. J. Benton, R. Bihary, J. J. Bock, J. R. Bond, J. A. Bonetti, S. A. Bryan, B. Burger, H. C. Chiang, C. R. Contaldi, B. P. Crill, O. Doré, M. Farhang, L. M. Fissel, N. N. Gandilo, S. R. Golwala, J. E. Gudmundsson, M. Halpern, M. Hasselfield, G. Hilton, W. Holmes, V. V. Hristov, K. D. Irwin, W. C. Jones, C. L. Kuo, C. J. MacTavish, P. V. Mason, T. E. Montroy, T. A. Morford, C. B. Netterfield, D. T. O'Dea, A. S. Rahlin, C. D. Reintsema, J. E. Ruhl, M. C. Runyan, M. A. Schenker, J. A. Shariff, J. D. Soler, A. Trangsrud, C. Tucker, R. S. Tucker, and A. D. Turner (2010). "SPIDER: a balloon-borne CMB polarimeter for large angular scales". In: *Society of Photo-Optical Instrumentation Engineers (SPIE) Conference Series*. Vol. 7741. Society of Photo-Optical Instrumentation Engineers (SPIE) Conference Series, 77411N–77411N–12. DOI: 10.1117/12.857720. arXiv: 1106.2158 [astro-ph.CO].

Planck Collaboration (2015b). "Planck 2015 results. X. Diffuse component separation: Foreground maps". In: *ArXiv e-prints*. arXiv: 1502.01588.

Planck Collaboration (2015f). "Planck intermediate results. XXII. Frequency dependence of thermal emission from Galactic dust in intensity and polarization". In: A&A 576, A107, A107. DOI: 10.1051/0004-6361/201424088. arXiv: 1405.0874.

Fuskeland, U., I. K. Wehus, H. K. Eriksen, and S. K. Næss (2014). "Spatial Variations in the Spectral Index of Polarized Synchrotron Emission in the 9yr WMAP Sky

Maps". In: ApJ 790, 104, p. 104. DOI: 10.1088/0004-637X/790/2/104. arXiv: 1404.5323.

Górski, K. M., E. Hivon, A. J. Banday, B. D. Wandelt, F. K. Hansen, M. Reinecke, and M. Bartelmann (2005). "HEALPix: A Framework for High-Resolution Discretization and Fast Analysis of Data Distributed on the Sphere". In: ApJ 622, pp. 759–771. DOI: 10.1086/427976. eprint: astro-ph/0409513.

Page, L., G. Hinshaw, E. Komatsu, M. R. Nolta, D. N. Spergel, C. L. Bennett, C. Barnes, R. Bean, O. Doré, J. Dunkley, M. Halpern, R. S. Hill, N. Jarosik, A. Kogut, M. Limon, S. S. Meyer, N. Odegard, H. V. Peiris, G. S. Tucker, L. Verde, J. L. Weiland, E. Wollack, and E. L. Wright (2007). "Three-Year Wilkinson Microwave Anisotropy Probe (WMAP) Observations: Polarization Analysis". In: ApJS 170, pp. 335–376. DOI: 10.1086/513699. eprint: astro-ph/0603450.

Delabrouille, J., M. Betoule, J. B. Melin, M. A. Miville- Deschênes, J. Gonzalez-Nuevo, M. Le Jeune, G. Castex, G. de Zotti, S. Basak, M. Ashdown, J. Aumont, C. Baccigalupi, A. J. Banday, J. P. Bernard, F. R. Bouchet, D. L. Clements, A. da Silva, C. Dickinson, F. Dodu, K. Dolag, F. Elsner, L. Fauvet, G. Faÿ, G. Giardino, S. Leach, J. Lesgourgues, M. Liguori, J. F. Macías-Pérez, M. Massardi, S. Matarrese, P. Mazzotta, L. Montier, S. Mottet, R. Paladini, B. Partridge, R. Piffaretti, G. Prezeau, S. Prunet, S. Ricciardi, M. Roman, B. Schaefer, and L. Toffolatti (2013). "The pre-launch Planck Sky Model: a model of sky emission at submillimetre to centimetre wavelengths". In: A&A 553, A96, A96. DOI: 10.1051/0004-6361/201220019. arXiv: 1207.3675 [astro-ph.CO].

Miville-Deschênes, M.-A., N. Ysard, A. Lavabre, N. Ponthieu, J. F. Macías-Pérez, J. Aumont, and J. P. Bernard (2008). "Separation of anomalous and synchrotron emissions using WMAP polarization data". In: A&A 490, pp. 1093–1102. DOI: 10.1051/0004-6361:200809484. arXiv: 0802.3345.

Finkbeiner, D. P., M. Davis, and D. J. Schlegel (1999). "Extrapolation of Galactic Dust Emission at 100 Microns to Cosmic Microwave Background Radiation Frequencies Using FIRAS". In: ApJ 524, pp. 867–886. DOI: 10.1086/307852. eprint: astro-ph/9905128.

Miller, N. J., D. T. Chuss, T. A. Marriage, E. J. Wollack, J. W. Appel, C. L. Bennett, J. Eimer, T. Essinger-Hileman, D. J. Fixsen, K. Harrington, S. H. Moseley, K. Rostem, E. R. Switzer, and D. J. Watts (2015). "Recovery of Large Angular Scale CMB Polarization for Instruments Employing Variable-delay Polarization Modulators". In: *ArXiv e-prints*. arXiv: 1509.04628 [astro-ph.IM].

Efstathiou, G. (2006). "Hybrid estimation of cosmic microwave background polarization power spectra". In: MNRAS 370, pp. 343–362. DOI: 10.1111/j.1365-2966.2006.10486.x. eprint: astro-ph/0601107.

Katayama, N. and E. Komatsu (2011). "Simple Foreground Cleaning Algorithm for Detecting Primordial B-mode Polarization of the Cosmic Microwave Background". In: ApJ 737, 78, p. 78. DOI: 10.1088/0004-637X/737/2/78. arXiv: 1101.5210 [astro-ph.CO].

Efstathiou, G., S. Gratton, and F. Paci (2009). "Impact of Galactic polarized emission on B-mode detection at low multipoles". In: MNRAS 397, pp. 1355–1373. DOI: 10.1111/j.1365-2966.2009.14995.x. arXiv: 0902.4803.

Byrd, Richard H., Peihuang Lu, Jorge Nocedal, and Ciyou Zhu (1995). "A Limited Memory Algorithm for Bound Constrained Optimization". In: *SIAM J. Sci. Comput.* 16.5, pp. 1190–1208. ISSN: 1064-8275. DOI: 10.1137/0916069. URL: http://dx.doi.org/10.1137/0916069.

Planck Collaboration (2014). "Planck intermediate results. XXX. The angular power spectrum of polarized dust emission at intermediate and high Galactic latitudes". In: *ArXiv e-prints*. arXiv: 1409.5738.

Hinshaw, G., M. R. Nolta, C. L. Bennett, R. Bean, O. Doré, M. R. Greason, M. Halpern, R. S. Hill, N. Jarosik, A. Kogut, E. Komatsu, M. Limon, N. Odegard, S. S. Meyer, L. Page, H. V. Peiris, D. N. Spergel, G. S. Tucker, L. Verde, J. L. Weiland, E. Wollack, and E. L. Wright (2007). "Three-Year Wilkinson Microwave Anisotropy Probe (WMAP) Observations: Temperature Analysis". In: ApJS 170, pp. 288–334. DOI: 10.1086/513698. eprint: astro-ph/0603451.

Chon, G., A. Challinor, S. Prunet, E. Hivon, and I. Szapudi (2004). "Fast estimation of polarization power spectra using correlation functions". In: MNRAS 350, pp. 914–926. DOI: 10.1111/j.1365-2966.2004.07737.x. eprint: astro-ph/0303414.

Allison, R., P. Caucal, E. Calabrese, J. Dunkley, and T. Louis (2015). "Towards a cosmological neutrino mass detection". In: *ArXiv e-prints*. arXiv: 1509.07471.

Bennett, C. L., R. S. Hill, G. Hinshaw, D. Larson, K. M. Smith, J. Dunkley, B. Gold, M. Halpern, N. Jarosik, A. Kogut, E. Komatsu, M. Limon, S. S. Meyer, M. R. Nolta, N. Odegard, L. Page, D. N. Spergel, G. S. Tucker, J. L. Weiland, E. Wollack, and E. L. Wright (2011). "Seven-year Wilkinson Microwave Anisotropy Probe (WMAP) Observations: Are There Cosmic Microwave Background Anomalies?" In: ApJS 192, 17, p. 17. DOI: 10.1088/0067-0049/192/2/17. arXiv: 1001.4758 [astro-ph.CO].

Planck Collaboration (2015d). "Planck 2015 results. XVI. Isotropy and statistics of the CMB". In: *ArXiv e-prints*. arXiv: 1506.07135.

Chapter 3

A projected estimate of the reionization optical depth using the CLASS experiment's sample-variance limited E-mode measurement

3.1 Introduction

Measurements of the cosmic microwave background (CMB) have tightly constrained the properties of the large-scale observable universe, with the reionization optical depth τ left as the worst-determined fundamental ΛCDM parameter (Bennett et al., 2013; Planck Collaboration XIII, 2016). The importance of polarization measurements has become more critical as the *Planck* experiment has measured the unpolarized temperature anisotropy over the full sky to its sample variance limit up to a resolution of $\theta \gtrsim 7'$ ($\ell \lesssim 1600$) (§3.8 of Planck Collaboration XI 2016, albeit with potential complications, see Addison et al. 2016). At sub-degree angular scales ($\ell \gtrsim 200$), polarization power is sourced by primordial scalar fluctuations with extra

correlations induced by gravitational lensing (e.g. Hu and Okamoto, 2004; Galli et al., 2014; Louis et al., 2017; Henning et al., 2017). At larger angular scales, gradient-like E-mode polarization measurements can tightly constrain the reionization optical depth τ via the rough scaling $C^{\mathrm{EE}}_{2\leqslant\ell\leqslant 20} \propto \tau^2$ (Page et al., 2007), while we can use the curl-like B-mode polarization measurements to constrain the amplitude of stochastic gravitational waves that the inflationary paradigm predicts, whose amplitude is parameterized by the ratio r of tensor-to-scalar fluctuations in the metric (Guth, 1981; Starobinsky, 1980; Kazanas, 1980; Mukhanov and Chibisov, 1981; Einhorn and Sato, 1981; Linde, 1982; Albrecht and Steinhardt, 1982; Kamionkowski, Kosowsky, and Stebbins, 1997; Seljak and Zaldarriaga, 1997). The CLASS experiment is uniquely and specially designed to constrain r and τ by recovering the largest scale fluctuations of the polarized cosmic microwave background across 70% of the sky (Eimer et al., 2012; Essinger-Hileman et al., 2014; Harrington et al., 2016).

The reionization optical depth τ is the total free electron opacity to the surface of last scattering,

$$\tau = \int_{t_{\mathrm{lss}}}^{t_0} n_{\mathrm{e}}(t)\sigma_{\mathrm{T}} c \, \mathrm{d}t, \tag{3.1}$$

where $n_{\mathrm{e}}(t)$ is the average number density of free electrons from the time of last scattering t_{lss} to today t_0 and σ_{T} is the Thomson scattering cross section. For $\tau \ll 1$, the reionization optical depth is the probability that a CMB photon was scattered by free electrons from reionization. The redshift of reionization can be defined if one assumes that $n_{\mathrm{e}}(t)$ is nearly a step function, but it is likely that reionization was an extended process, with evidence of significant contributions to τ up to $z \sim 16$ (Heinrich, Miranda, and Hu, 2017).

From measurements of QSO absorption lines via the Gunn-Peterson effect (Gunn

and Peterson, 1965), we know that the universe was ionized by redshift $z = 6$, corresponding to a lower limit of $\tau \gtrsim 0.038$ if we assume instantaneous reionization (Fan et al., 2006; Planck Collaboration Int. XLVII, 2016). The quantity τ can be constrained using measurements of the temperature-E-mode cross-correlation and the E-mode auto-correlation C_ℓ^{TE} and C_ℓ^{EE} at the largest angular scales. The *Planck* and *WMAP* measurements are limited in precision by sample variance in the C_ℓ^{TE} case, and by instrumental noise and systematic effects in the C_ℓ^{EE} case, with the latest limits from *Planck* giving $\tau \sim 0.06 \pm 0.01$ (Planck Collaboration et al., 2016; Planck Collaboration Int. XLVII, 2016), although the amplitude of unexplained large-scale signals in the *Planck* maps create extra uncertainty and potential biases in this measurement (Weiland et al., 2018). It is possible to obtain this constraint using only temperature anisotropy, CMB lensing, and baryon acoustic oscillation (BAO) data as an independent check. In particular, `PlanckTT+lensing+BAO` data constrain $\tau = 0.067 \pm 0.016$ (Planck Collaboration XIII, 2016, §3.4) and `WMAPTT+lensing+BAO` data imply $\tau = 0.066 \pm 0.02$ (Weiland et al., 2018, §5). These constraints are independent of CMB polarization data.

Free streaming of massive neutrinos reduces the amplitude of matter fluctuations at small scales. For testing extensions to ΛCDM, a measurement of τ is necessary to reduce degeneracies between the clustering amplitude at $8\,h^{-1}$ Mpc, the physical cold dark matter density, and the sum of the neutrino masses (σ_8, $\Omega_c h^2$, and $\sum m_\nu$, respectively) (Allison et al., 2015; Liu et al., 2016). The measurement of neutrino masses is especially tantalizing since current upper limits are only a few standard deviations away from the lower limit implied by solar neutrino oscillation measurements (Abazajian et al., 2016).

The relevant polarized foregrounds, thermal dust and synchrotron emission, dominate at large scales with their angular power spectra approximated by power laws $C_\ell^{\rm dust} \propto \ell^{-2.53}$ and $C_\ell^{\rm sync} \propto \ell^{-2.44}$ (Planck Collaboration X, 2016, Table 11, $f_{\rm sky}^{\rm eff} = 0.73$) and are highly anisotropic at large scales, with their minimum in frequency space falling around 70–90 GHz (Krachmalnicoff et al., 2016; Planck Collaboration X, 2016, Fig. 51). This contamination can be mitigated by making high signal-to-noise measurements of the CMB at degree scales and cleaning foregrounds in multipole space, which is the strategy of the ACTPol (Niemack et al., 2010), BICEP (Ade et al., 2015), POLARBEAR (Kermish et al., 2012), and SPTPol (Austermann et al., 2012) experiments. Another approach is to focus on large scale ($\theta \gtrsim 10^\circ$) fluctuations where it is computationally simpler to remove spatially varying foregrounds in map space, an approach that has been employed using maps smoothed to $\theta \sim 15^\circ$ (Bennett et al., 2013; Planck Collaboration XI, 2016). For power spectrum-based analyses, the incomplete sky causes issues both due to E $\rightarrow$ B mixing (caused by spherical harmonics no longer forming a complete orthonormal basis) and the related issue that estimates of the CMB power spectrum $\hat{C}_\ell$ are not drawn from a well-understood statistical distribution. These issues have been addressed by using C_ℓ estimators that can reduce or specifically forbid E $\rightarrow$ B mixing (Chon et al., 2004; Smith and Zaldarriaga, 2007, respectively), and the development of approximate likelihoods that include any potential mixing effects explicitly (Hamimeche and Lewis, 2008; Mangilli, Plaszczynski, and Tristram, 2015).

Watts et al. (2015) demonstrated that the CLASS experiment, and other experiments with multifrequency data and large observing area (e.g. LSPE, Aiola et al. 2012, GroundBird, Tajima et al. 2012 and PIPER, Gandilo et al. 2016), will be able

to overcome partial-sky E $\rightarrow$ B-mode mixing and known sources of foreground contamination by using an exact pixel-based likelihood for low-resolution measurements and a pseudo-C_ℓ likelihood for higher-resolution measurements. In this paper we address mode mixing by fitting the model to the data using a pseudo-C_ℓ estimate from `PolSpice` (Chon et al., 2004) and fitting the data to theory using the approximate Wishart distribution described in Hamimeche and Lewis (2008).

Another major obstacle to characterizing large angular scales is mitigating systematic effects due to observations made on long timescales due to instrumental variations. To reach the necessary instrumental stability, a front-end modulator in the form of a variable-delay polarization modulator (VPM, Chuss et al., 2012) is used as the first optical element of each CLASS telescope (Eimer et al., 2012). This reduces instrumental effects well below the amplitude of an $r = 0.01$ signal (Miller et al., 2016).

This paper expands on Watts et al. (2015) by characterizing the estimated power spectrum across the entire angular range ($2 \leqslant \ell \leqslant 100$) while simultaneously constraining τ, A_s, r, and foreground emission, assuming $1/f$ noise reduction to $r \ll 0.01$ levels using a Variable-delay Polarization Modulator (Miller et al., 2016). In addition to quantifying the expected cosmological parameter constraints from the full CLASS dataset, we also discuss constraints using combinations from external datasets. CLASS will make a sample-variance limited measurement of E-modes on the largest angular scales. With this precise measurement of τ ($\sigma_\tau \sim 0.003$), the CLASS experiment's measurements will break the $A_s e^{-2\tau}$ partial degeneracy found in temperature anisotropy measurements. The resulting improved constraint on A_s enables tighter bounds on the sum of neutrino masses $\sum m_\nu$.

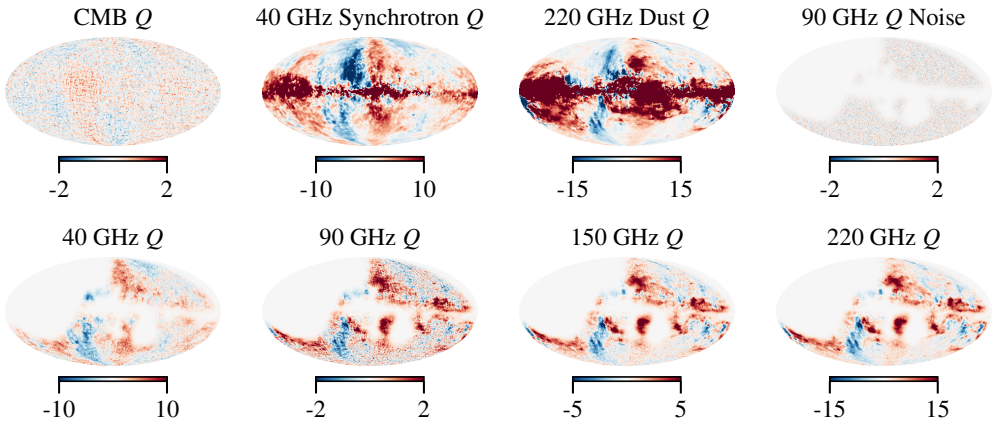

Figure 3.1: The simulated CLASS maps include a realization of the CMB, polarized synchrotron and thermal dust emission, and Gaussian white noise. The top panels show the individual Stokes Q components of the simulation, while the bottom show the simulated multifrequency Stokes Q CLASS maps, with the Galactic plane masked and parts of the celestial Northern Hemisphere and celestial Southern Hemisphere excluded by the survey boundary. All maps are displayed in Galactic coordinates with units of μK.

In section 3.2 we will discuss our simulated data and the assumptions that go into our modeling. section 3.3 introduces our implementation of the Hamimeche and Lewis (2008) pseudo-C_ℓ likelihood and its efficacy at providing constraints given the simulated data. section 3.4 discusses the implications of a CLASS τ measurement in the context of external cosmological parameter constraints. Unless noted otherwise, all cosmological parameters are those listed in Planck Collaboration Int. XLVII (2016), specifically `PlanckTTTEEE+SIMlow`.

3.2 Simulated Maps

We use the CLASS instrument and survey specifications for our simulated data as enumerated in Essinger-Hileman et al. (2014). The CLASS experiment is located in the Atacama Desert in Chile, at a latitude of $-23°$, scanning 70% of the sky

every day at 45° elevation. We combine a mask due to the survey geometry with the *WMAP* P06 Galactic foreground mask, which cuts out the brightest 25% of the sky (Page et al., 2007). This leaves CLASS with an observed sky fraction of $f_{\rm sky} = 0.47$. The CLASS frequency bands are chosen to minimize atmospheric emission while straddling the Galactic foreground minimum. Assuming a 5-year survey with 40, 90, 150, and 220 GHz channels, the maps are assigned weights per pixel $w_{p,\nu}$, corresponding to white noise levels $w_{p,\nu}^{-1/2} = [39, 10, 15, 43]\,\mu$K arcmin. We use this to simulate maps of white noise as draws of a Gaussian random variable $\boldsymbol{n}^\nu \sim \mathcal{N}(\mathbf{0}, \sigma_\nu^2 \mathbf{I})$ with $\sigma_\nu = w_{p,\nu}^{-1/2}/\sqrt{\Omega_{\rm pix}}$, where $\Omega_{\rm pix}$ is the area of a `HEALPix` pixel at the simulated resolution, here $N_{\rm side} = 128$[1].

We simulate foreground emission using `PySM` (Thorne et al., 2017)[2], which takes into account polarized foreground measurements from *Planck* and *WMAP* (polarized dust from Planck Collaboration X 2016, polarized synchrotron from Bennett et al. 2013). While it is known that the emission laws of these foregrounds vary across the sky, with antenna temperature emission parametrized as

$$\begin{aligned} \boldsymbol{m}_{\rm sync}^\nu &= \boldsymbol{m}_{\rm sync} \left(\frac{\nu}{\nu_{\rm S}}\right)^{\beta_{\rm S}(\hat{\boldsymbol{n}})} \\ \boldsymbol{m}_{\rm dust}^\nu &= \boldsymbol{m}_{\rm dust} \left(\frac{\nu}{\nu_{\rm D}}\right)^{\beta_{\rm D}(\hat{\boldsymbol{n}})-2} \frac{B_\nu\left[T_{\rm D}(\hat{\boldsymbol{n}})\right]}{B_{\nu_{\rm D}}\left[T_{\rm D}(\hat{\boldsymbol{n}})\right]}, \end{aligned} \tag{3.2}$$

current data do not yet meaningfully constrain the spatial variation of spectral indices within our sky cut (Watts et al. 2015 Appendix B, Sheehy and Slosar 2017, Planck Collaboration et al. 2018). Therefore we model foreground emission with fixed (i.e., isotropic) synchrotron spectral index $\beta_{\rm S}$, dust spectral index $\beta_{\rm D}$, and blackbody

[1] `HEALPix` (Górski et al., 2005) maps are divided into $12N_{\rm side}^2$ pixels, with each pixel width $\theta_{\rm pix} \sim 58.6°/N_{\rm side}$. The full documentation can be found at `http://healpix.sourceforge.net`.

[2] `https://github.com/bthorne93/PySM_public`

emission $B_\nu[T_\mathrm{D}]$ with dust temperature T_D. Here we use $\nu_\mathrm{S} = 40\,\mathrm{GHz}$ and $\nu_\mathrm{D} = 220\,\mathrm{GHz}$ as the reference frequencies, with $\boldsymbol{m}_\mathrm{sync}$ and $\boldsymbol{m}_\mathrm{dust}$ the synchrotron and dust emission at these respective frequencies. The typical levels for these parameters are $\beta_\mathrm{S} \sim -3.0 \pm 0.1$ (Fuskeland et al., 2014, *WMAP* intensity measurements), $\beta_\mathrm{D} \sim 1.6 \pm 0.1$ (Planck Collaboration Int. L, 2017, *Planck* polarization measurements), and $T_\mathrm{D} \sim 22 \pm 8\,\mathrm{K}$ (Planck Collaboration X, 2016, *Planck* intensity measurements). While varying foreground emission laws are a significant source of bias for B-mode measurements, E-modes are much brighter and are largely unaffected by this source of uncertainty. Additionally, we addressed this complication in Watts et al. (2015) by splitting the sky up into sub-regions with constant emission parameters and showed that a 95% C.L. measurement of $r = 0.01$ was still possible. We have performed several simulations using the levels of spectral index variation in Thorne et al. (2017) ($\Delta\beta_\mathrm{D} < 0.1$, $\Delta\beta_\mathrm{S} \sim 0.1$) and found shifts in the recovery of τ on the order of $\lesssim 0.5\sigma_\tau$. These simulations used a single set of foreground maps that assumed instrumental white noise. For this work we use $\beta_\mathrm{D} = 1.6$ and $\beta_\mathrm{S} = -3$ fixed across the sky.

For the CMB signal, we use the `CAMB` package (Lewis, Challinor, and Lasenby, 2000)[3] to generate theoretical C_ℓ^EE and C_ℓ^BB, keeping all parameters fixed to the `PlanckTTTEEE+SIMlow` Planck Collaboration Int. XLVII (2016) parameters, namely $\tau = 0.0596$ and $\ln(10^{10}A_s) = 3.056$, with the addition of tensor B-modes of amplitude $r = 0.05$. With these theoretical power spectra in hand, we simulate maps using `HEALPix`'s `synfast` function, from which we take the output Q and U Stokes parameters, denoted by the vector $\boldsymbol{m}_\mathrm{CMB}$.

The CLASS 40, 90, 150, and 220 GHz bands have beam full width half maxima

[3] http://camb.info

(FWHMs) of 90, 40, 24, and 18 arcmin respectively, but for the purposes of this study we simulate the maps with a common resolution of 1.5°. We bring all of the foregrounds and CMB to this common resolution $\theta_{\rm FWHM} = 1.5°$, and model the Gaussian noise as uncorrelated between pixels.

The data are from our multifrequency simulations

$$\boldsymbol{m}^{\nu} = g(\nu)\boldsymbol{m}^{\nu}_{\rm sync} + g(\nu)\boldsymbol{m}^{\nu}_{\rm dust} + \boldsymbol{m}_{\rm CMB} + \boldsymbol{n}^{\nu}, \tag{3.3}$$

where $g(\nu) \equiv \partial T/\partial T_A = (e^x - 1)^2/(x^2 e^x)$ is the conversion factor from antenna to thermodynamic temperature referenced to the CMB radiation, with $x \equiv h\nu/kT_{\rm CMB} = \nu/(56.78\,{\rm GHz})$, and $\boldsymbol{m}^{\nu}_{\rm sync/dust}$ as defined in Equation 3.2. A single realization of the CLASS Stokes Q maps using this prescription is shown in Figure 3.1.

3.3 Analysis Techniques

For the CLASS experiment, E-modes are far into the signal-dominated regime, with the main impediment to CMB characterization being the Galactic foreground emission (assuming all systematic measurement errors are under control). To estimate the linearly polarized Stokes parameters of the CMB maps and their polarized power spectra $C_\ell^{\rm EE}$ and $C_\ell^{\rm BB}$, we take linear combinations of the multifrequency maps constrained to keep the CMB amplitude consistent with blackbody emission,

$$\hat{\boldsymbol{m}}_{\rm CMB} \equiv \sum_\nu c_\nu \boldsymbol{m}^{\nu}, \qquad \sum_\nu c_\nu = 1. \tag{3.4}$$

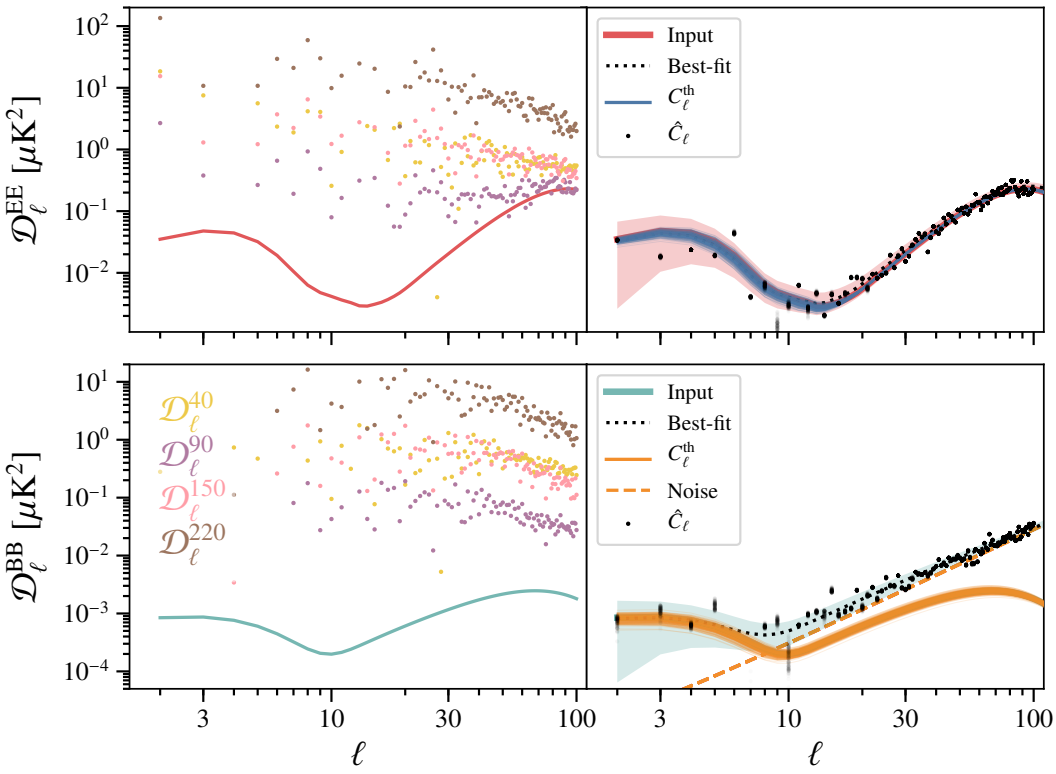

Figure 3.2: Left: The points labeled $\mathcal{D}_\ell^\nu \equiv \ell(\ell+1)C_\ell^\nu/2\pi$ are the autospectra associated with each CLASS band. The amplitudes of these spectra depend both on the foreground amplitudes and the inherent noise bias in auto-spectra. In our likelihood we include these auto-spectra and the cross-spectra (not plotted) and recover the input model (solid lines) by taking linear combinations of these sixteen spectra. Note that the theoretical curves have been smoothed with a 1.5° Gaussian window function. The B-mode spectrum includes contributions from primordial gravitational waves and gravitational lensing, the latter of which is sub-dominant for our fiducial value of $r = 0.05$, but is dominant at the recombination peak when $r \lesssim 0.01$. **Right:** This is a representation of the constraining power of CLASS in pseudo-C_ℓ space with each point and line an independent draw from the MCMC chain. The transparent overlapping gray dots ($\hat{C}_\ell$) represent estimates of the best-fit foreground-cleaned power spectrum $\sum_{\nu_1,\nu_2} c_{\nu_1} c_{\nu_2} \hat{C}_\ell^{\nu_1\times\nu_2}$ (with darker dots being many overlapping gray dots), the thin lines ($C_\ell^{\rm th}$) represent theory curves that were drawn from the chain, and the thick solid lines (Input) the input theory power spectra. The white noise level (Noise) is plotted as an orange dashed line, and the best-fit Theory + Noise power spectrum is plotted as the black dotted line. The expected error is represented by the transparent red and blue swaths, and is given in terms of the input theory spectrum and the best-fit noise, $\sigma_\ell = \sqrt{\frac{2}{(2\ell+1)f_{\rm sky}}}[C_\ell + N_\ell(c_\nu)]$. The input $r = 0.05$, $\log 10^{10} A_s = 3.046$, and $\tau = 0.0596$, are all recovered within 95% confidence levels.

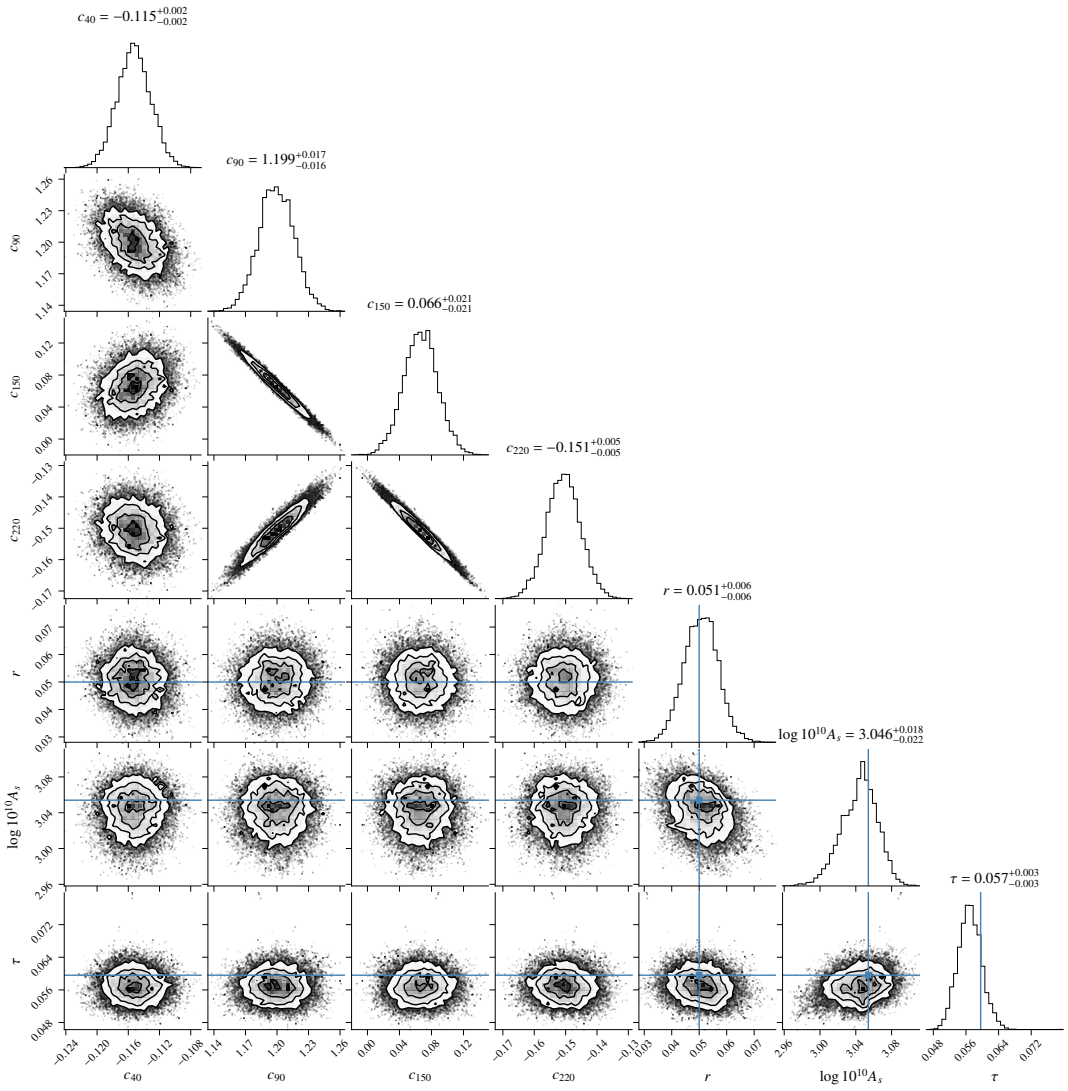

Figure 3.3: Monte Carlo Chain for a single simulation. All parameter fluctuations are representative of the spread found in our suite of simulations. The $\sim 1\sigma$ offset in τ is not unexpected for this single realization. An accurate and unbiased τ results from many simulations. The medians and their asymmetric 68% confidence levels are quoted above each one-dimensional histogram. The cosmological parameters are uncorrelated with the linear combination coefficients c_ν, implying that any residual foregrounds do not affect parameter constraints.

We ensure that the coefficients c_ν reduce foregrounds by imposing Gaussian priors

$$\sum_\nu c_\nu g(\nu) \left(\frac{\nu}{\nu_{\rm S}}\right)^{\beta_{\rm S}} = 0 \pm 0.01 \tag{3.5}$$

$$\sum_\nu c_\nu g(\nu) \left(\frac{\nu}{\nu_{\rm D}}\right)^{\beta_{\rm D}-2} \frac{B_\nu\left[T_{\rm D}\right]}{B_{\nu_{\rm D}}\left[T_{\rm D}\right]} = 0 \pm 0.01, \tag{3.6}$$

corresponding to priors on $\Delta\beta_{\rm S/D} < 0.1$. This prior downweights unphysical solutions corresponding to values of $\beta_{\rm S/D}$ that are ruled out by existing data. This prior is relatively weak compared to the constraining power of the experiment, which returns constraints corresponding to $\Delta\beta_{\rm S} = 0.02$ and $\Delta\beta_{\rm D} = 0.005$. If the c_ν are chosen such that there are no foreground residuals while the instrumental noise contribution is minimized, the resulting power spectrum estimate will be given by

$$\hat{C}_\ell^{\rm EE/BB} = C_\ell^{\rm EE/BB} + \sum_\nu c_\nu^2 N_\ell^\nu. \tag{3.7}$$

where $N_\ell^\nu = w_{p,\nu}^{-1}$, in units of $\mu{\rm K}^2$ sr.

For our purposes, the foreground coefficients c_ν are nuisance parameters that are marginalized over, while the true parameters of interest are r, τ, and A_s. To account for any spurious correlations between foregrounds and CMB fluctuations, we simultaneously fit for the foreground coefficients and the cosmological parameters. Given the power spectrum estimate $\hat{C}_\ell(c_\nu)$, the noise power spectrum $N_\ell = \sum_\nu c_\nu^2 N_\ell^\nu$, and the theoretical power spectrum $C_\ell(r, A_s, \tau)$, the cut-sky likelihood for the power

spectra $C_\ell^{\mathrm{EE/BB}}$ is given by minimizing

$$-2\ln\mathcal{L} \simeq \sum_{\ell\ell'}\left[G\left(\frac{\hat{C}_\ell}{C_\ell+N_\ell}\right)C_{f\ell}\right][M_f^{-1}]_{\ell\ell'}\left[C_{f\ell'}G\left(\frac{\hat{C}_{\ell'}}{C_{\ell'}+N_{\ell'}}\right)\right] + 2\sum_\ell \ln|\hat{C}_\ell| \tag{3.8}$$

where $G(x) \equiv \sqrt{2(x-\ln x-1)}$. The subscript f refers to some fiducial model, and $\boldsymbol{M}_f$ is the covariance of $\hat{C}_\ell$ evaluated for the fiducial model $C_{f\ell}$ (Equation 50 of Hamimeche and Lewis, 2008, see section A.3 for explanation of final term). We split the covariance matrix into two terms, one with CMB and white noise, and another with foreground residuals, $\boldsymbol{M}_f \equiv \boldsymbol{M}_f^{\mathrm{C+N}} + \boldsymbol{M}_f^{\mathrm{fore}}$. We estimate $\boldsymbol{M}_f^{\mathrm{C+N}}$ using simulated data on a cut sky with only CMB and Gaussian white noise contributions, using $r = 0.05$, $\ln(10^{10}A_s) = 3.056$, $\tau = 0.0596$, and $w_p^{-1/2} = 14\,\mu$K arcmin as the fiducial model parameters. The estimated covariance matrix has $M^{\mathrm{C+N}}_{f,(\ell,\ell+1)}/M^{\mathrm{C+N}}_{f,(\ell,\ell)} \lesssim 0.1$, with most values < 0.03 at the 68% C.L. The diagonal elements $M^{\mathrm{C+N}}_{f,\ell\ell}$ agree with the analytical prediction from Chon et al. (2004) at the 5% level,

$$M^{\mathrm{C+N}}_{f,(\ell\ell)} = \frac{2}{(2\ell+1)f_{\mathrm{sky}}w_2^2/w_4}C_\ell^2, \tag{3.9}$$

where $w_n = \int w(\hat{\boldsymbol{n}})^n\,\mathrm{d}\Omega$, $w(\hat{\boldsymbol{n}})$ is the apodized mask, and $f_{\mathrm{sky}} = w_1$ is the observed sky fraction.

The addition of a term $\boldsymbol{M}_f^{\mathrm{fore}}$ accounts for any foreground residuals encountered during the fits. In principle, the best-fit solution does not have any foreground contribution, but any variation around this point in parameter space will affect the best-fit value and will potentially induce spurious correlations. To estimate the effect of foreground residuals, we took the c_ν of a successful MCMC chain without any

foreground covariance accounted for and computed $\hat{C}_\ell$ of foreground residuals taken from multifrequency maps without noise or CMB. This gave a sample covariance matrix $\boldsymbol{M}_f^{\rm fore}$. Using this, we re-computed the Monte Carlo chain using this extra covariance, and found that the recovered cosmological parameters were accurately reconstructed, with an increase in their uncertainty, e.g. for the chain used in Figure 3.2, $\sigma_r = 0.0048 \rightarrow 0.0064$ and $\sigma_\tau = 0.0022 \rightarrow 0.0029$.

We estimate the pseudo-C_ℓ power spectrum using `PolSpice` (Chon et al., 2004), which corrects for the effects of masking and inter-bin correlations induced by the incomplete sky. We represent the estimation of the power spectrum using a bilinear operator P such that $\hat{C}_\ell = \boldsymbol{m}^T \mathsf{P} \boldsymbol{m}$. In practice, we use the bilinear property of this operator to take sums of all multifrequency cross spectra and subtract foregrounds in multipole space, i.e.

$$\hat{C}_\ell = \left(\sum_{\nu_1} c_{\nu_1} \boldsymbol{m}^{\nu_1} \right)^T \mathsf{P} \left(\sum_{\nu_2} c_{\nu_2} \boldsymbol{m}^{\nu_2} \right) = \sum_{\nu_1, \nu_2} c_{\nu_1} c_{\nu_2} \hat{C}_\ell^{\nu_1 \times \nu_2} \tag{3.10}$$

where we have defined $\hat{C}_\ell^{a\times b} \equiv (\boldsymbol{m}^a)^T \mathsf{P} \boldsymbol{m}^b$.

The method outlined here reduces and accounts for any E $\rightarrow$ B mixing inherent in the analysis of an incomplete sky while accounting for the underlying statistical distribution of the power spectrum. `PolSpice` returns a decoupled estimate of the polarization power spectra, giving an unbiased estimate of the true underlying power spectrum while minimizing spurious correlations between E-modes and B-modes. The approximate Wishart distribution from Hamimeche and Lewis (2008) accounts for the non-Gaussian nature of the low-ℓ power spectra while explicitly accounting for any residual E-B correlation in the fiducial covariance matrix $\boldsymbol{M}_f$.

Because calls to `CAMB` are computationally expensive, with each call taking

$O(1\,\mathrm{sec})$, we have written a code `clee-fast`[4] that linearly interpolates between pre-computed power spectra, only allowing variation in r, A_s, and τ. This is similar in spirit to `PICO` (Fendt and Wandelt, 2007), but works better for our purposes because it only allows variation of three parameters, reducing numerical noise and computational cost. Examples of the approximated theory curves and pseudo-C_ℓ estimates are displayed in Figure 3.2, and the corresponding corner plot of the parameter chain is displayed in Figure 3.3.

3.4 Predicting parameter constraints

We obtain sample variance-limited constraints that are on the order of $\sigma_\tau/\tau \sim 5\%$. This is a factor of ~ 3 improvement on the *Planck* precision of $\sigma_\tau/\tau \sim 16\%$, and is a factor of two away from the full-sky cosmic variance precision, $\sigma_\tau/\tau \sim 2.5\%$. We note that there exists a publicly available code, `cmb4cast` (Errard et al., 2016), that uses Fisher matrix analyses to make similar projections. This code gives $\sigma_\tau = 0.0035$, slightly larger than our $\sigma_\tau = 0.0029$. This discrepancy comes from a number of different assumptions between the codes, such as the level of foreground variation, priors on foreground variation, and the fiducial cosmological parameters. Despite these differences, it is reassuring that these different approaches yield this level of agreement.

While large-scale polarization measurements are weakly sensitive to variations in A_s, the strong E-mode sensitivity to τ can break the partial degeneracy in the well-constrained parameter combination $A_s e^{-2\tau}$ found in intensity measurements. The amplitude of primordial scalar fluctuations A_s can be used to predict the amplitude of

[4] https://github.com/pqrs6/clee-fast (Watts, 2017)

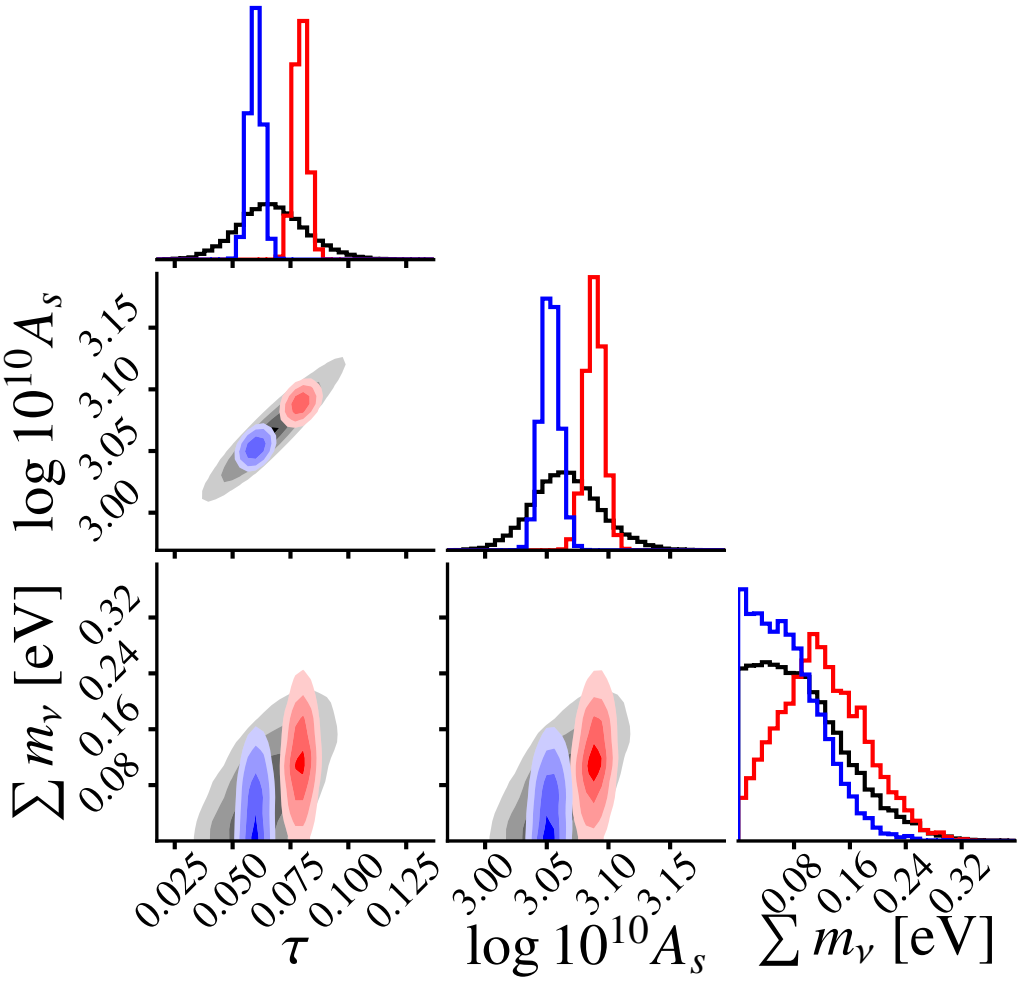

Figure 3.4: Combination with the *Planck* MCMC chains `base_mnu_plikHM_TTTEEE_lowTEB_lensing_BAO`, with CLASS posteriors applied using $\tau = 0.060 \pm 0.003$ (blue) and $\tau = 0.080 \pm 0.003$ (red). These two cases give neutrino mass constraints $\sum m_\nu = 64^{+56}_{-45}$ meV (blue) and $\sum m_\nu = 117 \pm 60$ meV (red). The black contours are from the raw *Planck* chains, and yield constraints $\tau = 0.067^{+0.015}_{-0.014}$ and $\sum m_\nu = 88^{+73}_{-55}$ meV.

matter fluctuations at low redshifts in the linear regime, typically parameterized by the amplitude of dark matter density fluctuations at a scale of $8\,h^{-1}$ Mpc, σ_8.

In standard ΛCDM, there are three neutrino species, and there is experimental evidence that there is a non-zero difference in the squares of each neutrino species' mass, which is detected via the oscillation of neutrinos from one species to another as they travel through space (Athanassopoulos et al., 1998; Abazajian et al., 2015). In the normal hierarchy, the mass of one neutrino is much greater than the other two, which requires that the sum of the neutrino masses $\sum m_\nu > 60\,\mathrm{meV}$. In the inverted hierarchy, two neutrinos have similar masses that are much larger than the third, which requires $\sum m_\nu > 100\,\mathrm{meV}$ (Patrignani, 2016, §14.2).

In the early universe, before neutrinos became non-relativistic matter, massive neutrinos at small scales free streamed, effectively reducing the amplitude of matter fluctuations (Bond and Szalay, 1983; Hu and Sugiyama, 1996). In this way the neutrino mass affects the cosmological model's prediction for σ_8 given A_s. This effect can be used to constrain the mass of neutrinos from above, with current upper limits $\sum m_\nu < 170\,\mathrm{meV}$ at the 95% C.L. using *Planck* temperature and low-ℓ polarization measurements, in combination with BOSS DR12 BAO data and the JLA Type Ia SNe catalog (Couchot et al., 2017). Tighter constraints on σ_8 should improve these limits, although the latest results from the Dark Energy Survey (DES, DES Collaboration et al., 2017) using galaxy clustering and weak lensing show that adding these data to the *Planck*+JLA+BAO data actually increases the 95% C.L. by 20%, which can be attributed to the tension in the values of σ_8 inferred by *Planck* and DES. There is enough uncertainty in A_s, mainly due to the partial degeneracy in $A_s e^{-2\tau}$, to weaken any $\sum m_\nu$ measurement to the $\sim 2\sigma$ level for the minimal $\sum m_\nu = 60\,\mathrm{meV}$ scenario

allowed by neutrino oscillations.

Allison et al. (2015) use Fisher forecasts of future measurements to predict the constraints from combining low-ℓ polarization measurements with Dark Energy Spectroscopic Instrument (DESI) and CMB-S4. In particular, using $\ell_{\rm min} = 50$ for CMB-S4 yields $\sigma_{\sum m_\nu} \sim 27$ meV with only *WMAP* low-ℓ polarization data, and 19 meV, using pre-2016 *Planck* low-ℓ polarization sensitivities. These upper limits are inflated by uncertainty in A_s from the partial degeneracy with τ. Therefore, an external constraint on τ can break this degeneracy, allowing for any differences between the A_s prediction of σ_8 and the measured value of σ_8 to be directly and precisely computed. In the case of putative CMB-S4 measurements with $\ell_{\rm min} = 5$, $\sigma_{\sum m_\nu}$ is reduced to 15 meV, with the reduction in uncertainty coming almost entirely from the uncertainty on τ reducing to $\sigma_\tau = 0.003$. As we have shown, if CLASS is able to measure $C_\ell^{\rm EE}$ and $C_\ell^{\rm BB}$ down to $\ell = 2$ with white noise, it will achieve this σ_τ. In Figure 3.4, using *Planck* MCMC chains from the 2015 data release[5], we show how a CLASS τ measurement would improve constraints on $\sigma_{\sum m_\nu}$ with currently available data.

3.5 Conclusions

We have implemented a $\hat{C}_\ell$-based likelihood for large-scale polarized CMB measurements in the presence of polarized foregrounds and instrumental noise measured on a partial sky. To do this, we implemented a fast interpolation scheme for retrieving $C_\ell(r, A_{\rm s}, \tau)$, and used `PolSpice` to develop a pseudo-C_ℓ likelihood that takes into account mode coupling from a cut-sky analysis.

[5] `COM_CosmoParams_fullGrid_R2.00.tar.gz` from the *Planck* Legacy Archive https://pla.esac.esa.int/pla/

1. We recover the input reionization optical depth with $\sigma_\tau \sim 0.003$, within a factor of two of the cosmic variance limited case.

2. We recover the tensor-to-scalar ratio with $\sigma_r \sim 0.006$, consistent with our partial pixel-based method in Watts et al. (2015).

3. We demonstrate the power of a τ prior on massive neutrino constraints $\sum m_\nu$ using *Planck* Monte Carlo chains.

The CLASS experiment was designed to characterize the large scale polarized CMB up to a sensitivity that allows a 2σ measurement of primordial gravitational waves with an amplitude of $r = 0.01$. As we have demonstrated, satisfying this requirement by measuring C_ℓ^{EE} and C_ℓ^{BB} down to $\ell = 2$ necessarily yields an estimate of the reionization optical depth τ that is limited only by sample variance, and cannot be meaningfully improved upon using measurements of the CMB alone. CLASS's τ constraint will be critical in characterizing neutrino mass, helping to fulfill a major objective in both the particle physics and cosmology communities.

References

Bennett, C. L., D. Larson, J. L. Weiland, N. Jarosik, G. Hinshaw, N. Odegard, K. M. Smith, R. S. Hill, B. Gold, M. Halpern, E. Komatsu, M. R. Nolta, L. Page, D. N. Spergel, E. Wollack, J. Dunkley, A. Kogut, M. Limon, S. S. Meyer, G. S. Tucker, and E. L. Wright (2013). "Nine-year Wilkinson Microwave Anisotropy Probe (WMAP) Observations: Final Maps and Results". In: ApJS 208, 20, p. 20. DOI: 10.1088/0067-0049/208/2/20. arXiv: 1212.5225.

Planck Collaboration XIII (2016). "Planck 2015 results. XIII. Cosmological parameters". In: A&A 594, A13, A13. DOI: 10.1051/0004-6361/201525830. arXiv: 1502.01589.

Planck Collaboration XI (2016). "Planck 2015 results. XI. CMB power spectra, likelihoods, and robustness of parameters". In: A&A 594, A11, p. 104. DOI: 10.1051/0004-6361/201526926. arXiv: 1507.02704.

Addison, G. E., Y. Huang, D. J. Watts, C. L. Bennett, M. Halpern, G. Hinshaw, and J. L. Weiland (2016). "Quantifying Discordance in the 2015 Planck CMB Spectrum". In: ApJ 818, 132, p. 132. DOI: 10.3847/0004-637X/818/2/132. arXiv: 1511.00055.

Hu, W. and T. Okamoto (2004). "Principal power of the CMB". In: Phys. Rev. D 69.4, 043004, p. 043004. DOI: 10.1103/PhysRevD.69.043004. eprint: astro-ph/0308049.

Galli, S., K. Benabed, F. Bouchet, J.-F. Cardoso, F. Elsner, E. Hivon, A. Mangilli, S. Prunet, and B. Wandelt (2014). "CMB polarization can constrain cosmology better than CMB temperature". In: Phys. Rev. D 90.6, 063504, p. 063504. DOI: 10.1103/PhysRevD.90.063504. arXiv: 1403.5271.

Louis, T., E. Grace, M. Hasselfield, M. Lungu, L. Maurin, G. E. Addison, P. A. R. Ade, S. Aiola, R. Allison, M. Amiri, E. Angile, N. Battaglia, J. A. Beall, F. de Bernardis, J. R. Bond, J. Britton, E. Calabrese, H.-m. Cho, S. K. Choi, K. Coughlin, D. Crichton, K. Crowley, R. Datta, M. J. Devlin, S. R. Dicker, J. Dunkley, R. Dünner, S. Ferraro, A. E. Fox, P. Gallardo, M. Gralla, M. Halpern, S. Henderson, J. C. Hill, G. C. Hilton, M. Hilton, A. D. Hincks, R. Hlozek, S. P. P.

Ho, Z. Huang, J. Hubmayr, K. M. Huffenberger, J. P. Hughes, L. Infante, K. Irwin, S. Muya Kasanda, J. Klein, B. Koopman, A. Kosowsky, D. Li, M. Madhavacheril, T. A. Marriage, J. McMahon, F. Menanteau, K. Moodley, C. Munson, S. Naess, F. Nati, L. Newburgh, J. Nibarger, M. D. Niemack, M. R. Nolta, C. Nuñez, L. A. Page, C. Pappas, B. Partridge, F. Rojas, E. Schaan, B. L. Schmitt, N. Sehgal, B. D. Sherwin, J. Sievers, S. Simon, D. N. Spergel, S. T. Staggs, E. R. Switzer, R. Thornton, H. Trac, J. Treu, C. Tucker, A. Van Engelen, J. T. Ward, and E. J. Wollack (2017). "The Atacama Cosmology Telescope: two-season ACTPol spectra and parameters". In: J. Cosmology Astropart. Phys. 6, 031, p. 031. DOI: 10.1088/1475-7516/2017/06/031. arXiv: 1610.02360.

Henning, J. W., J. T. Sayre, C. L. Reichardt, P. A. R. Ade, A. J. Anderson, J. E. Austermann, J. A. Beall, A. N. Bender, B. A. Benson, L. E. Bleem, J. E. Carlstrom, C. L. Chang, H. C. Chiang, H. Cho, R. Citron, C. Corbett Moran, T. M. Crawford, A. T. Crites, T. de Haan, M. A. Dobbs, W. Everett, J. Gallicchio, E. M. George, A. Gilbert, N. W. Halverson, N. Harrington, G. C. Hilton, G. P. Holder, W. L. Holzapfel, S. Hoover, Z. Hou, J. D. Hrubes, N. Huang, J. Hubmayr, K. D. Irwin, R. Keisler, L. Knox, A. T. Lee, E. M. Leitch, D. Li, A. Lowitz, A. Manzotti, J. J. McMahon, S. S. Meyer, L. Mocanu, J. Montgomery, A. Nadolski, T. Natoli, J. P. Nibarger, V. Novosad, S. Padin, C. Pryke, J. E. Ruhl, B. R. Saliwanchik, K. K. Schaffer, C. Sievers, G. Smecher, A. A. Stark, K. T. Story, C. Tucker, K. Vanderlinde, T. Veach, J. D. Vieira, G. Wang, N. Whitehorn, W. L. K. Wu, and V. Yefremenko (2017). "Measurements of the Temperature and E-Mode Polarization of the CMB from 500 Square Degrees of SPTpol Data". In: *ArXiv e-prints*. arXiv: 1707.09353.

Page, L., G. Hinshaw, E. Komatsu, M. R. Nolta, D. N. Spergel, C. L. Bennett, C. Barnes, R. Bean, O. Doré, J. Dunkley, M. Halpern, R. S. Hill, N. Jarosik, A. Kogut, M. Limon, S. S. Meyer, N. Odegard, H. V. Peiris, G. S. Tucker, L. Verde, J. L. Weiland, E. Wollack, and E. L. Wright (2007). "Three-Year Wilkinson Microwave Anisotropy Probe (WMAP) Observations: Polarization Analysis". In: ApJS 170, pp. 335–376. DOI: 10.1086/513699. eprint: astro-ph/0603450.

Guth, A. H. (1981). "Inflationary universe: A possible solution to the horizon and flatness problems". In: Phys. Rev. D 23, pp. 347–356. DOI: 10.1103/PhysRevD.23.347.

Starobinsky, A. A. (1980). "A new type of isotropic cosmological models without singularity". In: *Physics Letters B* 91, pp. 99–102. DOI: 10.1016/0370-2693(80)90670-X.

Kazanas, D. (1980). "Dynamics of the universe and spontaneous symmetry breaking". In: ApJ 241, pp. L59–L63. DOI: 10.1086/183361.

Mukhanov, V. F. and G. V. Chibisov (1981). "Quantum fluctuations and a nonsingular universe". In: *Soviet Journal of Experimental and Theoretical Physics Letters* 33, p. 532.

Einhorn, M. B. and K. Sato (1981). "Monopole production in the very early universe in a first-order phase transition". In: *Nuclear Physics B* 180, pp. 385–404. DOI: 10.1016/0550-3213(81)90057-2.

Linde, A. D. (1982). "A new inflationary universe scenario: A possible solution of the horizon, flatness, homogeneity, isotropy and primordial monopole problems". In: *Physics Letters B* 108, pp. 389–393. DOI: 10.1016/0370-2693(82)91219-9.

Albrecht, A. and P. J. Steinhardt (1982). "Cosmology for grand unified theories with radiatively induced symmetry breaking". In: *Physical Review Letters* 48, pp. 1220–1223. DOI: 10.1103/PhysRevLett.48.1220.

Kamionkowski, M., A. Kosowsky, and A. Stebbins (1997). "Statistics of cosmic microwave background polarization". In: Phys. Rev. D 55, pp. 7368–7388. DOI: 10.1103/PhysRevD.55.7368. eprint: astro-ph/9611125.

Seljak, U. and M. Zaldarriaga (1997). "Signature of Gravity Waves in the Polarization of the Microwave Background". In: *Physical Review Letters* 78, pp. 2054–2057. DOI: 10.1103/PhysRevLett.78.2054. eprint: astro-ph/9609169.

Eimer, J. R., C. L. Bennett, D. T. Chuss, T. Marriage, E. J. Wollack, and L. Zeng (2012). "The cosmology large angular scale surveyor (CLASS): 40 GHz optical design". In: *Society of Photo-Optical Instrumentation Engineers (SPIE) Conference Series*. Vol. 8452. Society of Photo-Optical Instrumentation Engineers (SPIE) Conference Series. DOI: 10.1117/12.925464. arXiv: 1211.0041 [astro-ph.IM].

Essinger-Hileman, T., A. Ali, M. Amiri, J. W. Appel, D. Araujo, C. L. Bennett, F. Boone, M. Chan, H.-M. Cho, D. T. Chuss, F. Colazo, E. Crowe, K. Denis, R. Dünner, J. Eimer, D. Gothe, M. Halpern, K. Harrington, G. C. Hilton, G. F. Hinshaw, C. Huang, K. Irwin, G. Jones, J. Karakla, A. J. Kogut, D. Larson, M. Limon, L. Lowry, T. Marriage, N. Mehrle, A. D. Miller, N. Miller, S. H. Moseley, G. Novak, C. Reintsema, K. Rostem, T. Stevenson, D. Towner, K. U-Yen, E. Wagner, D. Watts, E. J. Wollack, Z. Xu, and L. Zeng (2014). "CLASS: the cosmology large angular scale surveyor". In: *Society of Photo-Optical Instrumentation Engineers (SPIE) Conference Series*. Vol. 9153. Society of Photo-Optical Instrumentation Engineers (SPIE) Conference Series. DOI: 10.1117/12.2056701. arXiv: 1408.4788 [astro-ph.IM].

Harrington, K., T. Marriage, A. Ali, J. W. Appel, C. L. Bennett, F. Boone, M. Brewer, M. Chan, D. T. Chuss, F. Colazo, S. Dahal, K. Denis, R. Dünner, J. Eimer, T. Essinger-Hileman, P. Fluxa, M. Halpern, G. Hilton, G. F. Hinshaw, J. Hubmayr, J. Iuliano, J. Karakla, J. McMahon, N. T. Miller, S. H. Moseley, G. Palma, L. Parker,

M. Petroff, B. Pradenas, K. Rostem, M. Sagliocca, D. Valle, D. Watts, E. Wollack, Z. Xu, and L. Zeng (2016). "The Cosmology Large Angular Scale Surveyor". In: *Millimeter, Submillimeter, and Far-Infrared Detectors and Instrumentation for Astronomy VIII*. Vol. 9914. Proc. SPIE, 99141K. DOI: 10.1117/12.2233125. arXiv: 1608.08234 [astro-ph.IM].

Heinrich, C. H., V. Miranda, and W. Hu (2017). "Complete reionization constraints from Planck 2015 polarization". In: Phys. Rev. D 95.2, 023513, p. 023513. DOI: 10.1103/PhysRevD.95.023513. arXiv: 1609.04788.

Gunn, J. E. and B. A. Peterson (1965). "On the Density of Neutral Hydrogen in Intergalactic Space." In: ApJ 142, pp. 1633–1641. DOI: 10.1086/148444.

Fan, X., M. A. Strauss, R. H. Becker, R. L. White, J. E. Gunn, G. R. Knapp, G. T. Richards, D. P. Schneider, J. Brinkmann, and M. Fukugita (2006). "Constraining the Evolution of the Ionizing Background and the Epoch of Reionization with z˜6 Quasars. II. A Sample of 19 Quasars". In: AJ 132, pp. 117–136. DOI: 10.1086/504836. eprint: astro-ph/0512082.

Planck Collaboration Int. XLVII (2016). "Planck intermediate results. XLVII. Planck constraints on reionization history". In: A&A 596, A108, A108. DOI: 10.1051/0004-6361/201628897. arXiv: 1605.03507.

Planck Collaboration et al. (2016). "Planck intermediate results. XLVI. Reduction of large-scale systematic effects in HFI polarization maps and estimation of the reionization optical depth". In: A&A 596, A107, A107. DOI: 10.1051/0004-6361/201628890. arXiv: 1605.02985.

Weiland, J. L., K. Osumi, G. E. Addison, C. L. Bennett, D. J. Watts, M. Halpern, and G. Hinshaw (2018). "Effect of Template Uncertainties on the WMAP and Planck Measures of the Optical Depth Due To Reionization". In: *ArXiv e-prints*. arXiv: 1801.01226.

Allison, R., P. Caucal, E. Calabrese, J. Dunkley, and T. Louis (2015). "Towards a cosmological neutrino mass detection". In: Phys. Rev. D 92.12, 123535, p. 123535. DOI: 10.1103/PhysRevD.92.123535. arXiv: 1509.07471.

Liu, A., J. R. Pritchard, R. Allison, A. R. Parsons, U. Seljak, and B. D. Sherwin (2016). "Eliminating the optical depth nuisance from the CMB with 21 cm cosmology". In: Phys. Rev. D 93.4, 043013, p. 043013. DOI: 10.1103/PhysRevD.93.043013. arXiv: 1509.08463.

Abazajian, Kevork N., Peter Adshead, Zeeshan Ahmed, Steven W. Allen, David Alonso, Kam S. Arnold, Carlo Baccigalupi, James G. Bartlett, Nicholas Battaglia, Bradford A. Benson, Colin A. Bischoff, Julian Borrill, Victor Buza, Erminia Calabrese, Robert Caldwell, John E. Carlstrom, Clarence L. Chang, Thomas M. Crawford, Francis-Yan Cyr-Racine, Francesco De Bernardis, Tijmen de Haan,

Sperello di Serego Alighieri, Joanna Dunkley, Cora Dvorkin, Josquin Errard, Giulio Fabbian, Stephen Feeney, Simone Ferraro, Jeffrey P. Filippini, Raphael Flauger, George M. Fuller, Vera Gluscevic, Daniel Green, Daniel Grin, Evan Grohs, Jason W. Henning, J. Colin Hill, Renee Hlozek, Gilbert Holder, William Holzapfel, Wayne Hu, Kevin M. Huffenberger, Reijo Keskitalo, Lloyd Knox, Arthur Kosowsky, John Kovac, Ely D. Kovetz, Chao-Lin Kuo, Akito Kusaka, Maude Le Jeune, Adrian T. Lee, Marc Lilley, Marilena Loverde, Mathew S. Madhavacheril, Adam Mantz, David J. E. Marsh, Jeffrey McMahon, Pieter Daniel Meerburg, Joel Meyers, Amber D. Miller, Julian B. Munoz, Ho Nam Nguyen, Michael D. Niemack, Marco Peloso, Julien Peloton, Levon Pogosian, Clement Pryke, Marco Raveri, Christian L. Reichardt, Graca Rocha, Aditya Rotti, Emmanuel Schaan, Marcel M. Schmittfull, Douglas Scott, Neelima Sehgal, Sarah Shandera, Blake D. Sherwin, Tristan L. Smith, Lorenzo Sorbo, Glenn D. Starkman, Kyle T. Story, Alexander van Engelen, Joaquin D. Vieira, Scott Watson, Nathan Whitehorn, and W. L. Kimmy Wu (2016). "CMB-S4 Science Book, First Edition". In: DOI: Abazajian,K.N.,Adshead,P.,Ahmed,Z.,Allen,S.W.,Alonso,D.,Arnold,K.S.,âĂęWu,W.L.K.(2016).CMB-S4ScienceBook,FirstEdition.Retrievedfromhttp://arxiv.org/abs/1610.02743. arXiv: 1610.02743. URL: http://arxiv.org/abs/1610.02743.

Planck Collaboration X (2016). "Planck 2015 results. X. Diffuse component separation: Foreground maps". In: A&A 594, A10, A10. DOI: 10.1051/0004-6361/201525967. arXiv: 1502.01588.

Krachmalnicoff, N., C. Baccigalupi, J. Aumont, M. Bersanelli, and A. Mennella (2016). "Characterization of foreground emission on degree angular scales for CMB B-mode observations . Thermal dust and synchrotron signal from Planck and WMAP data". In: A&A 588, A65, A65. DOI: 10.1051/0004-6361/201527678. arXiv: 1511.00532.

Niemack, M. D., P. A. R. Ade, J. Aguirre, F. Barrientos, J. A. Beall, J. R. Bond, J. Britton, H. M. Cho, S. Das, M. J. Devlin, S. Dicker, J. Dunkley, R. Dünner, J. W. Fowler, A. Hajian, M. Halpern, M. Hasselfield, G. C. Hilton, M. Hilton, J. Hubmayr, J. P. Hughes, L. Infante, K. D. Irwin, N. Jarosik, J. Klein, A. Kosowsky, T. A. Marriage, J. McMahon, F. Menanteau, K. Moodley, J. P. Nibarger, M. R. Nolta, L. A. Page, B. Partridge, E. D. Reese, J. Sievers, D. N. Spergel, S. T. Staggs, R. Thornton, C. Tucker, E. Wollack, and K. W. Yoon (2010). "ACTPol: a polarization-sensitive receiver for the Atacama Cosmology Telescope". In: *Society of Photo-Optical Instrumentation Engineers (SPIE) Conference Series*. Vol. 7741. Society of Photo-Optical Instrumentation Engineers (SPIE) Conference Series. DOI: 10.1117/12.857464. arXiv: 1006.5049 [astro-ph.IM].

Ade, P A R, Z Ahmed, R W Aikin, K D Alexander, D Barkats, S J Benton, C A Bischoff, J J Bock, J A Brevik, I Buder, E Bullock, V Buza, J Connors, B P Crill, C D Dowell, C Dvorkin, L Duband, J P Filippini, S Fliescher, S R Golwala, M Halpern, S Harrison, M Hasselfield, S R Hildebrandt, G C Hilton, V V Hristov, H Hui, K D Irwin, K S Karkare, J P Kaufman, B G Keating, S Kefeli, S A Kernasovskiy, J M Kovac, C L Kuo, E M Leitch, M Lueker, P Mason, K G Megerian, C B Netterfield, H T Nguyen, R O 'brient, R W Ogburn Iv, A Orlando, C Pryke, C D Reintsema, S Richter, R Schwarz, C D Sheehy, Z K Staniszewski, R V Sudiwala, G P Teply, K L Thompson, J E Tolan, A D Turner, A G Vieregg, A C Weber, J Willmert, C L Wong, and K W Yoon (2015). "BICEP2/KECK ARRAY V: MEASUREMENTS OF B-MODE POLARIZATION AT DEGREE ANGULAR SCALES AND 150 GHz BY THE KECK ARRAY". In: *The Astrophysical Journal* 811, p. 126. DOI: 10.1088/0004-637X/811/2/126.

Kermish, Z. D., P. Ade, A. Anthony, K. Arnold, D. Barron, D. Boettger, J. Borrill, S. Chapman, Y. Chinone, M. A. Dobbs, J. Errard, G. Fabbian, D. Flanigan, G. Fuller, A. Ghribi, W. Grainger, N. Halverson, M. Hasegawa, K. Hattori, M. Hazumi, W. L. Holzapfel, J. Howard, P. Hyland, A. Jaffe, B. Keating, T. Kisner, A. T. Lee, M. Le Jeune, E. Linder, M. Lungu, F. Matsuda, T. Matsumura, X. Meng, N. J. Miller, H. Morii, S. Moyerman, M. J. Myers, H. Nishino, H. Paar, E. Quealy, C. L. Reichardt, P. L. Richards, C. Ross, A. Shimizu, M. Shimon, C. Shimmin, M. Sholl, P. Siritanasak, H. Spieler, N. Stebor, B. Steinbach, R. Stompor, A. Suzuki, T. Tomaru, C. Tucker, and O. Zahn (2012). "The POLARBEAR experiment". In: *Society of Photo-Optical Instrumentation Engineers (SPIE) Conference Series*. Vol. 8452. Society of Photo-Optical Instrumentation Engineers (SPIE) Conference Series. DOI: 10.1117/12.926354. arXiv: 1210.7768 [astro-ph.IM].

Austermann, J. E., K. A. Aird, J. A. Beall, D. Becker, A. Bender, B. A. Benson, L. E. Bleem, J. Britton, J. E. Carlstrom, C. L. Chang, H. C. Chiang, H.-M. Cho, T. M. Crawford, A. T. Crites, A. Datesman, T. de Haan, M. A. Dobbs, E. M. George, N. W. Halverson, N. Harrington, J. W. Henning, G. C. Hilton, G. P. Holder, W. L. Holzapfel, S. Hoover, N. Huang, J. Hubmayr, K. D. Irwin, R. Keisler, J. Kennedy, L. Knox, A. T. Lee, E. Leitch, D. Li, M. Lueker, D. P. Marrone, J. J. McMahon, J. Mehl, S. S. Meyer, T. E. Montroy, T. Natoli, J. P. Nibarger, M. D. Niemack, V. Novosad, S. Padin, C. Pryke, C. L. Reichardt, J. E. Ruhl, B. R. Saliwanchik, J. T. Sayre, K. K. Schaffer, E. Shirokoff, A. A. Stark, K. Story, K. Vanderlinde, J. D. Vieira, G. Wang, R. Williamson, V. Yefremenko, K. W. Yoon, and O. Zahn (2012). "SPTpol: an instrument for CMB polarization measurements with the South Pole Telescope". In: *Society of Photo-Optical Instrumentation Engineers (SPIE) Conference Series*. Vol. 8452. Society of Photo-Optical Instrumentation

Engineers (SPIE) Conference Series. DOI: 10.1117/12.927286. arXiv: 1210.4970 [astro-ph.IM].

Chon, G., A. Challinor, S. Prunet, E. Hivon, and I. Szapudi (2004). "Fast estimation of polarization power spectra using correlation functions". In: MNRAS 350, pp. 914–926. DOI: 10.1111/j.1365-2966.2004.07737.x. eprint: astro-ph/0303414.

Smith, K. M. and M. Zaldarriaga (2007). "General solution to the E-B mixing problem". In: Phys. Rev. D 76.4, 043001, p. 043001. DOI: 10.1103/PhysRevD.76.043001. eprint: astro-ph/0610059.

Hamimeche, S. and A. Lewis (2008). "Likelihood analysis of CMB temperature and polarization power spectra". In: Phys. Rev. D 77.10, 103013, p. 103013. DOI: 10.1103/PhysRevD.77.103013. arXiv: 0801.0554.

Mangilli, A., S. Plaszczynski, and M. Tristram (2015). "Large-scale cosmic microwave background temperature and polarization cross-spectra likelihoods". In: MNRAS 453, pp. 3174–3189. DOI: 10.1093/mnras/stv1733. arXiv: 1503.01347.

Watts, D. J., D. Larson, T. A. Marriage, M. H. Abitbol, J. W. Appel, C. L. Bennett, D. T. Chuss, J. R. Eimer, T. Essinger-Hileman, N. J. Miller, K. Rostem, and E. J. Wollack (2015). "Measuring the Largest Angular Scale CMB B-mode Polarization with Galactic Foregrounds on a Cut Sky". In: ApJ 814, 103, p. 103. DOI: 10.1088/0004-637X/814/2/103. arXiv: 1508.00017.

Aiola, S., G. Amico, P. Battaglia, E. Battistelli, A. Baó, P. de Bernardis, M. Bersanelli, A. Boscaleri, F. Cavaliere, A. Coppolecchia, A. Cruciani, F. Cuttaia, A. D'Addabbo, G. D'Alessandro, S. De Gregori, F. Del Torto, M. De Petris, L. Fiorineschi, C. Franceschet, E. Franceschi, M. Gervasi, D. Goldie, A. Gregorio, V. Haynes, N. Krachmalnicoff, L. Lamagna, B. Maffei, D. Maino, S. Masi, A. Mennella, G. Morgante, F. Nati, M. W. Ng, L. Pagano, A. Passerini, O. Peverini, F. Piacentini, L. Piccirillo, G. Pisano, S. Ricciardi, P. Rissone, G. Romeo, M. Salatino, M. Sandri, A. Schillaci, L. Stringhetti, A. Tartari, R. Tascone, L. Terenzi, M. Tomasi, E. Tommasi, F. Villa, G. Virone, S. Withington, A. Zacchei, and M. Zannoni (2012). "The Large-Scale Polarization Explorer (LSPE)". In: *Society of Photo-Optical Instrumentation Engineers (SPIE) Conference Series*. Vol. 8446. Society of Photo-Optical Instrumentation Engineers (SPIE) Conference Series. DOI: 10.1117/12.926095.

Tajima, O., J. Choi, M. Hazumi, H. Ishitsuka, M. Kawai, and M. Yoshida (2012). "GroundBIRD: an experiment for CMB polarization measurements at a large angular scale from the ground". In: *Society of Photo-Optical Instrumentation*

Engineers (SPIE) Conference Series. Vol. 8452. Society of Photo-Optical Instrumentation Engineers (SPIE) Conference Series. DOI: 10.1117/12.925816.

Gandilo, N. N., P. A. R. Ade, D. Benford, C. L. Bennett, D. T. Chuss, J. L. Dotson, J. R. Eimer, D. J. Fixsen, M. Halpern, G. Hilton, G. F. Hinshaw, K. Irwin, C. Jhabvala, M. Kimball, A. Kogut, L. Lowe, J. J. McMahon, T. M. Miller, P. Mirel, S. H. Moseley, S. Pawlyk, S. Rodriguez, E. Sharp, P. Shirron, J. G. Staguhn, D. F. Sullivan, E. R. Switzer, P. Taraschi, C. E. Tucker, and E. J. Wollack (2016). "The Primordial Inflation Polarization Explorer (PIPER)". In: *Millimeter, Submillimeter, and Far-Infrared Detectors and Instrumentation for Astronomy VIII*. Vol. 9914. Proc. SPIE, 99141J. DOI: 10.1117/12.2231109. arXiv: 1607.06172 [astro-ph.IM].

Chuss, David T., Edward J. Wollack, Ross Henry, Howard Hui, Aaron J. Juarez, Megan Krejny, S. Harvey Moseley, and Giles Novak (2012). "Properties of a variable-delay polarization modulator". In: *Appl. Opt.* 51.2, pp. 197–208. DOI: 10.1364/AO.51.000197. URL: http://ao.osa.org/abstract.cfm?URI=ao-51-2-197.

Miller, N. J., D. T. Chuss, T. A. Marriage, E. J. Wollack, J. W. Appel, C. L. Bennett, J. Eimer, T. Essinger-Hileman, D. J. Fixsen, K. Harrington, S. H. Moseley, K. Rostem, E. R. Switzer, and D. J. Watts (2016). "Recovery of Large Angular Scale CMB Polarization for Instruments Employing Variable-delay Polarization Modulators". In: ApJ 818, 151, p. 151. DOI: 10.3847/0004-637X/818/2/151. arXiv: 1509.04628 [astro-ph.IM].

Górski, K. M., E. Hivon, A. J. Banday, B. D. Wandelt, F. K. Hansen, M. Reinecke, and M. Bartelmann (2005). "HEALPix: A Framework for High-Resolution Discretization and Fast Analysis of Data Distributed on the Sphere". In: ApJ 622, pp. 759–771. DOI: 10.1086/427976. eprint: astro-ph/0409513.

Thorne, B., J. Dunkley, D. Alonso, and S. Næss (2017). "The Python Sky Model: software for simulating the Galactic microwave sky". In: MNRAS 469, pp. 2821–2833. DOI: 10.1093/mnras/stx949. arXiv: 1608.02841.

Sheehy, C. and A. Slosar (2017). "No evidence for dust B-mode decorrelation in Planck data". In: *ArXiv e-prints*. arXiv: 1709.09729.

Planck Collaboration et al. (2018). "Planck intermediate results. LIV. Polarized dust foregrounds". In: *ArXiv e-prints*. arXiv: 1801.04945.

Fuskeland, U., I. K. Wehus, H. K. Eriksen, and S. K. Næss (2014). "Spatial Variations in the Spectral Index of Polarized Synchrotron Emission in the 9yr WMAP Sky Maps". In: ApJ 790, 104, p. 104. DOI: 10.1088/0004-637X/790/2/104. arXiv: 1404.5323.

Planck Collaboration Int. L (2017). "Planck intermediate results. L. Evidence of spatial variation of the polarized thermal dust spectral energy distribution and implications for CMB B-mode analysis". In: A&A 599, A51, A51. DOI: 10.1051/0004-6361/201629164. arXiv: 1606.07335.

Lewis, A., A. Challinor, and A. Lasenby (2000). "Efficient Computation of Cosmic Microwave Background Anisotropies in Closed Friedmann-Robertson-Walker Models". In: ApJ 538, pp. 473–476. DOI: 10.1086/309179. eprint: astro-ph/9911177.

Watts, Duncan Joseph (2017). *clee_fast*. DOI: 10.5281/zenodo.1066547. URL: http://dx.doi.org/10.5281/zenodo.1066547.

Fendt, W. A. and B. D. Wandelt (2007). "Pico: Parameters for the Impatient Cosmologist". In: ApJ 654, pp. 2–11. DOI: 10.1086/508342. eprint: astro-ph/0606709.

Errard, Josquin, Stephen M. Feeney, Hiranya V. Peiris, and Andrew H. Jaffe (2016). "Robust forecasts on fundamental physics from the foreground-obscured, gravitationally-lensed CMB polarization". In: *Journal of Cosmology and Astro-Particle Physics* 2016. DOI: 10.1088/1475-7516/2016/03/052.

Athanassopoulos, C., L. B. Auerbach, R. L. Burman, D. O. Caldwell, E. D. Church, I. Cohen, J. B. Donahue, A. Fazely, F. J. Federspiel, G. T. Garvey, R. M. Gunasingha, R. Imlay, K. Johnston, H. J. Kim, W. C. Louis, R. Majkic, K. McIlhany, G. B. Mills, R. A. Reeder, V. Sandberg, D. Smith, I. Stancu, W. Strossman, R. Tayloe, G. J. VanDalen, W. Vernon, N. Wadia, J. Waltz, D. H. White, D. Works, Y. Xiao, and S. Yellin (1998). "Results on $\nu_\mu \to \nu_e$ Neutrino Oscillations from the LSND Experiment". In: *Phys. Rev. Lett.* 81 (9), pp. 1774–1777. DOI: 10.1103/PhysRevLett.81.1774. URL: https://link.aps.org/doi/10.1103/PhysRevLett.81.1774.

Abazajian, K. N., K. Arnold, J. Austermann, B. A. Benson, C. Bischoff, J. Bock, J. R. Bond, J. Borrill, E. Calabrese, J. E. Carlstrom, C. S. Carvalho, C. L. Chang, H. C. Chiang, S. Church, A. Cooray, T. M. Crawford, K. S. Dawson, S. Das, M. J. Devlin, M. Dobbs, S. Dodelson, O. Doré, J. Dunkley, J. Errard, A. Fraisse, J. Gallicchio, N. W. Halverson, S. Hanany, S. R. Hildebrandt, A. Hincks, R. Hlozek, G. Holder, W. L. Holzapfel, K. Honscheid, W. Hu, J. Hubmayr, K. Irwin, W. C. Jones, M. Kamionkowski, B. Keating, R. Keisler, L. Knox, E. Komatsu, J. Kovac, C.-L. Kuo, C. Lawrence, A. T. Lee, E. Leitch, E. Linder, P. Lubin, J. McMahon, A. Miller, L. Newburgh, M. D. Niemack, H. Nguyen, H. T. Nguyen, L. Page, C. Pryke, C. L. Reichardt, J. E. Ruhl, N. Sehgal, U. Seljak, J. Sievers, E. Silverstein, A. Slosar, K. M. Smith, D. Spergel, S. T. Staggs, A. Stark, R. Stompor, A. G. Vieregg, G. Wang, S. Watson, E. J. Wollack, W. L. K. Wu, K. W. Yoon, and O. Zahn (2015). "Neutrino physics from the cosmic microwave

background and large scale structure". In: *Astroparticle Physics* 63, pp. 66–80. DOI: 10.1016/j.astropartphys.2014.05.014. arXiv: 1309.5383.

Patrignani, C. et al. (2016). "Review of Particle Physics". In: *Chin. Phys.* C40.10, p. 100001. DOI: 10.1088/1674-1137/40/10/100001.

Bond, J. R. and A. S. Szalay (1983). "The collisionless damping of density fluctuations in an expanding universe". In: ApJ 274, pp. 443–468. DOI: 10.1086/161460.

Hu, W. and N. Sugiyama (1996). "Small-Scale Cosmological Perturbations: an Analytic Approach". In: ApJ 471, p. 542. DOI: 10.1086/177989. eprint: astro-ph/9510117.

Couchot, F., S. Henrot-Versillé, O. Perdereau, S. Plaszczynski, B. Rouillé d'Orfeuil, M. Spinelli, and M. Tristram (2017). "Cosmological constraints on the neutrino mass including systematic uncertainties". In: A&A 606, A104, A104. DOI: 10.1051/0004-6361/201730927. arXiv: 1703.10829.

DES Collaboration et al. (2017). "Dark Energy Survey Year 1 Results: Cosmological Constraints from Galaxy Clustering and Weak Lensing". In: *ArXiv e-prints*. arXiv: 1708.01530.

Chapter 4

Discussion and Conclusions

The Cosmology Large Angular Scale Surveyor (CLASS) is designed to constrain the physical effects of cosmological inflation by measuring the large scale fluctuations of the polarized cosmic microwave background induced by primordial gravitational waves and the density fluctuations induced during the era of reionization. In order to make these measurements, it is necessary to remove the polarized Galactic synchrotron and thermal dust emission using multifrequency measurements at 40, 90, 150, and 220 GHz. These measurements will enable characterization of the cosmic microwave background fluctuations, and will help provide unique constraints on the reionization optical depth τ and the tensor-to-scalar ratio r.

This thesis summarized the technical aspects of turning multifrequency maps of the sky into cosmological parameter constraints. The methods I described are robust to contamination from Galactic foregrounds and spurious B-modes induced by incomplete sky coverage. We demonstrated that the tensor-to-scalar ratio will be constrained to $r < 0.008$ at the 95% C.L., and the reionization optical depth will be constrained to close to the cosmic variance limit, with $\sigma_\tau = 0.003$. The code developed for this thesis will be the basis for the analysis of the real CLASS maps.

Appendix A

Published Appendices

This appendix includes appendices first published in Watts et al. (2015) (section A.1 and section A.2) and Watts et al. (2018) (section A.3).

A.1 Signal-to-Noise on Large Angular Scales

The purpose of this Appendix is to demonstrate that in the large-noise limit, the signal-to-noise of B-mode polarization measurements increases with decreasing multipole ℓ. Cosmic variance, the uncertainty in the observed CMB anisotropy due to it being a single realization of a Gaussian random field, is a limitation for large scale experiments in particular since the uncertainty in the power spectrum scales as $\ell^{-1/2}$ in the cosmic variance limit. For a beam window function b_ℓ and noise power spectrum N_ℓ, the signal-to-noise per multipole of a power spectrum is (Knox, 1995)

$$\frac{C_\ell b_\ell^2}{(C_\ell b_\ell^2 + N_\ell)\sqrt{\frac{2}{f_{\rm sky}(2\ell+1)}}} = \frac{\sqrt{f_{\rm sky}(\ell+1/2)}}{1 + N_\ell/(C_\ell b_\ell^2)}. \tag{A.1}$$

For $C_\ell b_\ell^2 \gg N_\ell$, i.e. in the cosmic variance limit, the $\ell^{1/2}$ factor dominates the signal-to-noise, but when the power spectra of the noise and CMB are comparable the

relationship is not as simple, and the projected significance can sometimes increase at large angular scales.

CMB polarization experiments are far from the cosmic variance measurement limits of the B-mode power spectrum, so at large angular scales the signal-to-noise in Equation A.1 becomes

$$\frac{C_\ell b_\ell^2 \sqrt{f_{\rm sky}(\ell + 1/2)}}{N_\ell}. \tag{A.2}$$

For low multipoles the BB spectrum roughly scales with multipole as $C_\ell \propto \ell^{-2}$, so that signal-to-noise scales as $\ell^{-3/2}$, in contrast with the $\ell^{1/2}$ scaling found in the cosmic variance limit.

A.2 Dust Spectral Index Variation

The purpose of this Appendix is to demonstrate that the observed variation in dust spectral index observed by *Planck* (Planck Collaboration, 2015) is consistent with noise, and does not indicate any intrinsic variation. To estimate the spectral index of thermal dust emission, the *Planck* team subdivided mid-latitude data into 400 overlapping patches of sky (Planck Collaboration, 2015). They subtracted lower frequency data from dust-dominated bands to remove the achromatic CMB component and then took ratios of the residual at two different frequencies, ν_1 and ν_2, denoted

$$R_{\nu_0}(\nu_2, \nu_1) = \frac{I_{\nu_2} - I_{\nu_0}}{I_{\nu_1} - I_{\nu_0}} \tag{A.3}$$

$$\simeq \left(\frac{\nu_2}{\nu_1}\right)^{\beta_{\rm D}} \frac{B_{\nu_2}(T_{\rm D})}{B_{\nu_1}(T_{\rm D})} \tag{A.4}$$

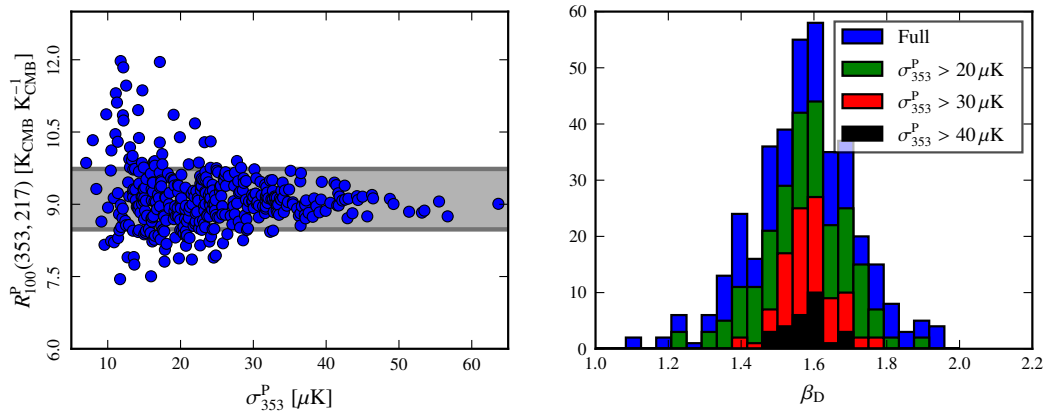

Figure A.1: We reproduce Figure 8 of Planck Collaboration (2015) on the left, and use the mean and standard deviation of β_{D} listed in the paper to reproduce the full histogram on the right, along with subsets corresponding to lower limits on signal fluctuation $\sigma^{\mathrm{P}}_{353}$. The data with lower limits 30 μK and 40 μK correspond to the same lower limits explored in §B of Planck Collaboration (2015), and yield β_{D} fluctuations consistent with the β_{D} dispersion measured in Monte Carlo simulations with a *constant* β_{D} and *Planck* noise.

where β_{D} is the spectral index of the dust, T_{D} is the dust temperature, and I_ν is the total signal intensity at frequency ν. To remove the CMB contribution from the dust-dominated bands, they subtracted I_{ν_0} from I_{ν_2} and I_{ν_1} before taking a ratio, and assumed the dust follows a modified blackbody spectrum $\propto \nu^{\beta_{\mathrm{D}}} B_\nu(T_{\mathrm{D}})$. They estimated the dust temperature using $R^{\mathrm{I}}(3000, 857)$ with DIRBE data as the high-frequency template, while they computed spectral indices using $R^{\{\mathrm{I,P}\}}_{100}(353, 217)$. Using T_{D}, they implicitly solved for β_{D} for each patch.

The resulting distribution of β_{D} from *Planck* has a 1σ dispersion of $\sigma_{\beta_{\mathrm{D}}} = 0.17$, which at face value suggests true on-sky spectral index variation. However, each sky patch has an associated local dispersion $\sigma^{\mathrm{P}}_{353}$ in the 353 GHz dust template brightness, with higher values corresponding to higher signal-to-noise, and Planck Collaboration (2015) claim that low signal-to-noise values with $\sigma^{\mathrm{P}}_{353} < 20\,\mu$K are dominated by instrument noise. Additionally, in Appendix B of Planck Collaboration (2015), Monte

Carlo simulations of dust polarization with *constant* $T_{\rm D}$ and $\beta_{\rm D}$ and instrument noise give a 1σ dispersion $\sigma_{\beta_{\rm D}} = 0.07$ in $\beta_{\rm D}$ (which is therefore entirely due to instrument noise) for sky patches with signal $\sigma^{\rm P}_{353} > 30\,\mu$K.

Using data from the top plot of Figure 8 of Planck Collaboration (2015) and the relation from Equation A.4 fixing $T_{\rm D}$ to be constant, we rescale $R^{\rm P}_{100}(353, 217)$, assuming a log-linear relation between $R^{\rm P}_{100}(353, 217)$ and $\beta_{\rm D}$. We rescale $\beta_{\rm D}$ to have the quoted mean and standard deviation of $\beta_{\rm D} = 1.59 \pm 0.17$. We reproduce Figure 8 of Planck Collaboration (2015) in our Figure A.1. Using these estimates, we compute the standard deviation of subsets of the data with $\sigma^{\rm P}_{353} > [20, 30, 40]\,\mu$K, obtaining $\sigma^{\rm P}_{\beta_{\rm D}} = [0.12, 0.07, 0.05]$, respectively. We observe that the observed variation of $\sigma^{\rm P}_{\beta_{\rm D}} = 0.07$ for $\sigma^{\rm P}_{353} > 30\,\mu$K is entirely consistent with effects of instrument noise seen in the Planck Collaboration (2015) Monte Carlo simulations and, therefore, with the hypothesis of a constant dust spectral index in the polarization data. Based on this, we claim that our model of dust spatial spectral variation with $\sigma^{\rm P}_{\beta_{\rm D}} = 0.01$ as shown in Figure 2.3 is consistent with the latest *Planck* data.

A.3 Derivation of pseudo-C_ℓ likelihood

In Hamimeche and Lewis (2008), the cut-sky approximation for a pseudo-C_ℓ likelihood is derived assuming a fixed power spectrum estimate. However, by the nature of the joint cosmological parameter and foreground cleaning estimates, this is not accurate for our purposes, and the best-fit solution ends up being one where the total noise level is increased without bound. Here we review the calculations of Hamimeche and Lewis while keeping the dependence of the estimated $\hat{C}_\ell$ explicit.

The spherical harmonic coefficient vector $\mathbf{a}_{\ell m} = (a^{\rm T}_{\ell m}, a^{\rm E}_{\ell m}, a^{\rm B}_{\ell m})^T$ is a normally

distributed random variable with covariance matrix at each ℓ

$$\boldsymbol{C}_\ell \equiv \langle \mathbf{a}_{\ell m} \mathbf{a}_{\ell m}^\dagger \rangle \tag{A.5}$$

and estimator

$$\hat{\boldsymbol{C}}_\ell \equiv \frac{1}{2\ell+1} \sum_m \mathbf{a}_{\ell m} \mathbf{a}_{\ell m}^\dagger. \tag{A.6}$$

In standard ΛCDM the $\mathbf{a}_{\ell m}$ are Gaussian distributed with

$$-2 \ln P(\{\mathbf{a}_{\ell m}\}|\boldsymbol{C}_\ell) = \sum_m [\mathbf{a}_{\ell m}^\dagger \boldsymbol{C}_\ell^{-1} \mathbf{a}_{\ell m} + \ln |2\pi \boldsymbol{C}_\ell|] = (2\ell+1)\big(\mathrm{Tr}[\hat{\boldsymbol{C}}_\ell \boldsymbol{C}_\ell^{-1}] + \ln |\boldsymbol{C}_\ell|\big) + \text{const.} \tag{A.7}$$

For a full-sky likelihood, $\hat{\boldsymbol{C}}_\ell$ contains all of the sky's information, and is drawn from a Wishart distribution,

$$P(\hat{\boldsymbol{C}}_\ell|\boldsymbol{C}_\ell) \propto \frac{|\hat{\boldsymbol{C}}_\ell|^{(2\ell-n)/2}}{|\boldsymbol{C}_\ell|^{(2\ell+1)/2}} e^{-(2\ell+1)\mathrm{Tr}(\hat{\boldsymbol{C}}_\ell \boldsymbol{C}_\ell^{-1})/2} \tag{A.8}$$

where n is the number of fields considered. We take $n = 2$ for $a_{\ell m}^{\mathrm{E}}$ and $a_{\ell m}^{\mathrm{B}}$.

The root of the Hamimeche and Lewis approximation involves rewriting this likelihood in a quadratic form. Using orthogonal $\boldsymbol{U}_\ell$ and diagonal $\boldsymbol{D}_\ell$ to rewrite $\boldsymbol{C}_\ell^{-1/2} \hat{\boldsymbol{C}}_\ell \boldsymbol{C}_\ell^{-1/2} \equiv \boldsymbol{U}_\ell \boldsymbol{D}_\ell \boldsymbol{U}_\ell^T$, the probability can be written as

$$-2 \ln P = (2\ell+1) \left\{ \mathrm{Tr}[\hat{\boldsymbol{C}}_\ell \boldsymbol{C}_\ell^{-1}] + \ln |\boldsymbol{C}_\ell| - \frac{2\ell - n}{2\ell+1} \ln |\hat{\boldsymbol{C}}_\ell| \right\} + \text{const.} \tag{A.9}$$

$$= (2\ell+1) \left\{ \mathrm{Tr}[\hat{\boldsymbol{C}}_\ell \boldsymbol{C}_\ell^{-1}] - \ln |\hat{\boldsymbol{C}}_\ell \boldsymbol{C}_\ell^{-1}| - n \right\} + n \Big[\ln |\hat{\boldsymbol{C}}_\ell| + 2\ell + 1 \Big] + \text{const.} \tag{A.10}$$

$$= \frac{2\ell+1}{2} \mathrm{Tr}[\boldsymbol{G}(\boldsymbol{D}_\ell)]^2 + n \ln |\hat{\boldsymbol{C}}_\ell| + \text{const.} \tag{A.11}$$

where $G(x) \equiv \sqrt{2(x - \ln x - 1)}$ and $[\boldsymbol{G}(\boldsymbol{D}_\ell)]_{ij} = G(D_{\ell,ii}) \delta_{ij}$.

Note that in Equation A.9, if we assume that $\hat{\boldsymbol{C}}_\ell$ is constant, we can adjust the constant such that $-2 \ln P = 0$ when $\boldsymbol{C}_\ell = \hat{\boldsymbol{C}}_\ell$. This is where our derivation differs from Hamimeche and Lewis. From here, the derivation in Hamimeche and Lewis applies, carrying along the extra $n \ln |\hat{\boldsymbol{C}}_\ell|$ term. This term essentially adds a penalty for increasing the noise, preventing the coefficients in $\hat{\boldsymbol{C}}_\ell = \sum_{\nu_1,\nu_2} c_{\nu_1} c_{\nu_2} \hat{\boldsymbol{C}}_\ell^{\nu_1 \times \nu_2}$ from getting too large.

Appendix B

Background Material

This appendix includes useful results that are unpublished but used n the course of my dissertation (section B.1 and section B.2).

B.1 Real spherical harmonics

Functions on the sphere are traditionally decomposed into complex spherical harmonics

$$X(\hat{\boldsymbol{n}}) = \sum_{\ell,m} x_\ell^m Y_\ell^m(\hat{\boldsymbol{n}}) \tag{B.1}$$

where the spherical harmonics used in the `HEALPix` convention are

$$Y_\ell^m(\theta, \phi) = \lambda_{\ell m}(\cos\theta) e^{im\phi} \tag{B.2}$$

where

$$\lambda_{\ell m}(x) = \begin{cases} \sqrt{\frac{2\ell+1}{4\pi}\frac{(\ell-m)!}{(\ell+m)!}} P_{\ell m}(x) & m \geq 0 \\ (-1)^m \lambda_{\ell|m|}(x) & m < 0 \\ 0 & |m| > \ell \end{cases} \tag{B.3}$$

and the associated Legendre polynomials are the solutions of the differential equation

$$(1-x^2)\frac{\mathrm{d}^2}{\mathrm{d}x^2}P_{\ell m} - 2x\frac{\mathrm{d}}{\mathrm{d}x}P_{\ell m} + \left(\ell(\ell+1) - \frac{m^2}{1-x^2}\right)P_{\ell m} = 0. \tag{B.4}$$

The fields we deal with (T, E, and B) are all real quantities, so there are constraints on the complex x_ℓ^m. It is therefore convenient to work with real spherical harmonics $Y_{\ell m}$ defined as

$$Y_{\ell m} = \begin{cases} \frac{i}{\sqrt{2}}(Y_\ell^m - (-1)^m Y_\ell^{-m}) & m < 0 \\ Y_\ell^0 & m = 0 \\ \frac{1}{\sqrt{2}}(Y_\ell^{-m} + (-1)^m Y_\ell^m) & m > 0 \end{cases} \tag{B.5}$$

so that the real-space spherical harmonic decomposition is given by

$$X(\hat{\boldsymbol{n}}) = \sum_{\ell m} x_{\ell m} Y_{\ell m} \tag{B.6}$$

$$= \sum_{\ell m} \begin{cases} x_{\ell m}\frac{i}{\sqrt{2}}(Y_\ell^m - (-1)^m Y_\ell^{-m}) & m < 0 \\ x_{\ell 0} Y_\ell^0 & m = 0 \\ x_{\ell m}\frac{1}{\sqrt{2}}(Y_\ell^{-m} + (-1)^m Y_\ell^m) & m > 0 \end{cases} \tag{B.7}$$

$$= \sum_{\ell m} Y_\ell^m \begin{cases} (x_{\ell m}\frac{i}{\sqrt{2}} + x_{\ell,-m}\frac{1}{\sqrt{2}}) & m < 0 \\ x_{\ell 0} & m = 0 \\ (x_{\ell m}\frac{1}{\sqrt{2}} - x_{\ell,-m}\frac{i}{\sqrt{2}})(-1)^m & m < 0 \end{cases} \tag{B.8}$$

$$= \sum_{\ell m} x_\ell^m Y_\ell^m. \tag{B.9}$$

Compare this to the function `complex2real` that takes an array of complex x_ℓ^m as inputs and outputs an array of real $x_{\ell m}$.

```
1  def complex2real(ellmax, mmax, cx_alm):
2      """
3      Convert an array from HealPy of complex-valued alms into an
       array
4      of real-valued alms.
5      """
6      len_ = ilength(ellmax, mmax)
7      assert(cx_alm.shape[0] == len_)
8      #print "len = ", len
9      re_alm = np.zeros((ellmax+1)**2, dtype='double')
10     for i in range(len_):
11         ell, m = i2lm(ellmax, i)
12         r = lm2r(ell, m)
13         if m == 0:
14             re_alm[r] = np.real(cx_alm[i])
15         else:
16             re_alm[r] = np.real(cx_alm[i]) * np.sqrt(2.0)
17             r = lm2r(ell, -m)
18             re_alm[r] = (-1)**m * np.imag(cx_alm[i]) * np.sqrt(2.0)
19
20     return re_alm
```

The functional form that is implemented here is found in lines 13–18,

$$a_{\ell,m} = \sqrt{2}\Re[a_\ell^m] \tag{B.10}$$

$$a_{\ell,-m} = (-1)^m\sqrt{2}\Im[a_\ell^m]. \tag{B.11}$$

For completeness, I also list the `real2complex` function brings the real $x_{\ell m}$ back into the complex form that `healpy` uses.

```
1  def real2complex(re_alm, ellmax=-1, mmax=-1):
2      """
3      Convert an array of real-valued alms to a healpy array of
       complex-valued
4      alms.
5      """
6      if ellmax < 0:
7          ellmax = np.floor(np.sqrt(re_alm.shape[0] - 1)).astype(int)
8      if mmax < 0:
9          mmax = ellmax
10     assert(re_alm.shape[0] >= (ellmax+1)**2)
11     len_ = int(ilength(ellmax, mmax))
12     cx_alm = np.zeros(len_, dtype='cfloat')
13     for i in range(len_):
14         ell, m = i2lm(ellmax, i)
15         r1 = lm2r(ell, m)
16         if m == 0:
17             cx_alm[i] = re_alm[r1]
18         else:
19             r2 = lm2r(ell, -m)
20             cx_alm[i] = (re_alm[r1] + (-1)**m * 1.0j * re_alm[r2])
       / np.sqrt(2.0)
21
22     return cx_alm
```

Lines 16–20 are the ones relevant to this discussion. Essentially, the function that is implemented here is

$$a_\ell^m = \frac{1}{\sqrt{2}}(a_{\ell,m} + (-1)^m i a_{\ell,-m}). \tag{B.12}$$

B.2 Construction of pixel-space covariance matrix

To compare theoretical power spectra to polarized data, it is necessary to construct a pixel-space covariance matrix C_{ij}. This is computed analytically in Appendix A of Tegmark and de Oliveira-Costa (2001), but analytic issues at the poles and relative

computational ease make us favor an numerical approach.

Basically, each $a_{\ell m}^{\mathrm{T/E/B}}$ corresponds to an IQU map. Functionally, we represent the spherical harmonic transform of a polarized map as a vector of length $3(\ell_{\mathrm{max}}+1)^2$

$$\boldsymbol{a} = (a_{00}^{\mathrm{T}}, a_{1,-1}^{\mathrm{T}}, \cdots a_{\ell_{\mathrm{max}},\ell_{\mathrm{max}}}^{\mathrm{T}}, a_{0,0}^{\mathrm{E}}, \ldots, a_{\ell_{\mathrm{max}},\ell_{\mathrm{max}}}^{\mathrm{B}}) \tag{B.13}$$

with a corresponding map $\boldsymbol{m} = \mathbf{Y}\boldsymbol{a}$ represented by a $3N_{\mathrm{pix}}$ vector and $\mathbf{Y}$ the real-space inverse spherical harmonic transform operator, and is represented by a $3N_{\mathrm{pix}} \times N_{a_{\ell m}}$ matrix. We can also construct an approximation to the spherical harmonic transform by taking the pseudo-inverse, denoted here as $\mathbf{Y^{-1}}$. Note that this is not a true inverse because in general $N_{\mathrm{pix}} > N_{a_{\ell m}}$, where for a full sky $N_{\mathrm{pix}} = 12N_{\mathrm{side}}^2$ and $N_{a_{\ell m}} = (\ell_{\mathrm{max}}+1)^2$. For a given resolution, the largest reliable multipole is $\ell_{\mathrm{max}} = 2N_{\mathrm{side}}$, and the largest multipole that can be recovered is $\ell_{\mathrm{max}} = 3N_{\mathrm{side}} - 1$, so that $N_{a_{\ell m}} \leqslant 9N_{\mathrm{side}}^2 < N_{\mathrm{pix}} \leqslant 12N_{\mathrm{side}}^2$.

The pixel space covariance matrix is related to the C_ℓ by

$$\boldsymbol{C} = \langle (\mathbf{Y}\boldsymbol{a})(\mathbf{Y}\boldsymbol{a})^T \rangle \tag{B.14}$$

$$= \mathbf{Y}\langle \boldsymbol{a}\boldsymbol{a}^T \rangle \mathbf{Y}^T \tag{B.15}$$

$$= \mathbf{Y}\boldsymbol{\mathscr{C}}\mathbf{Y}^T \tag{B.16}$$

where $\boldsymbol{\mathscr{C}}$ is the multipole-space covariance matrix

$$\mathscr{C}_{(\ell m)(\ell m)'} = \delta_{\ell\ell'}\delta_{mm'} \begin{pmatrix} C_\ell^{\mathrm{TT}} & C_\ell^{\mathrm{TE}} & C_\ell^{\mathrm{TB}} \\ C_\ell^{\mathrm{TE}} & C_\ell^{\mathrm{EE}} & C_\ell^{\mathrm{EB}} \\ C_\ell^{\mathrm{TB}} & C_\ell^{\mathrm{EB}} & C_\ell^{\mathrm{BB}} \end{pmatrix}. \tag{B.17}$$

For each set of multipoles C_ℓ, it is possible to construct a corresponding pixel-space

covariance matrix $\boldsymbol{C}_\ell = \mathbf{Y}\mathscr{C}\mathbf{Y}^T$. Functionally we achieve this by using basis in real $a_{\ell m}$ space and transform it to a map using the `hp.synfast` routine, thus creating the real-space spherical harmonic matrix $\mathbf{Y}$.

B.3 The Boltzmann Equation

The stress energy tensor is related to the distribution of photons by integrating over the phase space density and summing over all polarization states,

$$T_{\mu\nu} = \frac{1}{\sqrt{-g}} \int \mathrm{d}^3 p \, g_{ij} n^{ij}(\boldsymbol{x}, \boldsymbol{p}, t) \frac{p_\mu p_\nu}{p^0}. \tag{B.18}$$

The phase space density matrix n^{ij} can be thought of as the number of photons per unit volume in physical space per unit volume in momentum space with ellipticity vectors in both the i and j direction, and can be written

$$n^{ij} \equiv \sum_r \delta\big(\boldsymbol{x} - \boldsymbol{x}_r(t)\big)\delta\big(\boldsymbol{p} - \boldsymbol{p}_r(t)\big) \sum_\lambda P_r(\lambda) e^i\big(\boldsymbol{p}_r(t), \lambda\big) e^{j*}\big(\boldsymbol{p}_r(t), \lambda\big). \tag{B.19}$$

$P_r(\lambda)$ is the probability that photon r has polarization λ, and $\boldsymbol{e}(\boldsymbol{p}, \lambda)$ is a polarization vector for photons with three-momentum $\boldsymbol{p}$ and polarization λ, with $p_i e^i = 0$ and $g_{ij} e^i(\boldsymbol{p}, \lambda) e^{j*}(\boldsymbol{p}, \lambda') = \delta_{\lambda\lambda'}$. Note that $\boldsymbol{e}(\boldsymbol{p}, \lambda)$ is a complex vector that is always perpendicular to the corresponding photon's momentum and has unit norm ($p_i e^i = 0$ and $g_{ij} e^i(\lambda) e^{j*}(\lambda') = \delta_{\lambda\lambda'}$, respectively).

The collisional Boltzmann equation is

$$\frac{\mathrm{d}n^{ij}}{\mathrm{d}t} = C[n^{ij}]$$

where C encodes the physics of scattering, and $\frac{\mathrm{d}}{\mathrm{d}t}$ is the total time differential. Using $\frac{\mathrm{d}x^i}{\mathrm{d}t} = \frac{p^i}{p^0}$ (the definition of velocity in general relativity), $\frac{\partial p_i}{\partial t} = \frac{p^k p^l}{2p^0} \frac{\partial g_{kl}}{\partial x^i}$ (the geodesic

equation), and

$$\frac{\partial e^i}{\partial t} = -e^m \frac{p^k p^l p^i}{2(p^0)^3} \frac{\partial g_{kl}}{\partial x^m} - \frac{1}{2}\left(\dot{g}_{kl} + \frac{p^m}{p^0}\frac{\partial g_{kl}}{\partial x^m}\right) e^k \left(g^{li} - \frac{p^l p^i}{(p^0)^2}\right) \tag{B.20}$$

(the equation of parallel transport for ellipticity 4-vectors), it is possible to write down the full differential equation.

The evolution of the phase space polarization matrix is given by

$$\frac{\partial n^{ij}}{\partial t} + \frac{\partial n^{ij}}{\partial x^k}\frac{p^k}{p^0} + \frac{p^k p^l}{2p^0}\frac{\partial g_{kl}}{\partial x^m}\left(\frac{\partial n^{ij}}{\partial p_m} - \frac{p^i}{(p^0)^2}n^{mj} - \frac{p^j}{(p^0)^2}n^{im}\right) \tag{B.21}$$

$$-\frac{1}{2}\left(\dot{g}_{kl} + \frac{p^m}{p^0}\frac{\partial g_{kl}}{\partial x^m}\right)\left[n^{kj}\left(g^{li} - \frac{p^l p^i}{(p^0)^2}\right) + n^{ik}\left(g^{lj} - \frac{p^l p^j}{(p^0)^2}\right)\right] = C^{ij} \tag{B.22}$$

The zeroth order solution is given by $\frac{1}{2}\bar{n}_\gamma(a(t)p^0)\left(g^{ij} - \frac{p^i p^j}{(p^0)^2}\right)$, as can be verified by taking the trace to obtain $\bar{n}_\gamma(ap^0)$. When the zeroth order solution is subtracted out, the time variation of the perturbations δn^{ij} is given by

$$\boxed{\frac{\partial \delta n^{ij}}{\partial t} + \frac{\hat{p}_m}{a}\frac{\partial \delta n^{ij}}{\partial x^m} + 2\frac{\dot{a}}{a}\delta n^{ij} - \frac{1}{4a^2}p\bar{n}'_\gamma \hat{p}_k \hat{p}_l \frac{\partial}{\partial t}\left(\frac{\delta g_{kl}}{a^2}\right)(\delta^{ij} - \hat{p}_i\hat{p}_j) = \delta C^{ij}} \tag{B.23}$$

where $p \equiv \sqrt{p_i p_i}$, $\hat{\boldsymbol{p}} \equiv \boldsymbol{p}/p$, and

$$\delta C^{ij} = -\omega_c \delta n^{ij} - \frac{\omega_c}{2a^3}(p_k \delta u_k)\bar{n}'_\gamma(\delta^{ij} - \hat{p}_i\hat{p}_j) \tag{B.24}$$

$$+ \frac{3\omega_c}{8\pi}\int \mathrm{d}^2\hat{p}_1[\delta n^{ij} - \hat{p}_i\hat{p}_k\delta n^{ij} - \hat{p}_j\hat{p}_k\delta n^{ik} + \hat{p}_i\hat{p}_j\hat{p}_k\hat{p}_l\delta n^{kl}]. \tag{B.25}$$

Here, $\omega_c = n_e(t)\sigma_\mathrm{T}$ is the collision rate of photons with the plasma, and $n_e(t)$ is the number density of free electrons. We also note that the number density fluctuation equivalent of Equation 1.22 for specific intensity is given by

$$a^4\bar{\rho}_\gamma J_{ij}(\boldsymbol{x}, \hat{\boldsymbol{p}}, t) = a^2\int_0^\infty 4\pi p^3\,\mathrm{d}p\,\delta n^{ij}(\boldsymbol{x}, |\boldsymbol{p}|\hat{\boldsymbol{p}}, t). \tag{B.26}$$

Scalar modes

In the synchronous gauge, we can consider the scalar perturbations A and B in Fourier space, so that the Boltzmann equation for J_{ij} becomes

$$\frac{\partial J_{ij}}{\partial t} + i\frac{\hat{\boldsymbol{p}}\cdot\boldsymbol{k}}{a}J_{ij} + \alpha(\boldsymbol{k})\left[\dot{A}_k - (\boldsymbol{k}\cdot\hat{\boldsymbol{p}})^2\dot{B}_k\right](\delta_{ij} - \hat{p}_i\hat{p}_j) = -\omega_c J_{ij} \tag{B.27}$$

$$+ \frac{3\omega_c}{8\pi}\int \mathrm{d}^2\hat{p}_1\left[J_{ij} - \hat{p}_i\hat{p}_k J_{kj} - \hat{p}_j\hat{p}_k J_{ik} + \hat{p}_i\hat{p}_j\hat{p}_k\hat{p}_l J_{kl}\right] + \frac{2\omega_c}{a}(\hat{p}_k\delta u_k)(\delta^{ij} - \hat{p}_i\hat{p}_j) \tag{B.28}$$

We may decompose the intensity matrix into a polarized and unpolarized component, i.e.

$$J_{ij} = \alpha(\boldsymbol{k})\left\{\frac{1}{2}\left(\Delta_T^{(S)} - \Delta_P^{(S)}\right)(\delta_{ij} - \hat{p}_i\hat{p}_j) + \Delta_P^{(S)}\left[\frac{(\hat{k}_i - (\hat{\boldsymbol{k}}\cdot\hat{\boldsymbol{p}})\hat{p}_i)(\hat{k}_j - (\hat{\boldsymbol{k}}\cdot\hat{\boldsymbol{p}})\hat{p}_j)}{1 - (\hat{\boldsymbol{p}}\cdot\hat{\boldsymbol{k}})^2}\right]\right\} \tag{B.29}$$

We can also define source functions

$$\int \frac{\mathrm{d}^2\hat{\boldsymbol{p}}}{4\pi}J_{ij} = \alpha(\boldsymbol{k})\left[\delta_{ij}\Phi + \frac{1}{2}\hat{k}_i\hat{k}_j\Pi\right]$$

and $\mu \equiv \hat{\boldsymbol{k}}\cdot\hat{\boldsymbol{p}}$, which yield the coupled Boltzmann equations for scalar fluctuations;

$$\dot{\Delta}_P^{(S)} + i\frac{k\mu}{a}\Delta_P^{(S)} = -\omega_c\left[\Delta_P^{(S)} - \frac{3}{4}(1-\mu^2)\Pi\right] \tag{B.30}$$

$$\dot{\Delta}_T^{(S)} + i\frac{k\mu}{a}\Delta_T^{(S)} = -\omega_c\left[\Delta_T^{(S)} - \frac{3}{4}(1-\mu^2)\Pi - 3\Phi - \frac{4ik\mu}{a}\delta u_{Bk}\right] - 2\dot{A}_k + 2k^2\mu^2\dot{B}_k \tag{B.31}$$

It is convenient to express these in terms of a Legendre polynomial expansion,

$$\Delta_{T/P}^{(S)}(k,\mu,t) = \sum_{\ell=0}^{\infty}(-i)^\ell(2\ell+1)P_\ell(\mu)\Delta_{T/P,\ell}^{(S)}(k,t) \tag{B.32}$$

which gives us a framework to write the source functions as $\Phi = \frac{1}{6}[2\Delta_{T,0}^{(S)} - \Delta_{T,2}^{(S)} -$

$\Delta_{P,0}^{(S)} - \Delta_{P,2}^{(S)}]$ and $\Pi = \Delta_{P,0}^{(S)} + \Delta_{T,2}^{(S)} + \Delta_{P,2}^{(S)}$.

Tensor modes

The only place that tensor fluctuations appear in perturbations is in the off-diagonal terms $h_{ij} = a^2 D_{ij}$. We can use this to write the equivalent of Equation B.27

$$\frac{\partial J_{ij}}{\partial t} + i\frac{\hat{p}\cdot\boldsymbol{k}}{a}J_{ij} + \hat{p}_k\hat{p}_l e_{kl}\dot{\mathcal{D}}_k(\delta_{ij} - \hat{p}_i\hat{p}_j) = -\omega_c J_{ij} \tag{B.33}$$

$$+ \frac{3\omega_c}{8\pi}\int \mathrm{d}^2\hat{p}_1[J_{ij} - \hat{p}_i\hat{p}_k J_{kj} - \hat{p}_j\hat{p}_k J_{ik} + \hat{p}_i\hat{p}_j\hat{p}_k\hat{p}_l J_{kl}]. \tag{B.34}$$

Equation B.33 differs from Equation B.27 only in the final term on the left-hand side (the metric fluctuations) and the lack of a velocity term, which has no tensor fluctuations.

The source term is defined as

$$\int \frac{\mathrm{d}^2\hat{\boldsymbol{p}}_1}{4\pi} J_{ij}(\boldsymbol{k}, \hat{\boldsymbol{p}}_1, t, \lambda) = -\frac{2}{3}e_{ij}(\hat{\boldsymbol{k}}, \lambda)\Psi(k, t) \tag{B.35}$$

and the intensity matrix is decomposed as

$$J_{ij} = \frac{1}{2}(\delta_{ij} - \hat{p}_i\hat{p}_j)\hat{p}_k\hat{p}_l e_{kl}\left(\Delta_T^{(T)} + \Delta_P^{(T)}\right) + \left(e_{ij} - \hat{p}_i\hat{p}_k e_{kj} - \hat{p}_j\hat{p}_k e_{ik} + \hat{p}_i\hat{p}_j\hat{p}_k\hat{p}_l e_{kl}\right)\Delta_P^{(T)} \tag{B.36}$$

With this in hand, we can write down the coupled Boltzmann equations for temperature and polarization fluctuations due to tensor modes,

$$\dot{\Delta}_T^{(T)} + i\frac{k\mu}{a}\Delta_T^{(T)} = -\omega_c[\Delta_T^{(T)} - \Psi] - 2\dot{\mathcal{D}}_k \tag{B.37}$$

$$\dot{\Delta}_P^{(T)} + i\frac{k\mu}{a}\Delta_P^{(T)} = -\omega_c[\Delta_P^{(T)} + \Psi] \tag{B.38}$$

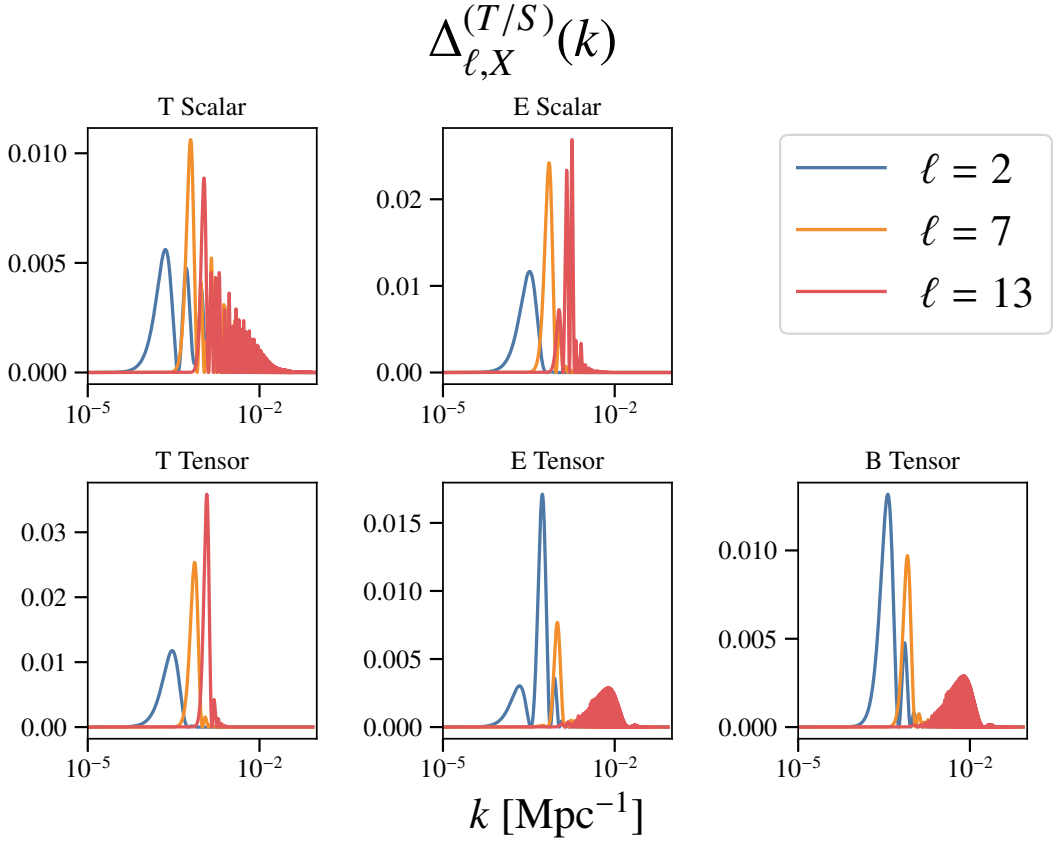

Figure B.1: We display a sample of the relevant transfer functions $\Delta_{\ell,X}^{(T/S)}(k)$ to demonstrate how the 3D Fourier modes propagate to multipole space.

which can be analogously decomposed into

$$\Delta_{T/P}^{(T)}(k,\mu,t) = \sum_{\ell=0}^{\infty}(-i)^{\ell}(2\ell+1)P_{\ell}(\mu)\Delta_{T/P,\ell}^{(T)}(k,t). \tag{B.39}$$

The source term can be rewritten as

$$\Psi = \frac{1}{10}\Delta_{T,0}^{(T)} + \frac{1}{7}\Delta_{T,2}^{(T)} + \frac{3}{70}\Delta_{T,4}^{(T)} - \frac{3}{5}\Delta_{P,0}^{(T)} + \frac{6}{7}\Delta_{P,2}^{(T)} - \frac{3}{70}\Delta_{P,4}^{(T)} \tag{B.40}$$

References

Watts, D. J., D. Larson, T. A. Marriage, M. H. Abitbol, J. W. Appel, C. L. Bennett, D. T. Chuss, J. R. Eimer, T. Essinger-Hileman, N. J. Miller, K. Rostem, and E. J. Wollack (2015). "Measuring the Largest Angular Scale CMB B-mode Polarization with Galactic Foregrounds on a Cut Sky". In: ApJ 814, 103, p. 103. DOI: 10.1088/0004-637X/814/2/103. arXiv: 1508.00017.

Watts, D. J., B. Wang, A. Ali, J. W. Appel, C. L. Bennett, D. T. Chuss, S. Dahal, J. R. Eimer, T. Essinger-Hileman, K. Harrington, G. Hinshaw, J. Iuliano, T. A. Marriage, N. J. Miller, I. L. Padilla, M. Petroff, K. Rostem, E. J. Wollack, and Z. Xu (2018). "A Projected Estimate of the Reionization Optical Depth Using the CLASS Experiment's Sample-Variance Limited E-Mode Measurement". In: *ArXiv e-prints*. arXiv: 1801.01481.

Knox, L. (1995). "Determination of inflationary observables by cosmic microwave background anisotropy experiments". In: Phys. Rev. D 52, pp. 4307–4318. DOI: 10.1103/PhysRevD.52.4307. eprint: astro-ph/9504054.

Planck Collaboration (2015). "Planck intermediate results. XXII. Frequency dependence of thermal emission from Galactic dust in intensity and polarization". In: A&A 576, A107, A107. DOI: 10.1051/0004-6361/201424088. arXiv: 1405.0874.

Hamimeche, S. and A. Lewis (2008). "Likelihood analysis of CMB temperature and polarization power spectra". In: Phys. Rev. D 77.10, 103013, p. 103013. DOI: 10.1103/PhysRevD.77.103013. arXiv: 0801.0554.

Tegmark, M. and A. de Oliveira-Costa (2001). "How to measure CMB polarization power spectra without losing information". In: Phys. Rev. D 64.6, 063001, p. 063001. DOI: 10.1103/PhysRevD.64.063001. eprint: astro-ph/0012120.

Duncan Joseph Watts

Department of Physics and Astronomy
Johns Hopkins University
Email: dwatts@jhu.edu
Phone: +1 609 280 0994
orcid: 0000-0002-5437-6121

233 Bloomberg Center
Johns Hopkins University
3400 N. Charles Street
Baltimore, MD, 21218, USA

Research Interests:

Cosmology
Cosmic Microwave Background Physics
Inflation
Galactic Foregrounds
Nonlinear optimization
Monte Carlo Markov Chain methods
Distributed computing (`slurm`, `PBS`)
Multivariate statistics

Education:

Johns Hopkins University
2012–2018, Ph.D. Physics and Astronomy
Advisor: Tobias A. Marriage
Thesis: Methods and Projections for Joint Foreground and Cosmological Parameter Estimation for the CLASS Experiment
2012–2014, M.A. Physics and Astronomy

Harvard University
2008–2012, A.B. Departmental Honors, Physics and Astronomy
Advisor: Douglas P. Finkbeiner
Thesis: An Investigation of Gamma-Rays in the Galactic Center

Teaching and Outreach

Fall 2012, Teaching Assistant, Introductory Physics Recitation and Laboratory
Fall 2016, Teaching Assistant/Lecturer, Graduate Cosmology
2012–2018, Volunteer, JHU Physics and Astronomy Graduate Student Public Outreach Group
2013–2016, Maryland Space Grant Observatory Fellowship

Collaborations:

2013–, The Cosmology Large Angular Scale Surveyor (CLASS) Collaboration

Conference Presentations and Talks

1. CMB-S4 Workshop, *Projected Constraints on Optical Depth to Reionization and Neutrino Mass from the CLASS Experiment*, August 2017
2. Great Lakes Cosmology Workshop, *Measuring CMB B-mode Polarization with Galactic Foregrounds on a Cut Sky*, June 2016
3. AAS Winter Meeting *Galactic foreground cleaning in support of a primordial CMB B-mode measurement*, January 2014

Workshops and Meetings

1. CMB-S4 Workshop, August 2017
2. SciCoder: Astroinformatics for Astronomers, July 2014

SELECTED PUBLICATIONS:

1. **Watts, D. J.**, B. Wang, and T. A. Marriage. A Projected Estimate of the Optical Depth to Reionization Using the CLASS Experiment's Sample-Variance limited E-Mode Measurement. *In preparation*, 2017
2. **Watts, D. J.**, D. Larson, T. A. Marriage, M. H. Abitbol, J. W. Appel, C. L. Bennett, D. T. Chuss, J. R. Eimer, T. Essinger-Hileman, N. J. Miller, K. Rostem, and E. J. Wollack. Measuring the Largest Angular Scale CMB B-mode Polarization with Galactic Foregrounds on a Cut Sky. ApJ, 814:103, December 2015
3. E. R. Switzer and **Watts, D. J.** Robust likelihoods for inflationary gravitational waves from maps of cosmic microwave background polarization. Phys. Rev. D, 94(6):063526, September 2016
4. J. L. Weiland, K. Osumi, G. E. Addison, C. L. Bennett, **Watts, D. J.**, M. Halpern, and G. Hinshaw. Effect of Template Uncertainties on the WMAP and Planck Measures of the Optical Depth Due To Reionization. *ArXiv e-prints*, January 2018
5. G. E. Addison, **Watts, D. J.**, C. L. Bennett, M. Halpern, G. Hinshaw, and J. L. Weiland. Elucidating ΛCDM: Impact of Baryon Acoustic Oscillation Measurements on the Hubble Constant Discrepancy. ApJ, 853:119, February 2018
6. G. E. Addison, Y. Huang, **Watts, D. J.**, C. L. Bennett, M. Halpern, G. Hinshaw, and J. L. Weiland. Quantifying Discordance in the 2015 Planck CMB Spectrum. ApJ, 818:132, February 2016

ALL PUBLICATIONS:

6. D. T. Chuss, A. Ali, M. Amiri, J. Appel, C. L. Bennett, F. Colazo, K. L. Denis, R. Dünner, T. Essinger-Hileman, J. Eimer, P. Fluxa, D. Gothe, M. Halpern, K. Harrington, G. Hilton, G. Hinshaw, J. Hubmayr, J. Iuliano, T. A. Marriage, N. Miller, S. H. Moseley, G. Mumby, M. Petroff, C. Reintsema, K. Rostem, K. U-Yen, **Watts, D.**, E. Wagner, E. J. Wollack, Z. Xu, and L. Zeng. Cosmology Large Angular Scale Surveyor (CLASS) Focal Plane Development. *Journal of Low Temperature Physics*, 184:759–764, August 2016
7. K. Harrington, T. Marriage, A. Ali, J. W. Appel, C. L. Bennett, F. Boone, M. Brewer, M. Chan, D. T. Chuss, F. Colazo, S. Dahal, K. Denis, R. Dünner, J. Eimer, T. Essinger-Hileman, P. Fluxa, M. Halpern, G. Hilton, G. F. Hinshaw, J. Hubmayr, J. Iuliano, J. Karakla, J. McMahon, N. T. Miller, S. H. Moseley, G. Palma, L. Parker, M. Petroff, B. Pradenas, K. Rostem, M. Sagliocca, D. Valle, **Watts, D.**, E. Wollack, Z. Xu, and L. Zeng. The Cosmology Large Angular Scale Surveyor. In *Millimeter, Submillimeter, and Far-Infrared Detectors and Instrumentation for Astronomy VIII*, volume 9914 of Proc. SPIE, page 99141K, July 2016
8. N. J. Miller, D. T. Chuss, T. A. Marriage, E. J. Wollack, J. W. Appel, C. L. Bennett, J. Eimer, T. Essinger-Hileman, D. J. Fixsen, K. Harrington, S. H. Moseley, K. Rostem, E. R. Switzer, and **Watts, D. J.** Recovery of Large Angular Scale CMB Polarization for Instruments Employing Variable-delay Polarization Modulators. ApJ, 818:151, February 2016
9. J. W. Appel, A. Ali, M. Amiri, D. Araujo, C. L. Bennet, F. Boone, M. Chan, H.-M. Cho, D. T. Chuss, F. Colazo, E. Crowe, K. Denis, R. Dünner, J. Eimer, T. Essinger-Hileman, D. Gothe, M. Halpern, K. Harrington, G. Hilton, G. F. Hinshaw, C. Huang, K. Irwin, G. Jones, J. Karakula, A. J. Kogut, D. Larson, M. Limon, L. Lowry, T. Marriage, N. Mehrle, A. D. Miller, N. Miller, S. H. Moseley, G. Novak, C. Reintsema, K. Rostem, T. Stevenson, D. Towner, K. U-Yen, E. Wagner, **Watts, D.**, E. Wollack, Z. Xu, and L. Zeng. The cosmology large angular scale surveyor (CLASS): 38-GHz detector array of bolometric polarimeters. In *Millimeter, Submillimeter, and Far-Infrared Detectors and Instrumentation for Astronomy VII*, volume 9153 of Proc. SPIE, page 91531J, July 2014
10. T. Essinger-Hileman, A. Ali, M. Amiri, J. W. Appel, D. Araujo, C. L. Bennett, F. Boone, M. Chan, H.-M. Cho, D. T. Chuss, F. Colazo, E. Crowe, K. Denis, R. Dünner, J. Eimer, D. Gothe, M. Halpern, K. Harrington, G. C. Hilton, G. F. Hinshaw, C. Huang, K. Irwin, G. Jones, J. Karakla, A. J. Kogut, D. Larson, M. Limon, L. Lowry, T. Marriage, N. Mehrle, A. D. Miller, N. Miller, S. H. Moseley, G. Novak, C. Reintsema, K. Rostem, T. Stevenson, D. Towner, K. U-Yen, E. Wagner, **Watts, D.**, E. J. Wollack, Z. Xu, and L. Zeng. CLASS: the cosmology large angular scale surveyor. In *Millimeter, Submillimeter, and Far-Infrared Detectors and Instrumentation for Astronomy VII*, volume 9153 of Proc. SPIE, page 91531I, July 2014